FACULDADE DE ENGENHARIA DA UNIVERSIDADE DO PORTO

Experimental characterisation and development of a numerical model to determine the failure mechanism of pressure-sensitive adhesives

Hugo Carneiro de Sousa



Master's in Mechanical Engineering

Supervisor:
Prof. Dr. Eduardo A. S. Marques

Co-Supervisors:
Dr. Ricardo J. C. Carbas
Prof. Dr. Lucas F. M. da Silva
Beatriz D. Simões

July 16, 2024

Experimental characterisation and development of a numerical model to determine the failure mechanism of pressure-sensitive adhesives

Hugo Carneiro de Sousa

Master's in Mechanical Engineering

July 16, 2024

Abstract

Adhesive joints have become increasingly popular in the last decades in the automotive and aeronautical industries because of their numerous advantages. Cost savings, overall structure weight reduction, and subsequently lower energy consumption are some of their primary benefits. Adhesive joints provide a more even distribution of stress and the removal of extra components, such as screws or welding beads, simplifies the automation of the manufacturing process. They are also great at damping vibrations and can function as good seals.

In recent years, pressure-sensitive adhesives (PSAs) have received greater interest, particularly in electronics. Their attractive characteristics, like their ease of design, simplicity in joint production at room temperature, and sustainability, have encouraged researchers to investigate their mechanical properties. Nevertheless, the most important and exclusive characteristic of PSAs is the fact that they not require an activation, which makes them unique and more efficient.

This thesis addresses the characterisation and numerical modelling of the failure modes of acrylic PSAs. Initially, double-cantilever beam (DCB) specimens were tested under mode I loading to obtain a cohesive law. This law was further developed and refined through the creation of a Python code, which facilitated the treatment of experimental data and its integration into a numerical model. Further experiments were conducted under mode III loading to expand the cohesive law's applicability to shear stress scenarios. An apparatus was developed for peel testing, aiming to create a complete failure envelope that correlates peel load with peel angle. This involved meticulous experimental testing to extract the adhesion energy and characterise the peel-front process zone using digital image processing techniques. The experimental data obtained was then used in a numerical model. Validating this model involves comparing its predictions with experimental results using identical specimen geometries and then using different geometric configurations.

To complement the experimental findings, bulk tensile testing data from previous studies were utilised to develop a numerical hyperelastic model.

Keywords: pressure-sensitive adhesives, fracture mechanics, adhesive joints

Resumo

O uso de juntas adesivas tornou-se cada vez mais popular nas últimas décadas em industrias como a automóvel e aeronáutica, devido às suas inúmeras vantagens. A poupança de custos, a redução do peso global das estruturas e, consequentemente, o menor consumo de energia são alguns dos seus principais benefícios. As juntas adesivas proporcionam uma distribuição mais uniforme da tensão e a remoção de componentes extra, como parafusos ou cordões de soldadura, o que simplifica a automação do processo de fabrico. Adicionalmente, apresentam boa capacidade de amortecer as vibrações e podem funcionar como vedantes. A utilização de adesivos sensíveis à pressão (PSA) tem também sido alvo de interesse crescente nos últimos anos, particularmente no domínio da eletrónica. Caraterísticas atrativas, como a facilidade de conceção, a simplicidade na produção de juntas à temperatura ambiente e a sustentabilidade, têm incentivado investigadores a estudar as suas propriedades mecânicas. Todavia, a caraterística mais importante e exclusiva dos PSA é o facto de não requererem um processo de ativação, o que os torna únicos e mais eficientes.

Esta tese aborda a caraterização e a modelação numérica dos modos de falha de PSAs acrílicos. Inicialmente, foram ensaiados provetes do tipo double cantilever beam (DCB) em modo I de modo a obter uma lei coesiva. Esta lei foi desenvolvida e aperfeiçoada através da criação de um código Python, que facilitou o tratamento dos dados experimentais e a sua posterior integração num modelo numérico. Foram realizados outros ensaios mecânicos em modo III para expandir a aplicabilidade da lei coesiva a cenários dominados por tensões de corte.

Foi desenvolvido um dispositivo de ensaio para condições de arrancamento, com o objetivo de criar um envelope de força em função do ângulo de arrancamento. Este processo envolveu testes experimentais meticulosos, que permitiram extrair a energia de adesão e caraterizar a zona de processo da frente de arrancamento utilizando técnicas digitais de processamento de imagem. Os dados experimentais obtidos foram posteriormente utilizados num modelo numérico. A validação deste modelo foi feita atráves da comparação das suas previsões com os resultados experimentais, utilizando geometrias de provete idênticas ás modeladas e, em seguida, utilizando diferentes configurações geométricas.

Para complementar os resultados experimentais, foram utilizados dados de ensaios de tração em espécimes de bulk de estudos anteriores para desenvolver um modelo numérico hiperelástico.

Keywords: adesivos sensíveis à pressão, mecânica da fratura, juntas adesivas

Acknowledgements

First, I extend my deepest gratitude to Professor Lucas da Silva for granting me the opportunity to participate in this significant project. His expertise, encouragement, and mentorship have been pivotal during this project.

I would also like to express my gratitude to my supervisors, Eduardo Marques and Ricardo Carbas, for their support, knowledge, consistent availability, and patience during this project.

I also wish to thank all Advanced Joining Processes Unit members for their ongoing support, insightful contributions, and the fellowship we cultivated during this project. Working alongside you has been a remarkable experience. A special thanks to my colleague Beatriz Simões, whose deep knowledge, and steadfast support have been crucial to the success of this project. Her dedication and support have greatly influenced my work, and I am sincerely grateful for her patience and assistance during this work.

My appreciation extends to all my friends who have been part of this five-year journey. I am grateful for all the moments and memories created.

Last but not least, I would like to thank all my family for their incredible support throughout my life. To my parents, Mário and Sofia, my sister Maria, my grandparents, Odete and Neves, and my girlfriend, Beatriz, your sacrifices and support have not gone unnoticed, and I am incredibly fortunate to have you all in my life.

"The best way to predict the future is to invent it."

Alan Kay

Contents

1 Introduction **1**
- 1.1 Background and motivation . . . 1
- 1.2 Objectives . . . 1
- 1.3 Methodology . . . 2
- 1.4 Layout of the dissertation . . . 3

2 Literature Review **5**
- 2.1 Survey of adhesives . . . 5
  - 2.1.1 Classification of adhesives . . . 6
  - 2.1.2 Failure modes and joint design . . . 7
- 2.2 Failure prediction approaches . . . 9
  - 2.2.1 Continuum mechanics . . . 9
  - 2.2.2 Fracture mechanics . . . 10
  - 2.2.3 Damage mechanics . . . 13
- 2.3 Pressure-sensitive adhesives (PSAs) . . . 14
  - 2.3.1 Characterisation of PSAs . . . 15
  - 2.3.2 Adhesion mechanisms of PSAs . . . 15
  - 2.3.3 Effect of joint design and testing parameters in performance of PSAs . . . 16
  - 2.3.4 Cohesive law estimation through DCB testing . . . 19
  - 2.3.5 Peel testing in PSAs . . . 19
  - 2.3.6 Numerical modelling of hyperelasticity in PSAs . . . 21

3 Experimental procedures **25**
- 3.1 Materials . . . 25
- 3.2 Specimen manufacturing . . . 26
  - 3.2.1 DCB specimens . . . 26
  - 3.2.2 Peel specimens . . . 30
- 3.3 Testing setup . . . 30
  - 3.3.1 DCB mode I testing . . . 31
  - 3.3.2 DCB mode III testing . . . 32
  - 3.3.3 Peel testing . . . 34
- 3.4 Experimental results . . . 35
  - 3.4.1 DCB mode I testing . . . 35
  - 3.4.2 DCB mode III testing . . . 38
  - 3.4.3 Peel testing . . . 41

4 Numerical details **43**
4.1 Cohesive zone modeling 43
4.1.1 DCB mode I testing 43
4.1.2 DCB mode III testing 44
4.1.3 Peel tests 48
4.2 Hyperelasticity 49

5 Cyclic creep stations **53**

6 Conclusions and Future Work **55**

References **57**

A Paper 1 - Development of a cohesive zone model to characterise the fracture behaviour of PSAs **63**

B Paper 2 - Experimental and numerical characterisation of the interface fracture behaviour of PSAs with peel tests **91**

C Python code for adhesion energy estimation **117**

D Python code for digital image processing **123**

List of Figures

2.1 Stress fields obtained with three different joining methods. Welding (left), riveting (centre) and adhesive bonding (right) [1]. . . . 6
2.2 Schematic representation of cohesive and adhesive failures [8]. . . . 8
2.3 Main types of loadings acting in adhesive joints [8]. . . . 9
2.4 Examples of joint configurations [8]. . . . 9
2.5 Singularities in the proximity of an adhesive edge. Adapted from [18]. . . . 10
2.6 Fracture modes for an adhesive joint [18]. . . . 11
2.7 Schematic representation of different cohesive law shapes: triangular or exponential (left) and trapezoidal (right). Adapted from [16]. . . . 13
2.8 Operating principle of a CZM. Adapted from [1]. . . . 14
2.9 (a) Tensile load-displacement responses, and (b) Strength and modulus properties at different loading rates. Adapted from [44]. . . . 18

3.1 DCB specimen geometry, in mm. . . . 26
3.2 DCB specimen configuration for mode I test, in mm. . . . 26
3.3 Representation of the mould used. . . . 27
3.4 Vacuum setup. . . . 28
3.5 Open vacuum mould. . . . 29
3.6 Adhesive A DCBs produced with (bottom) and without (top) a vacuum environment. 29
3.7 Peel specimen configuration, in mm. . . . 30
3.8 Manufacturing of the inclinometers supports. (a) Slicing of the inclinometers supports using PrusaSlicer software. (b) Assembly of the inclinometers supports to the DCB. . . . 31
3.9 DCB mode I testing setup. . . . 32
3.10 3D-printed supports for the inclinometers and DIC: (a) CAD model; (b) Slicing of the supports in the PrusaSlicer software. . . . 33
3.11 DCB specimen with the 3D-printed pieces under mode III loading conditions. . . . 33
3.12 Test setup attached to the testing machine (left). CAD model of the test setup (right). 34
3.13 Slicing of the different angle tables for the peel tests in the PrusaSlicer software. . 35
3.14 Load-displacement curves for DCB mode I testing with adhesives: (a) A and (b) B. 36
3.15 Rotations of the acrylics for DCB mode I testing with adhesives: (a) A using a vacuum condition manufacturing and (b) B. . . . 36
3.16 Fracture energy curves based on the J-integral approach for DCB mode I testing with adhesives: (a) A and (b) B. . . . 36
3.17 GOM correlate software: (a) procedure to ensure perpendicularity and (b) measuring of the CTOD for DCB mode I testing. . . . 37
3.18 CTOD measured using DIC for DCB mode I testing with adhesives: (a) A and (b) B. . . . 37

3.19 Average cohesive law for DCB mode I testing with adhesives: (a) A and (b) B. . 38
3.20 The tape with thickness h exhibits two modes of deformation: peel (w) and shear (v). Conjugated stress components σ and τ. Adapted from [79]. 38
3.21 Three different timestamps for DCB being loaded in mode III with Adhesive A. . 39
3.22 Three different timestamps for DCB being loaded in mode III with Adhesive B. . 39
3.23 Load-displacement curves for DCB mode III testing with adhesives: (a) A and (b) B. 40
3.24 Fracture energy curves based on the J-integral approach for DCB mode III testing with adhesives: (a) A and (b) B. 40
3.25 GOM correlate software: (a) procedure to ensure perpendicularity and (b) measuring of the CTSD for DCB mode III testing. 40
3.26 Average cohesive law for DCB mode III testing with adhesives: (a) A and (b) B. . 41
3.27 Peel curves for adhesive A. 41
3.28 Peel curves for adhesive B. 42

4.1 Average damage curves. 44
4.2 Mesh and boundary conditions used in the DCB mode I testing FE model. 44
4.3 Mesh used in the FE model. 45
4.4 Boundary conditions applied in the FE model. 45
4.5 Stresses contribution of different loading modes on a cohesive element for adhesives (a) A and (b) B. 46
4.6 Comparison between experimental and numerical load-displacement curves for DCB mode III testing with adhesives: (a) A and (b) B. 47
4.7 Schematic of the FE model. 48
4.8 Mesh and boundary conditions applied in the FE model of SLJ. 49
4.9 Experimental and numerical results for SLJ using bulk test data. Comparison between the different models. 50
4.10 Experimental and numerical results for SLJ using SLJ test data. Comparison between the different models. 50
4.11 Boundary conditions applied to the block in shear. 51
4.12 Experimental and numerical results for the stress tensor components in function of the shear stress. 51

5.1 Cyclic creep station evolution. 54
5.2 Thermal chambers. 54

List of Tables

3.1 General properties of PSAs used. 25
3.2 Mechanical properties of PMMA [75]. 25
3.3 Properties of the PETG filament [76, 77]. 28
3.4 Mechanical properties of steel 1.4310. 30
3.5 Properties of the PC filament [78]. 32

Nomenclature

List of Acronyms

CTOD	Crack Tip Opening Displacement
CTSD	Crack Tip Shear Displacement
CZM	Cohesive Zone Modelling
DCB	Double Cantilever Beam
DIC	Digital Image Correlation
ENF	End-Notched Flexure
FE	Finite Element
FEUP	Faculty of Engineering of the University of Porto
FPZ	Fracture Process Zone
PC	Polycarbonate
PETG	Polyethylene Terephthalate Glycol
PSA	Pressure-Sensitive Adhesive
SLJ	Single Lap Joint

List of Symbols

G	Energy release rate
G_c	Critical energy release rate
G_I	Energy release rate in mode I
G_{I_c}	Critical energy release rate in mode I
G_{II}	Energy release rate in mode II
G_{II_c}	Critical energy release rate in mode II
K	Stress intensity factor
K_c	Fracture toughness
σ_r	Remote stress
a	Crack length
E	Young's modulus
G'	Storage modulus

ν	Poisson's ratio
ϕ	Mode mixity ratio
J	J-integral
U	Strain energy density
T	Traction vector
u	Displacement
t_n^0	Tensile failure strength
t_s^0	Shear failure strength
ε_n	Tensile strain
ε_s	Shear strain
$\mathbf{t}$	Traction vector
ε	Strain tensor
$\mathbf{K}$	Element stiffness matrix
F	Force
b	Width of the specimen
θ_{up}	Rotation of the upper beam
θ_{lo}	Rotation of the lower beam
σ	Stress
τ	Shear stress
G_a	Adhesive fracture energy
U_{ext}	External work
U_s	Stored strain energy
U_{dt}	Energy lost in tensile deformation
U_{db}	Energy dissipated in bending
G_{eb}	Adhesive fracture energy considering only elastic bending
G_{db}	Energy dissipated due to plastic deformation
P	Peel load
θ	Peel angle
ε_y	Yield strain
W, U	Strain energy potential
J_{el}	Elastic volume ratio
$I_{1,2,3}$	Strain invariants
$\lambda_{1,2,3}$	Principal stretches

Chapter 1

Introduction

1.1 Background and motivation

Adhesives have revolutionised material joining in critical sectors, such as automotive and aeronautical industries, presenting an efficient alternative to traditional mechanical joining techniques like welding, brazing, bolting, and riveting. Adhesive usage can reduce structural weight, which minimises energy consumption and emissions, while enhancing load distribution and durability. Unlike conventional methods, adhesives allow for the seamless integration of dissimilar materials, offer greater design flexibility, and facilitate automated manufacturing processes.

Pressure-sensitive adhesives (PSAs) represent a versatile class of adhesives that form bonds when light pressure is applied without the need for heat, solvent, or water activation. This unique characteristic makes PSAs invaluable in a broad range of applications, including labels, tapes, and decals, as well as in critical industries such as medical, automotive, electronics, and construction. The inherent flexibility and ease of use of PSAs, coupled with their ability to bond a variety of surfaces instantly, positions them as a key adhesive technology. Their utility is underpinned by their viscoelastic nature, which allows them to maintain identical properties in tape or film forms, ensuring consistent performance across different applications.

Characterising PSAs involves evaluating properties like tack, shear adhesion, and peel adhesion, which is critical to understanding their bonding behaviour under different loading conditions.

1.2 Objectives

The main objective of this project is to understand the failure mechanism of different acrylic PSAs and develop a numerical model, resorting to cohesive zone modelling (CZM) that will allow for the accurate prediction of the fracture process of these materials, used in high-performance applications and electronic systems in the aeronautical and automotive fields.

This study involves manufacturing and testing double-cantilever beam (DCB) specimens bonded with PSAs to analyse their behaviour under tension and shear stresses, corresponding to loading

modes I and III, respectively. Furthermore, an apparatus is developed for peel testing under different angles and, therefore, to comprehensively assess these adhesives in a practical application setting.

This project uses the empirical data gathered from these tests to construct a robust numerical model that accurately predicts the adhesives' failure behaviour. The validation of this model involves comparing its predictions against the experimental results using identical specimen geometries and, subsequently, simulated outcomes using varied geometrical configurations. This comprehensive approach ensures a deep understanding of the adhesives' performance under different loading conditions. Some initial studies are also developed on hyperelastic models to characterise the mechanical behaviour of PSAs.

This dissertation is part of a broader project that aims to understand the behaviour of PSAs in diverse real-life applications. Therefore, in addition to understanding their failure modes, it is also necessary to understand their creep behaviour in order to comprehend the longevity of joints made with them. Thus, parallel to this thesis's primary task, two thermal chambers and three cyclic creep stations were also assembled to enable the future characterisation of these adhesives under creep and cyclic creep conditions at different temperatures.

1.3 Methodology

To accomplish the previously mentioned goals, a particular methodology had to be established, which is as follows:

- Conduct a thorough literature review on fracture mechanics and PSAs.
- Manufacture and test DCB specimens in mode I loading conditions to extract a cohesive law. Develop a Python code for data treatment and, later, implementation of the obtained cohesive law in a numerical finite element (FE) model.
- Next, a similar procedure to the one described in the previous point is used for mode III loading tests to obtain a cohesive law capable of predicting the failure mode in a shear plan.
- While doing the DCB testing, an apparatus similar to others available in the literature is developed and created for peel testing.
- A complete failure envelope of the peel load as a function of the loading angle is intended to be obtained through experimental tests. A cohesive law is estimated and implemented in a numerical model. To do that, the adhesion energy of the PSAs is extracted, and the peel-front process zone is characterised using digital image processing. This last step is accomplished by developing a Python code capable of processing the images recorded during testing.
- Using bulk tensile testing data from previous works, initial studies are developed in a numerical hyperelastic model.

- Additionally, throughout the entire duration of this thesis, two thermal chambers and three cyclic creep stations are to be developed.

1.4 Layout of the dissertation

This thesis is organised into seven primary chapters. Each chapter is detailed as follows:

- **Chapter 1** sets the stage for the thesis, outlining the background and motivation behind the research, the specific objectives aimed to be achieved, and the methodology employed to conduct the study.
- **Chapter 2** provides an extensive review of the current literature related to adhesive technologies, focusing on PSAs. This chapter discusses various adhesive classifications, failure modes, and the principles of fracture mechanics as they pertain to adhesive joints.
- **Chapter 3** details the experimental methodologies used to analyse the failure mechanisms of the PSAs. This includes the preparation of DCB and peel specimens, as well as the testing configurations used. The experimental results obtained are also exposed in this chapter.
- **Chapter 4** provides the numerical details used in the FE simulations. A CZM was used to predict the behaviour of the DCB specimens loaded in mode I and mode III, as well as for the peel tests. A hyperelastic numerical model is also explored in order to model the behaviour of single lap joints.
- **Chapter 5** discusses the design and process of developing the thermal chambers and cyclic creep stations.
- **Chapter 6** summarises the research findings, discussing the implications of the study and suggesting directions for future research. This chapter reflects on the challenges encountered during the research and the potential for upcoming advancements in adhesive technology.
- Finally, the scientific papers which result from this work are presented in the **Appendices**. The first paper entitled "Development of a cohesive zone model to characterise the fracture behaviour of PSAs" is presented in **Appendix** A, while the second paper, entitled "Experimental and numerical characterisation of the interface fracture behaviour of PSAs with peel tests" is available at **Appendix** B. In addition, the developed Python codes are presented here.

Chapter 2

Literature Review

2.1 Survey of adhesives

Adhesives can be defined as materials that establish a physical link between surfaces of other materials, capable of resisting separation forces [1]. Nevertheless, the general term "adhesive" refers to glue, cement, paste, and other substances [2].

The origins of adhesives can be traced to the pre-historic times when most adhesives were made from organic materials. In modern times, synthetic adhesives based on polymeric structures have revolutionised multiple industries, from the aerospace to consumer goods. Modern adhesives are used for a wide range of applications, from protective films and labels to structural parts, enhancing the performance and durability of vehicles and aircraft [2].

Adhesion can be described, in a simpler way, as the process of attraction between two substances originated from intermolecular forces established between them [1]. According to Wu et al. [3], adhesion is the condition where two dissimilar bodies are held together by close interfacial contact, allowing for the transfer of mechanical force or work across the interface. Van der Waals forces, chemical bonds, or electrostatic attraction can all contribute to the interfacial forces that hold the two phases together. The mechanical properties of the two bulk phases and the interfacial zone, in addition to the interfacial forces, determine the system's mechanical strength.

An adhesive joint results from joining two surfaces—either the same or different ones—by fillers and adhesives. Substrates are the materials that the adhesive bonds to before bonding. They are called adherends after they have bonded. The interphase is the space between the adherend and the adhesive, which includes the interface. In turn, the interface, also known as the boundary layer, is defined by the contact between the two materials and the surface [2].

When compared to traditional joining techniques, such as bolting, riveting, welding and brazing, adhesive bonding has several advantages [2, 4–6]:

- More uniform stress distribution, as represented in Figure 2.1, which increases stiffness and load transmission capacity and ensures weight and cost savings;
- Capability to bond thin sheets of material;

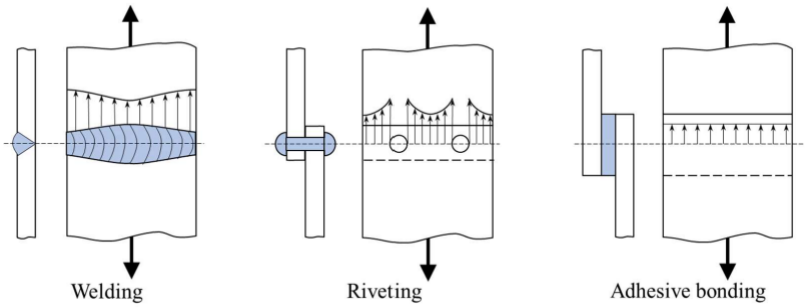


Figure 2.1: Stress fields obtained with three different joining methods. Welding (left), riveting (centre) and adhesive bonding (right) [1].

- The potential for automation of processes;
- Capability to easily join different materials;
- Flexibility in joint design;
- The potential for a smooth surface finish, possible due to the absence of holes and welding marks;
- Vibration damping and shock absorption capabilities.

Despite the benefits mentioned above, using adhesives comes with certain disadvantages, such as [2, 4–6]:

- Difficult visual examination of the bonded area, and consequently, difficult quality control;
- Low performance when exposed to cleavage and peeling stresses, which cause stress concentrations and reduce joint strength;
- Limited resilience to harsh environmental factors as a result of the adhesive's polymeric nature, such as high temperatures and humidity;
- The need for careful surface preparation;
- The requirement of specific equipment (e.g., holding fixtures, presses, ovens, and autoclaves)
- Adverse health effects resulting from exposure to cleaning solvents

2.1.1 Classification of adhesives

Adhesives can be classified according to different parameters: based on their polymer base, their function in the polymer "backbone", their physical form, their chemical composition, and their functional types [2].

According to the type of polymer base, adhesives can be natural or synthetic. Adhesives originating from natural sources comprise both vegetable and animal-based materials and natural gums, such as casein- and protein-based adhesives, animal glue, and natural rubber. On the other hand, synthetic adhesives include polyesters, silicones, epoxies, and acrylics [2, 7].

The polymer molecule's main chain, designated as the "backbone", is composed of repeating monomer units that are covalently bonded to one another. Since the "backbone" provides the framework to which side chains and functional groups are attached, it is crucial to define the polymer's overall structure and properties. Considering this, the adhesive's behaviour and functionality are determined by the polymer's "backbone" functionality, which can be thermosetting, thermoplastic, elastomeric, or hybrid [5]. Thermosetting adhesives are characterised by a curing process that is triggered by chemical reactions at different temperatures, resulting in a permanent hardening. Polyurethane, epoxy, and phenolic adhesives are a few examples of thermosetting adhesives. When exposed to heat, thermoplastic adhesives exhibit no hardening or cross-linking and can still melt without experiencing significant changes to their properties. Elastomeric adhesives are composed of polymers that exhibit characteristics similar to those of rubber and are distinguished by their unique rheological features [1, 2, 5, 8, 9]. Lastly, hybrid adhesives are a combination of the various types previously discussed.

The physical form, which typically specifies how the adhesive must be applied, can be liquid, paste, film, or powder. Liquid adhesives have good gap-filling properties and can be applied with rolls, sprays, or brushes. It is possible to use paste adhesives on vertical surfaces due to their high viscosity and minimal propensity to drip or sag. Film adhesives (like PSAs) are very easy to work with and guarantee a constant bond line thickness. Finally, powder adhesives must be heated or dissolved in a solvent to become liquid and applicable [2, 10].

Furthermore, the adhesives are divided into structural and non-structural types by the functional type. The former should guarantee high strength and performance, as the latter, including water-based adhesives, pressure-sensitive adhesives, and hot melt adhesives, among others, are unable to withstand high loads [11, 12].

Lastly, they can be classified as members of the chemical family epoxies, acrylics, and polyurethanes, among others. Epoxies are thermoset structural adhesives that are assumed to be the most adaptable because, although they are typically strong and brittle, they can be made to be tougher and more flexible without sacrificing their tensile strength. Although acrylics cure quickly and have a high strength, they are more expensive than epoxies. Furthermore, polyurethanes are sensitive to moisture and heat but remain strong and flexible even at low temperatures [2].

2.1.2 Failure modes and joint design

Three failure modes (cohesive failure in the adhesive, adhesive failure, and cohesive failure in the adherend) can occur in an adhesive joint with homogenous adherends. The following representations describe each failure mode:

- Cohesive failure occurs when an adhesive rupture occurs, but the interfaces are still intact, leaving some adhesive in both adherents [5].

- Adhesive failure, also referred to as interfacial failure, is usually the consequence of poor adhesion caused by insufficient surface preparation. In this instance, after the rupture, one of the substrates is still free of adhesive residue. Careful surface treatment methods, such as anodisation, grit blasting, plasma surface treatments, degreasing, and the use of adhesion-promoting primers, can frequently increase the quality of adhesion [13].

- Cohesive adherend failure consists in the collapse of the joint, despite the proper design and conception. This is, in fact, the result of a substrate failure, which indicates that, in this case, the adhesive and the interface are no longer the weakest part of the structural design.

Figure 2.2 shows the aforementioned failure modes.

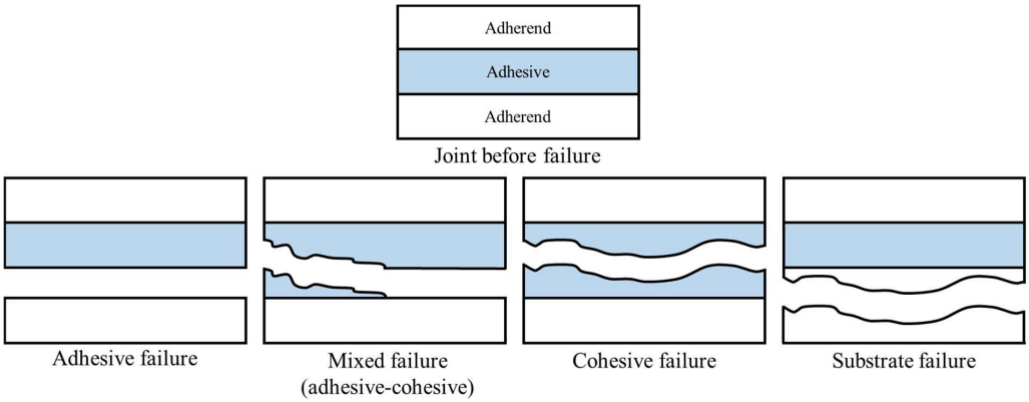


Figure 2.2: Schematic representation of cohesive and adhesive failures [8].

Multiple types of stress can be applied to adhesive joints while they are in use, which can have different effects on the adhesive layer. Understanding those stresses and how they differ from one another is crucial to ensuring a successful design [14]. As seen in Figure 2.3, there are, basically, four basic modes of loading: shear, tension, cleavage, and peel. These modes can be found in various real-life combinations or variations [12]. These include single-lap joints, double-lap joints, scarf joints, and stepped-lap joints, among others [1, 8]. Some of the most usual joint types are schematically depicted in Figure 2.4. Single-lap joints are the most popular due to their ease of use, practical efficiency and because they are the most representative of real applications.

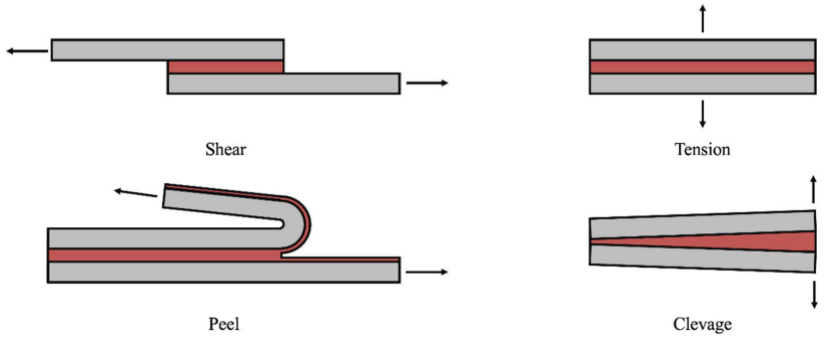


Figure 2.3: Main types of loadings acting in adhesive joints [8].

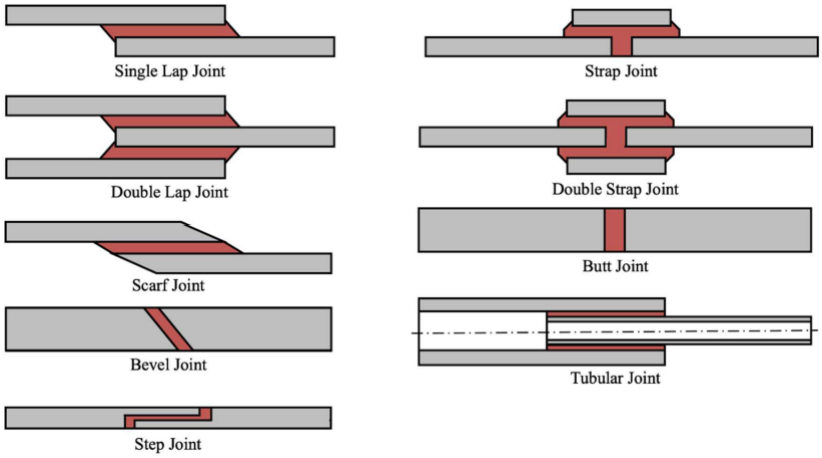


Figure 2.4: Examples of joint configurations [8].

2.2 Failure prediction approaches

As exposed previously, adhesive joints may be subjected to multiple loading conditions. Only accounting for the mechanical loads to predict adhesive joint failure is insufficient, as it neglects other factors like intangible flaws, crack formation, and environmental conditions. Several methods have been created over time to account for these and other factors, including continuum mechanics, fracture mechanics, and damage mechanics.

2.2.1 Continuum mechanics

The continuum mechanics method ignores the particular properties of the adherents and assumes a perfect bond at the interface by treating both as continuous materials [15]. In order to determine whether a failure has occurred, the adhesive's calculated stresses and strains are compared to the mechanical properties of the material, usually using criteria like maximum stress or maximum strain. However, the mesh size affects these computations, and because of that, singularity points like overlap edges could appear [16]. Figure 2.5 illustrates these singularities. The application

of the Finite Element Analysis (FEA) prevents the existence of convergence because of the increasing stresses as the mesh becomes more refined since, according to the linear elastic analysis, these singularities have corresponding infinite stress values. Numerous authors have attempted to address this issue, but their solutions are limited to continuum structures and cannot be used to characterise defects in other materials [11, 15, 17].

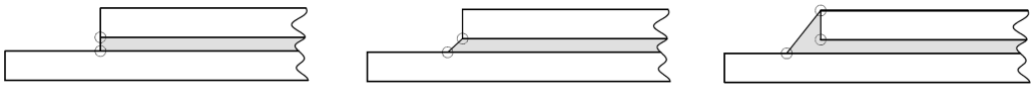


Figure 2.5: Singularities in the proximity of an adhesive edge. Adapted from [18].

2.2.2 Fracture mechanics

Cracks and other defects in materials, including manufacturing defects, are specifically taken into account by the fracture mechanics approach, which considers them as discontinuities. This method provides a quantitative analysis of the behaviour of cracks in structures, allowing for the evaluation of the crack's propagation and the determination of whether the crack's size surpasses the critical failure size or not. The incapacity of this model to accurately represent the beginning of damage is one of its limitations. It is better suited for researching how damage propagates rather than examining how damage first grows. A stress intensity factor criterion and an energy release rate are commonly employed in this methodology [15, 19].

Energy release rate criterion

An energy-based criterion considers that the propagation of cracks occurs when the available energy, G, the energy release rate, which is dependent on the applied load, equals a critical value, the critical energy release rate or G_c (a material property) [18]. Therefore, Equation 2.1 represents the condition to prevent crack propagation [15].

$$G \leq G_c \tag{2.1}$$

Stress intensity factor criterion

In stress intensity factor analysis, K is a scaling parameter that shows the distribution of stress in a discontinuous cracked material surrounding the crack tip. It also measures the potential that a crack has for propagation. Stress intensity factor can be represented according to Equation 2.2 [15].

$$K = Y\sigma_r\sqrt{\pi a} \tag{2.2}$$

, where Y is a non-dimensional factor that is dependent on the loading distribution and geometry, σ_r is a remote stress that is applied perpendicularly to the crack length, a. Crack propagation

will occur when the stress intensity factor, K, is equal to a critical value, the material fracture toughness K_c [15].

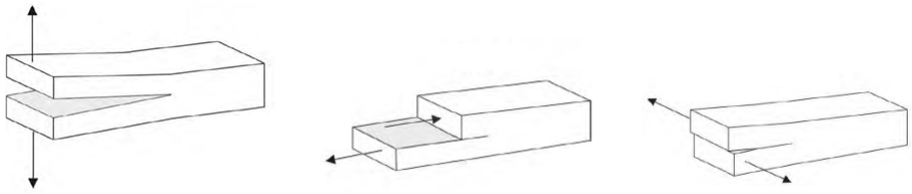
The two previously mentioned criteria can be related by Equations 2.3 and 2.4, for plane stress and plane strain conditions, respectively [20]:

$$G = \frac{K^2}{E} \tag{2.3}$$

$$G = \frac{K^2}{E}(1-\nu^2) \tag{2.4}$$

where E is the Young's modulus and ν is the Poisson's ratio.

There are three modes that the crack can propagate in, as illustrated in Figure 2.6. The opening mode, which is represented by Mode I, and two shear modes, which are represented by Mode II and III for in-plane and out-of-plane shear, respectively [12, 15].



(a) Mode I. (b) Mode II. (c) Mode III.

Figure 2.6: Fracture modes for an adhesive joint [18].

Under real-life applications, joints are not usually loaded in pure loading conditions. Therefore, it is important to be able to characterise joints in mixed-mode conditions. This mode mixity can be represented by a mode ratio, given by Equation 2.5 [15].

$$\phi = \tan^{-1}\left(\frac{G_{II}}{G_I}\right) \tag{2.5}$$

The combination of the effects of both modes is required to determine crack propagation in mixed modes. Equation 2.6 provides this relationship [15].

$$\left(\frac{G_I}{G_{Ic}}\right)^{\alpha} + \left(\frac{G_{II}}{G_{IIc}}\right)^{\beta} = 1 \tag{2.6}$$

where G_{I_c} is the critical energy release rate in mode I, G_{II_c} is the critical energy release rate in mode II and α and β are constants.

J-Integral approach

The J-integral, initially developed by Rice [21], is a contour integral that is independent of the path and can be employed to evaluate near-crack-tip deformation in both linear and non-linear elastic materials. The concept that crack propagation requires a critical value of the J-integral, J_c, forms

the basis for the use of J to characterise fracture [22]. The J-integral can be described according to Equation 2.7

$$J = \int_{\tau} \left(U\,dy - T\frac{\partial u}{\partial x}\,d\tau \right) \tag{2.7}$$

where U, T, and u represent the strain energy density, the vectors of traction perpendicular to the integration contour τ, and displacement, respectively.

One of the most important characteristics that make the J-integral a robust and versatile tool in fracture mechanics is its independence from the chosen contour of integration. Rice [21] rigorously demonstrated this property, showing that for both elastic and elastoplastic materials, the value of the J-integral remains constant regardless of the path taken around the crack tip, provided certain conditions are met.

The conditions required to maintain the contour independence of the J-integral are as follows [21, 23]:

- The integration contour (τ in Equation 2.7), must surround the crack tip.
- The elastic deformation energy, represented by U, should not explicitly depend on the x-coordinate. This implies that the mechanical energy stored in the material should be uniform in the direction parallel to the crack, allowing for a consistent evaluation of energy release irrespective of the chosen path.
- There should be no objects that may alter the body's energy if moved in the x direction inside the contour.

Biel and Stigh [24] considered this characteristic by employing multiple alternative contours as well as the J-integral approach. Thus, according to the authors' observations, the two contours that assumed elastic deformation in the substrates in the presence of plasticity were less accurate.

These conditions ensure that the J-integral accurately measures the energy release rate associated with crack propagation without being influenced by the specific path of integration. This property is particularly valuable in practical applications, where the precise geometry and conditions near the crack tip may be complex and irregular.

By measuring a displacement in close proximity to the crack tip, crack tip opening displacement (CTOD) offers a straightforward way to characterise the stress and deformation fields at the crack tip [25]. To measure this parameter, different solutions are proposed in the literature, and these include strain gauge sensors [26], optical tracking [27], luminescence [28], and acoustic emission [29]. Since it allows for the precise measurement of the local displacement/strain close to the crack tip, the digital image correlation (DIC) technique has recently gained much popularity. DIC is a powerful, non-contact optical method used to measure displacement and strain fields on the surface of materials under load. In fracture mechanics, DIC is employed to accurately capture the CTOD by tracking the movement of speckle patterns applied to the specimen surface. This method can help with the direct extraction of the cohesive law.

2.2.3 Damage mechanics

Damage mechanics studies the initiation and propagation of damage by taking into account continuum mechanics and fracture mechanics, respectively. For studies of this nature, a cohesive zone model (CZM) is typically employed. Generally, CZMs are based on non-thick elements that define the boundary between two solid surfaces. When a stress criterion is satisfied, a relaxation process based on the fracture energy criterion, which is used to simulate material degradation, begins for each of those elements [15].

When an element reaches a certain level of stress, a CZM element exhibits damage, leading to a reduction in both stiffness and strength. These elements are linked via cohesive traction and relative displacement, facilitating the simulation of elastic behaviour [30]. This behaviour is linearly defined within the CZM for all laws until reaching critical thresholds for tension (t_n^0) or shear (t_s^0), as shown in Figure 2.7 [16].

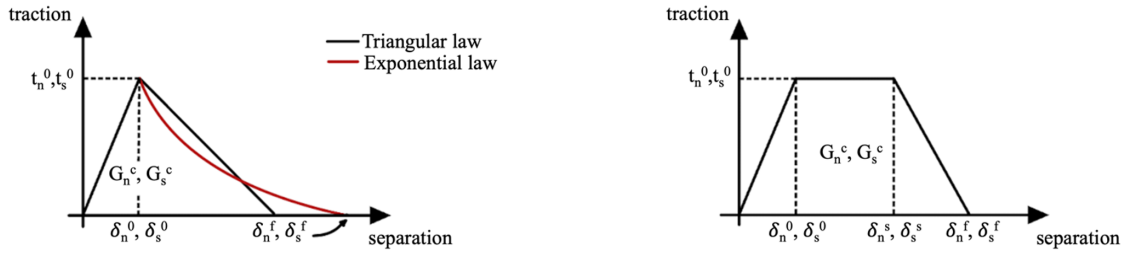


Figure 2.7: Schematic representation of different cohesive law shapes: triangular or exponential (left) and trapezoidal (right). Adapted from [16].

The elastic response of cohesive elements is governed by an elastic constitutive matrix, correlating stress and strain in tension and shear:

$$\mathbf{t} = \begin{bmatrix} t_n \\ t_s \end{bmatrix} = \begin{bmatrix} K_{nn} & K_{ns} \\ K_{ns} & K_{ss} \end{bmatrix} \begin{bmatrix} \varepsilon_n \\ \varepsilon_s \end{bmatrix} = \mathbf{K}\boldsymbol{\varepsilon} \tag{2.8}$$

Damage initiation can be dictated by different criteria, including the quadratic nominal stress criterion, a commonly employed method, calculated as:

$$\left\{ \frac{\langle t_n \rangle}{t_n^0} \right\}^2 + \left\{ \frac{t_s}{t_s^0} \right\}^2 = 1 \tag{2.9}$$

In Equations 2.8 and 2.9, t_n and t_s denote the cohesive tractions in tension and shear, respectively, while ε_n and ε_s are the corresponding strains. The use of Macaulay brackets indicates that compressive stresses are excluded from initiating damage [16, 31]. Fulfilment of this criterion leads to material degradation, culminating in softening as prescribed by the CZM until failure occurs. The fundamentals of damage accumulation and the integration of cohesive elements into the mesh are depicted in Figure 2.8.

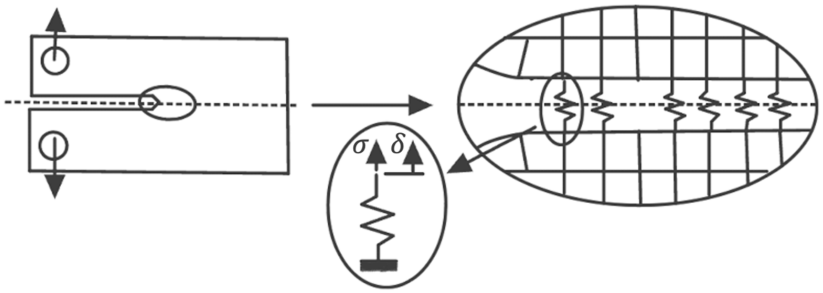


Figure 2.8: Operating principle of a CZM. Adapted from [1].

2.3 Pressure-sensitive adhesives (PSAs)

Pressure-sensitive adhesives are a unique class of adhesives that bond to a variety of surfaces when light pressure is applied, such as finger pressure, without the need for heat, solvent or water activation, as is the case for other adhesives. This property makes PSAs extremely versatile and useful for a wide range of applications, including labels, tapes, and decals, and important for different industries, such as medical, automotive, electronic and construction [32].

This singular characteristic is explained by the fact that PSAs do not suffer physical changes, having, because of that, identical properties both in the bonded joint and in tapes or films. Whereas other types of adhesives are usually applied in the liquid state and then hardened into a solid state, promoting, first, a wetting of the surface and, posteriorly, a good bonding resistance, a PSA, being a viscoelastic material and presenting a viscous solid or soft solid state, allows, immediately, not only good wetting and bonding properties (due to the liquid-like behaviour of the tape or film) but also a good stiffness and debonding resistance (due to the solid-like behaviour) [32, 33].

In order to properly define a PSA, the Pressure Sensitive Tape Council created the following qualitative criteria that must be present in the material for it to be considered a PSA:

- Aggressive and permanently tacky;
- Adherence without the need for more than finger or hand pressure;
- No requirement for activation by water, solvent or heat;
- Ability to exert a strong holding force;
- Sufficient cohesiveness and elasticity so that it can be removed from smooth surfaces without leaving a residue.

Regarding the categorisation of the polymer base used, PSAs can be divided into acrylic, rubber, silicone and polyurethane. First, acrylic PSAs are composed of acrylic-based polymers and exhibit excellent ageing characteristics, UV resistance, and environmental stability, maintaining their adhesive properties over a wide temperature range and having the advantage of good transparency. Secondly, rubber PSAs are composed of rubber-based polymers and present great

flexibility, conformability and ability to bond to a large variety of substrates despite not being as resistant as the previous ones to different environments. Additionally, silicone PSAs are composed of silicone-based polymers and offer excellent thermal stability, chemical resistance and electrical insulation properties, retaining adhesion at both very high and very low temperatures. Lastly, polyurethane PSAs are composed of polyurethane-based polymers and provide good flexibility, durability and resistance to wear and chemicals [32].

PSA's advantages include the ease of handling and bond assembly, the simplicity of processing with the associated time and cost reduction, the ability to bond to most substrates, the environmental resistance, the flexibility in their formulation and the durability of their bond. On the other hand, PSAs are associated with a lower load capability, a propensity to creep and a limited bond thickness tolerance [32, 33].

2.3.1 Characterisation of PSAs

PSAs are characterised through various properties and performance metrics. However, the key aspects to characterise them are: tack, shear adhesion, and peel adhesion [2, 32–34].

Firstly, tack measures the initial adhesion capacity of a PSA, evaluating how quickly it bonds to a surface under light pressure. Thus, tack tests, such as loop tack and probe tack, aim to quantify tack by assessing the ability of adhesion to the adhesive under low-pressure conditions. These types of tests are crucial when studying PSAs since they do not undergo any activation process, which means that the result of these tests provides information about the adhesion strength in service [32, 33].

Secondly, shear adhesion assesses the adhesive's resistance to sliding forces parallel to the bonding surface, indicating internal cohesion. Therefore, shear adhesion tests involve applying a constant force to the bond line in a direction parallel to the bonding interface and measuring the force at which the adhesive fails [32, 33].

Lastly, peel adhesion measures the force required to peel the adhesive from the surface at a specified angle and speed, reflecting the bond strength. To that end, various tests, like 180-degree and 90-degree peel tests, are performed to evaluate the force required to break the bond. The results are generally reported as the average or maximum force needed to peel the material from the surface or as the work required to remove a specified length of material [2, 32].

2.3.2 Adhesion mechanisms of PSAs

The adhesive properties of PSAs are fundamentally influenced by their viscoelastic and non-Newtonian flow behaviour. This rheological characteristic is based on modulus components that vary with time and temperature, manifesting in practical applications, such as time, stress and temperature-dependent bonding phenomena like dwell time.

In viscoelastic materials, the process of bonding and debonding is not fully reversible from an energetic standpoint. The deformation energy partly dissipates through viscous flow, which is

time-dependent, leading to a delay between stress and strain. Consequently, establishing effective contact requires a specific dwell time, and creep phenomena can occur during both bonding and debonding [35]. Therefore, PSAs exhibit a nuanced interplay of molecular interactions, rheological properties, surface characteristics and chemical dynamics, collectively influencing their performance across various applications. Unlike most adhesives that rely on static properties to adhere to a surface, PSA's behaviour is highly dependent on rheological factors since once initial tack has occurred, the adhesive strength increases due to slow flow processes [35–37]. Additionally, PSAs demonstrate good water resistance, which cannot be solely attributed to the physical bonds formed, suggesting that additional adhesion mechanisms are taking place, such as forming new bonds to replace those disrupted by environmental factors, thanks to their high viscosity and molecular mobility [36].

Moreover, these viscoelastic properties make it possible for PSAs to maintain their adhesive qualities without changing physical states or requiring curing techniques. This characteristic facilitates not only good wetting and adhesion but also good cohesion properties [32]. Nevertheless, it is important to note that, because of these properties, there is always a compromise between the strength of the adhesive and the wetting capability while remaining in the same state. In other words, this balance between intermolecular forces for adhesion and cohesion determines the properties and the behaviour of the PSA [38].

Thus, the performance of PSAs is influenced by many factors, like polymer molecular weight, branching, crosslinking, and the overall formulation. For instance, harder compositions or high glass transition temperature (T_g) require low molecular weight to maintain good wettability, while softer compositions need higher molecular weight to ensure sufficient cohesive strength. Beyond that, higher levels of branching also improve adhesion. Crosslinking and the presence of tackifiers are associated with higher cohesive strength but worse adhesion potential [39].

2.3.3 Effect of joint design and testing parameters in performance of PSAs

It is crucial to comprehend PSA behaviour and the various factors that affect its strength and performance in order to adjust the joint design and loading conditions to achieve optimal performance in service. The general performance of adhesives, which PSAs are a part of, depends on several factors related to the joint geometry and the testing conditions [40]. Some of those variables are listed below:

- Combination of materials in adhesive and adherend.
- Adhesive properties such as stiffness, glass transition temperature T_g, viscosity, and others.
- Thickness of the adhesive layer.
- Surface roughness.
- Assembly conditions such as applied load, temperature, and moisture.
- Loading conditions including peel, shear, tensile, and others.

To further complicate the description of the influence of these variables and others, the interdependency of these different variables must be considered. For instance, while stronger joints using a soft PSA (G' = 10 kPa) can be achieved with small-scale surface roughness compared to smooth surfaces, stiffer PSAs (G' = 80 kPa) or large-scale roughness are detrimental to joint strength [40, 41].

Thickness

The thickness of the adhesive layer in PSAs plays a crucial and complex role in their performance since it is influenced by various factors such as loading conditions, PSA type, applied load, and assembly time.

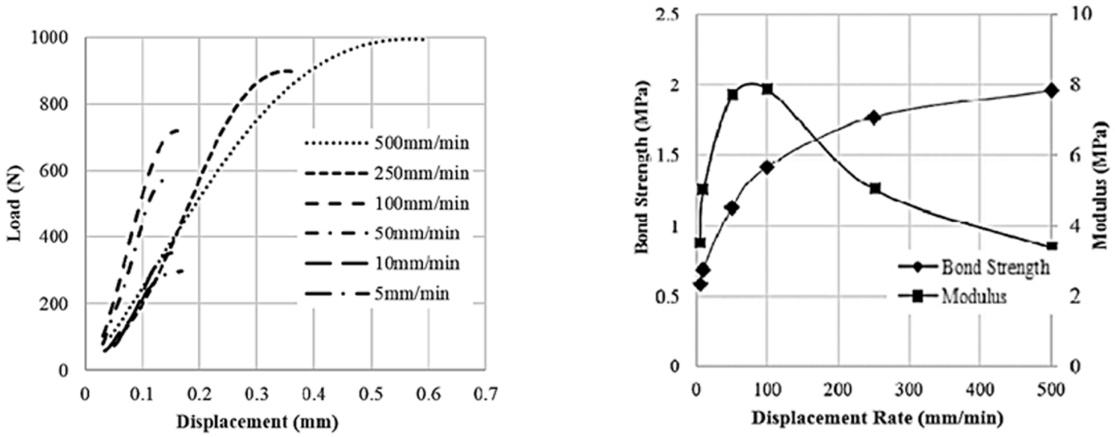
Firstly, the tack force of a PSA is significantly influenced by the thickness of the adhesive layer. As the thickness increases, the initial stickiness or tack of the adhesive can change, impacting how quickly and effectively the adhesive forms a bond under light pressure. Notwithstanding, Tordjeman et al. [42], show that the relationship between thickness and tack properties is not that straightforward since it was found to be a non-monotonic behaviour, meaning that the tack force does not consistently increase or decrease with adhesive thickness. However, when thickness and applied load during assembly increased, the tack energy also increased. The same effect was also observed for the bonding area.

Thus, it is essential to consider other factors. On the one hand, the applied load is extremely important, as a higher applied load leads to an increased actual bonding area. On the other hand, the type of PSA used also matters since PSAs with better wetting properties can better flow into surface cavities, enhancing bonding, particularly under higher applied loads [42].

Loading stress and loading rate

In most materials, when stress is applied to a joint, the rate of deformation increases, and the duration the joint can sustain the load decreases. However, for viscoelastic materials, like PSAs, the deformation or loading rate has an additional impact.

Consequently, it was found that, in viscoelastic materials, like PSAs, a higher loading rate leads, typically, to an increased strength associated with a decreased failure strain [43, 44]. This property of this type of adhesive is attributed to a delay in the cavitation (the formation and subsequent collapse of gaps or bubbles within the material, usually as a result of applied stress or pressure) when higher deformation rates are in place. Moreover, it was also studied that a more pronounced hardening effect is associated with a higher loading rate. Even more, a study done in [44] with acrylic PSAs showed that when the loading rate is increased, the bond strength also increases, as well as the modulus, which rises until a peak of around 100 mm/min is reached. This is illustrated in Figure 2.9.



(a) (b)

Figure 2.9: (a) Tensile load-displacement responses, and (b) Strength and modulus properties at different loading rates. Adapted from [44].

Nevertheless, it is important to note that the loading rate also influences the failure mode of PSAs. For instance, the occurrence of an adhesive failure is more common at low rates than at higher rates. In this last condition, a cohesive failure will be predominant [44]. This particularity can be explained by the fact that these adhesives, because of their viscous properties, behave like a dashpot or shock absorber, so the load is dependent on the deformation rate and not on the deformation, as happens on a linear spring. Consequently, the behaviour of the adhesive, whether it is liquid-like, rubber-like or glassy-like, is dependent on the deformation rate [45].

Surface roughness

The effect of surface roughness on PSAs can be either beneficial or detrimental, depending on the roughness scale and the PSA's ability to deform and wet the surface, including valleys and pits [41].

For soft adhesives, low roughness can be advantageous over smooth surfaces due to increased mechanical interlocking and enhanced contact area. However, high roughness can also create voids and reduce resistance by reducing the actual bonding area and introducing initial defects [46]. Additionally, it was also discovered that surface roughness influences the debonding process, as well, since it plays a crucial role in initiating and propagating fracture.

Studies about the influence of surface roughness in different types of PSAs (including a flexible core (FC), a rigid foam (RF), and a flexible foam (FF)) revealed that lower roughness values (Ra = 0.21 μm), corresponding to an ungrounded surface) enhance the ultimate shear strength for both rigid and flexible foam adhesives. However, it was also shown that all roughness values lead to minimal differences for the acrylic core adhesive (FC). Similarly, the flexible foam adhesive showed little variation for higher roughness values, indicating an undefined relationship between surface roughness and final shear strength. Nevertheless, using an adhesion promoter before assembly improved shear strength and cohesion [47].

2.3.4 Cohesive law estimation through DCB testing

The Cohesive Zone Model (CZM) has demonstrated efficacy in predicting the strength of adhesively bonded structures, particularly within the aeronautical industry [48]. This model utilises a cohesive law that specifies the tractions exerted by the substrates onto the adhesive surfaces, essentially representing the adhesive's material volume properties. The cohesive law fundamentally depends on the separation of the bonded surfaces, as discussed extensively by Yang and Thouless [49] and Stigh et al. [50].

The cohesive law describes the relationship between the traction vector components and the separation vector of the surfaces. Theoretical groundwork for measuring these laws using the Double Cantilever Beam (DCB) specimen has been laid by Olsson and Stigh [51]. In this project, the cohesive law is derived through the direct method.

The direct method assumes that during stable crack propagation, the Fracture Process Zone (FPZ) translates in a self-similar manner along the specimen ahead of the crack tip. The cohesive law is then deduced by differentiating the fracture toughness with respect to the initial crack tip opening displacement [52].

In DCB specimen configurations, stable mode I crack growth is facilitated by loading through transversal forces F [48]. The J-integral is calculated as follows:

$$J = \frac{1}{b} F(\theta_{up} - \theta_{lo}), \tag{2.10}$$

where θ represents the rotation at the loading points (for the upper (up) and lower (lo) beams, and b is the width of the crack propagation region.

Choosing the integration path τ vertically simplifies the calculation since $d\tau = dy$ and the tractions T at the free edge are zero. Considering w as the CTOD, the J-integral can be described as:

$$J = \int_0^{w_0} \sigma(w)\, dw. \tag{2.11}$$

Here, w_o is the critical CTOD (when traction becomes 0) and σ is identified as the average cohesive stress across the tape thickness, facilitating the determination of the cohesive law $\sigma(w)$ by differentiating J with respect to w. This setup assumes nearly uniaxial strain due to stiff adherends, ensuring path independence of J.

Combining Equations 2.10 and 2.11, the cohesive law is obtained:

$$\sigma = \frac{\partial J}{\partial w} = \frac{1}{b} \frac{\partial}{\partial w} F(\theta_{up} - \theta_{lo}) \tag{2.12}$$

2.3.5 Peel testing in PSAs

The peel test is widely used in the packaging and electronics industries to evaluate the failure of flexible laminates. A lot of research has been done on this test, examining a variety of factors, including peel angle, material thickness, intrinsic adhesion, and the effects of test rates and temperatures [53, 54]. Tensile deformation of the peeling arm is also a parameter of major importance

as this may have an impact on the energy available for debonding [55]. Kinloch et al. [56, 57] have studied the effects of the backing tape on the fracture energy of flexible adhesives and proposed this as a characteristic parameter of the adhesive's peeling behaviour that is independent of the geometric details of the test.

Adhesive energy

The adhesive fracture energy, G_a, is determined through an energy balance approach, expressed as:

$$G_a = \frac{1}{b}\left(\frac{dU_{\text{ext}}}{da} - \frac{dU_s}{da} - \frac{dU_{dt}}{da} - \frac{dU_{db}}{da}\right), \tag{2.13}$$

where dU_{ext}, dU_s, dU_{dt}, and dU_{db} represent the external work, stored strain energy, energy lost in tensile deformation, and energy dissipated in bending, respectively. G_a reflects both the interfacial bonding energy and local energy dissipation [56].

For a simplified model with an inextensible backing to the peeling arm, reducing elastic deformation, the adhesive fracture energy under a load P and peel angle θ is given by:

$$G_a^{\infty} = \frac{P}{b}(1-\cos\theta). \tag{2.14}$$

In cases where the peel arm is extensible, for an arm of thickness h and width b, the modified equation considering tensile strain ε_a in the arm is:

$$G_a^{\text{eb}} = \frac{P}{b}(1+\varepsilon_a-\cos\theta) - h\int_0^{\varepsilon_a}\sigma\, d\varepsilon, \tag{2.15}$$

and the maximal elastic energy, assuming no work hardening, is defined as:

$$G_{\max}^{e} = \frac{1}{2}(\sigma_y\varepsilon_y h) = \frac{1}{2}(E\varepsilon_y^2 h), \tag{2.16}$$

where ε_y is the yield strain and E the Young's modulus of the peeling arm.

The determination of the critical energy release rate, G_c, in scenarios where plastic or viscoelastic bending occurs near the crack front, requires accounting for associated energy losses to ensure the accuracy of energy calculations necessary for crack propagation [58]. Gent and Hamed, [59–61], emphasise the importance of incorporating these energy losses in the overall energy balance by demonstrating how both elastic and plastic bending work together to cause notable curvatures close to the debond tip.

To accurately model the energy dissipation due to bending, G_{db}, several material characterisations of the peel arm have been utilised:

- as a non-work-hardening, elastic-perfectly plastic material,
- as a bilinear work-hardening, elastic-plastic material,
- as a power-law work-hardening, elastic-plastic material.

The appropriate stress-strain relationships for these materials are then integrated into analytical formulas derived for G_{db}. These formulas are the product of extensive theoretical work involving large displacement beam theory, which accommodates elastic-plastic loading and unloading, as well as root rotation at the peel front [56, 62, 63]. This comprehensive approach has been validated and extended in various studies, enhancing the understanding of the mechanics involved in peel arm dynamics and their implications for adhesive performance [58].

The total work done by external forces is adjusted for the energy dissipated due to plastic deformation in the backing substrate, represented as G_{db}. Thus, the adjusted fracture energy, G_a, considering these losses, can be mathematically expressed as:

$$G_a = G_a^{\text{eb}} - G_{\text{db}} \tag{2.17}$$

where G_a^{eb} represents the initial calculated adhesive fracture energy before accounting for bending dissipation.

2.3.6 Numerical modelling of hyperelasticity in PSAs

The significant deformation levels that PSAs can achieve before failure can be defined by hyperelastic models. Complex mathematical expressions based on the theory of large deformations serve as the foundation for the constitutive models of hyperelastic materials [64, 65]. Different tests may be needed to determine the constitutive parameters of the material in order to define the input requirements of the models [66–68].

Hyperelasticity represents a critical property in certain materials, enabling them to undergo significant deformations without internal energy dissipation. This characteristic is notably present in elastomers, polymers, rubber, and various biological tissues. Unlike other materials that exhibit energy loss during deformation, hyperelastic materials can store and fully recover the applied energy upon load removal. The capacity of hyperelastic materials to revert to their original state after extensive deformations, without energy loss, positions them as essential components in diverse applications, such as medical devices and automotive components [69, 70].

Hyperelastic material models are used to simulate the elastic behaviour of large deformations. In these models, the stiffness varies as the specimen deforms, and the internal energy stored in the elastic domain of the material is fully recovered upon unloading. The strain energy potential, or the strain energy stored in the material, is thus defined by hyperelastic models through equations and expressions. In the case that a stress-strain curve is available, the region beneath the curve represents the strain energy [71–73].

Several models have been developed to simulate the phenomenological behaviour of hyperelastic materials. The most popular hyperelastic models are described below according to the ABAQUS documentation [74]:

- **Arruda-Boyce** form:

$$U = \mu \left\{ \frac{1}{2}(\bar{I}_1 - 3) + \frac{1}{20\lambda_m^2}\left(\bar{I}_1^2 - 9\right) + \frac{11}{1050\lambda_m^4}\left(\bar{I}_1^3 - 27\right) + \frac{19}{7000\lambda_m^6}\left(\bar{I}_1^4 - 81\right) + \right.$$
$$\left. + \frac{519}{673750\lambda_m^8}\left(\left(\bar{I}_1^5 - 243\right)\right) \right\} + \frac{1}{D}\left(\frac{J_{e\ell}^2 - 1}{2} - \ln J_{e\ell}\right)$$

- **Marlow** form:

$$U = U_{dev}(\bar{I}_1) + U_{vol}(J_{el})$$

- **Mooney-Rivlin** form:

$$U = C_{10}(\bar{I}_1 - 3) + C_{01}(\bar{I}_2 - 3) + \frac{1}{D_1}(J^{el} - 1)^2$$

- **Neo-Hookean** form:

$$U = C_{10}(\bar{I}_1 - 3) + \frac{1}{D_1}(J^{el} - 1)^2$$

- **Ogden** form:

$$U = \sum_{i=1}^{N} \frac{2\mu_i}{\alpha_i^2}\left(\bar{\lambda}_1^{\alpha_i} + \bar{\lambda}_2^{\alpha_i} + \bar{\lambda}_3^{\alpha_i} - 3\right) + \sum_{i=1}^{N} \frac{1}{D_1}(J^{el} - 1)^{2i}$$

- **Polynomial** form:

$$U = \sum_{i+j=1}^{N} C_{ij}(\bar{I}_1 - 3)^i (\bar{I}_2 - 3)^i + \sum_{i=1}^{N} \frac{1}{D_1}(J^{el} - 1)^{2i}$$

- **Reduced polynomial** form:

$$U = \sum_{i+j=1}^{N} C_{i0}(\bar{I}_1 - 3)^i + \sum_{i=1}^{N} \frac{1}{D_1}(J^{el} - 1)^{2i}$$

- **Van der Waals** form:

$$U = \mu \left\{ -\left(\lambda_m^2 - 3\right)[\ln(1-\eta) + \eta] - \frac{2}{3}a\left(\frac{\tilde{I} - 3}{2}\right)^{\frac{3}{2}} \right\} + \frac{1}{D}\left(\frac{J_{e\ell}^2 - 1}{2} - \ln J_{e\ell}\right)$$

- **Yeoh** form:

$$U = C_{10}(\bar{I}_1 - 3) + C_{20}(\bar{I}_1 - 3)^2 + C_{30}(\bar{I}_1 - 3)^3 + \frac{1}{D_1}\left(J^{e\ell} - 1\right)^2 + \frac{1}{D_2}\left(J^{e\ell} - 1\right)^4 + \frac{1}{D_3}\left(J^{e\ell} - 1\right)^6$$

In the models listed above, the coefficients D_i and C_{ij} are material parameters obtained through experimental data. Due to hyperelastic materials' inherently nonlinear behaviour characteristics, it is essential to have experimental data in tension, compression, and shear modes of deformation. These modes collectively capture the material's response to changes in shape and volume.

The deviatoric response pertains to alterations in shape without concurrent volume changes, while the volumetric response signifies variations in volume devoid of alterations in shape. Together, these responses provide a holistic understanding of how the material behaves under different loading conditions. The deviatoric strain invariants ($\bar{I}$) are expressed as functions of the deviatoric stretches ($\bar{\lambda}_i$), offering mathematical representations of the material's deformation under stress. Additionally, the elastic volume ratio (J^{el}) quantifies the material's volume change during elastic deformation [40].

Chapter 3

Experimental procedures

This chapter details the materials and experimental procedures used in this project. The adhesives under study were tested in modes I and III, using specimens based on DCBs geometries. Adhesives were also tested in peel to determine their failure modes.

3.1 Materials

In this work, two different double-sided acrylic PSAs were studied: Adhesive A, made of a highly shock-absorbing black acrylic foam, and Adhesive B, grey acrylic foam. The properties of these two adhesives were provided in the manufacturers' datasheets, and they are reported in Table 3.1.

Table 3.1: General properties of PSAs used.

Adhesive	A	B
Poisson's ratio	0.499	0.499
Thickness [mm]	0.3	1.1

The substrates used in this project were made of PMMA, commonly called acrylic. This optically clear material, in opposition to metal substrates like aluminium or steel, has the advantage of allowing easier identification of defects and trapped bubbles in the interface between this and the adhesive layer, facilitating the study of the failure mode of the adhesives. Additionally, PMMA has smooth and flat surfaces. The mechanical properties of PMMA are summarised in table 3.2 [75].

Table 3.2: Mechanical properties of PMMA [75].

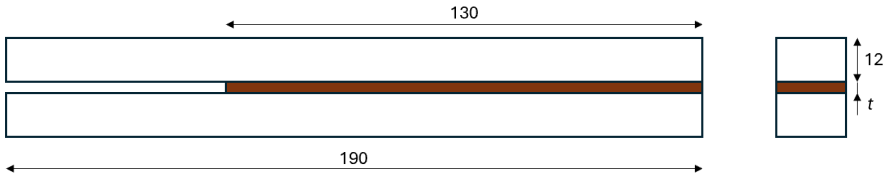
Density	Young's modulus	Poisson's ratio
1200 kg/m^3	1.8 - 3.2 GPa	0.35 - 0.4

3.2 Specimen manufacturing

3.2.1 DCB specimens

DCB specimens were produced to perform both pure mode I and mode III tests in order to obtain the fracture energy and cohesive laws of the acrylic PSAs in tensile and shear, respectively. Isopropyl alcohol was used to clean the PMMA substrates to eliminate any residues and grease that could be in the material and interfere with the adhesion process. The geometry of the DCB's specimens was based on the work developed in [48], and it is presented in Figure 3.1, where t is the thickness of the adhesive tape. The surface of the specimens near the crack tip was coated with white matte paint and speckled with black dots to allow for a further DIC analysis.

Figure 3.1: DCB specimen geometry, in mm.



For the mode I test, in order to load the DCB while allowing it to rotate freely, two steel blocks were bonded to the substrates using a two-component polyurethane structural adhesive (SikaForce® - 325 TC L 60). This adhesive, according to the manufacturer, presents a density of 1830 g/m^3 and a tensile strength of 15 MPa.

Figure 3.2 represents the DCB specimen for the mode I test. A 50 mm initial crack length and a 130 mm length of the DCB bonded with the PSA are sufficient to guarantee that the specimen's end is virtually unloaded, which is a requirement of the method used to measure the fracture energy.

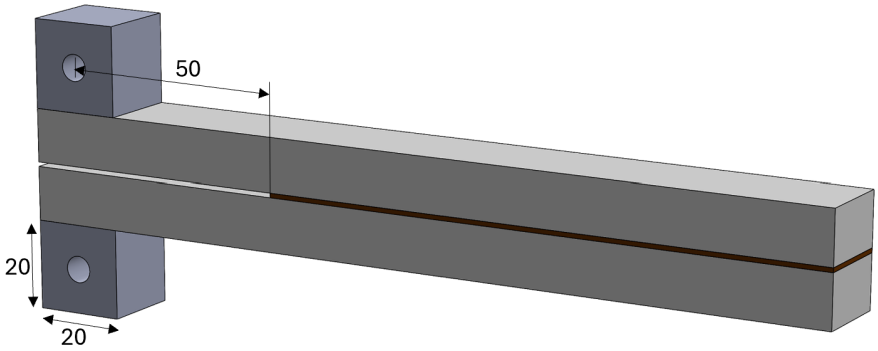


Figure 3.2: DCB specimen configuration for mode I test, in mm.

Sandblasting was performed in the face of the steel blocks that stayed in contact with the PMMA adherents. This surface treatment aimed to create a rougher surface to improve the bond

between these two material surfaces. Sandblasting was performed at a distance of at least 40 cm between the nozzle and the block [13]. After the sandblasting procedure, the blocks were cleaned using acetone to remove impurities and greases.

All specimens were assembled with the acrylic PSA in a mould with 23 kPa applied to each joint and then rested for 72 hours before being tested. Figure 3.3 illustrates the mould setup for mode I test specimens. A similar setup was used for mode III mould, the only difference being that the steel blocks were not present this time. As will be described further, a 3D-printed part was used to load the specimens for these tests.

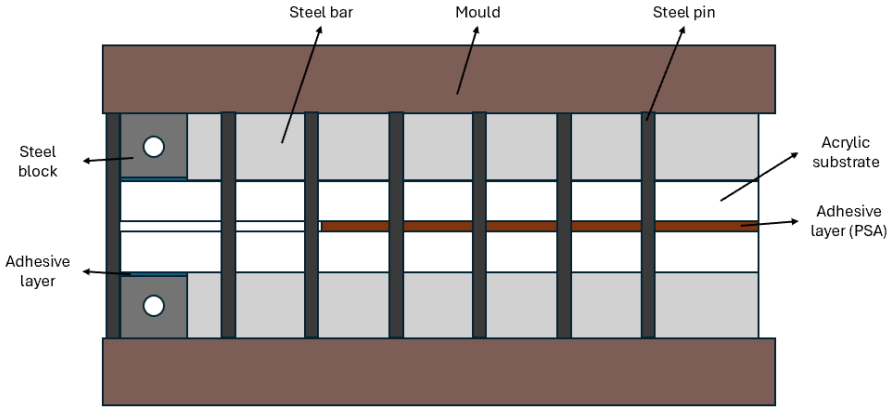


Figure 3.3: Representation of the mould used.

Vacuum condition manufacturing

PSAs, as detailed in Section 2.3, are designed to be permanently tacky and adhere with minimal pressure, such as that applied by a finger or hand. PSAs should be progressively applied along the desired bonding length while maintaining pressure on the recently bonded areas to guarantee the absence of defects.

Applying the PSA to the first substrate is relatively straightforward due to the adhesive's flexibility. This flexibility allows for the gradual application of the adhesive, ensuring uniform adhesion and minimising the risk of air entrapment or incomplete bonding. The application process becomes challenging when dealing with the second substrate. The rigidity of the second substrate prevents the gradual application of the PSA, making it difficult to achieve a good level of adhesion without defects.

A vacuum environment was created to produce samples with the fewest possible defects. To achieve this, a vacuum pump connected to a plastic bag sealed with sealing tape was used. A mould was placed inside the bag, which was 3D printed (Figure 3.4), to ensure the alignment of the substrates. The mould was printed using Polyethylene terephthalate glycol (PETG), a commonly used filament for 3D printing, whose characteristics are shown in Table 3.3. PETG was selected due to its minimal thermal expansion, which minimises warping and enables printing without the need for an enclosure, and its ability to sustain the compression forces created by the vacuum.

This piece was created using an original Prusa i3 MK3S+ 3D printer (Prusa Research, Prague, Czech Republic).



Figure 3.4: Vacuum setup.

Table 3.3: Properties of the PETG filament [76, 77].

Property	Value
Filament diameter [mm]	1.75
Density of the filament [g/cm^3]	1.27
Nozzle recommended temperature [°C]	240
Bed temperature [°C]	90
Maximum service temperature [°C]	80

The configuration consists of a mould in which one of the substrates is placed with the adhesive already applied. The second substrate is placed on top, separated by two pins that are placed at the ends of the bottom substrate. Since one end is already bonded with adhesive, about 5 mm of the adhesive-length extremity had to be cut off using a scalpel. This procedure does not affect the experimental results since, as described in section 2.2.2, one of the premises for applying the J integral is that the end of the adhesive must remain stress-free throughout the test. This point will be confirmed later when analysing the results. This entire assembly is placed inside a plastic bag. The vacuum pump is then activated, and the air is gradually removed from the interior of the vacuum bag. A throttle was used to control the air outlet speed. Once the air pressure reaches the desired levels, the pins are removed from outside the vacuum bag. Figure 3.5 shows the adhesive placed on the open mould with the pins already in place.

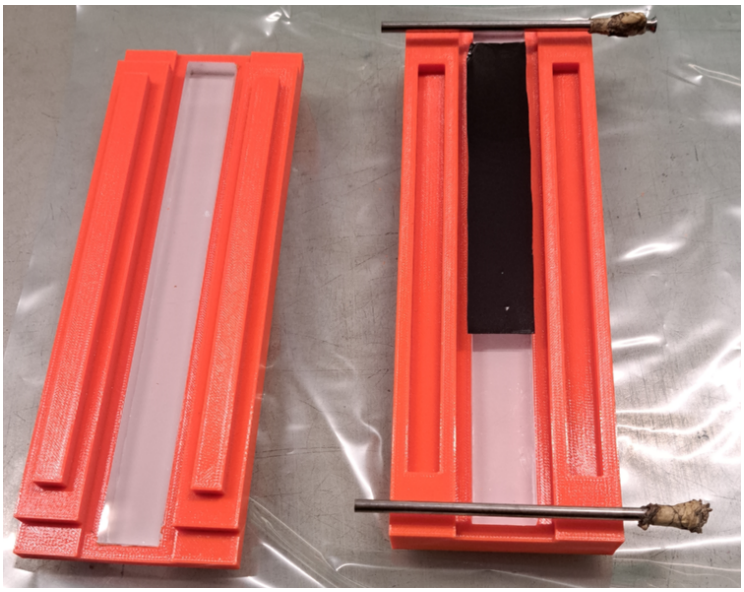


Figure 3.5: Open vacuum mould.

Once the pins are removed, due to the action of gravity and the compression forces caused by the pressure difference, the second substrate is pressed onto the first, completing the DCB specimen. This method ensures proper alignment and minimises defects by utilising the vacuum environment to apply uniform pressure during bonding.

This procedure was only carried out for adhesive A. Adhesive B is thicker and foamier, so the pressure exerted by the mould and the weights on the DCBs produced with this adhesive is sufficient to remove the air bubbles and guarantee good adhesion.

Due to the limitations of the setup, it was not possible to achieve a perfect zero-pressure environment. As the air was removed, the plastic bag became increasingly adhered to the tube through which the air was extracted, eventually obstructing it completely before a vacuum environment was achieved. Nevertheless, as can be seen in Figure 3.6, the sample produced in this environment (bottom) presented considerably fewer defects in comparison with the ones produced at ambient pressure (top). From now on, samples produced in this low-pressure environment will be referred to as vacuum samples for the sake of simplicity, even though these condition has not been fully achieved.

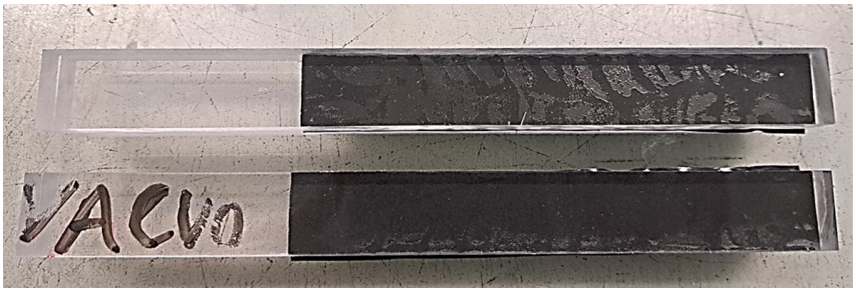


Figure 3.6: Adhesive A DCBs produced with (bottom) and without (top) a vacuum environment.

3.2.2 Peel specimens

The peel specimens were composed of three materials: the adhesive (PSA), the PMMA substrate and a backing calibrated tape from Helios-Preisser (Gammertingen, Germany) made of steel 1.4310 (whose mechanical properties are described in table 3.4).

Table 3.4: Mechanical properties of steel 1.4310.

Density	Young's modulus	Poisson's ratio
7900 kg/m^3	160 GPa	0.28

The adhesive samples were cut with a scalpel, 100 mm long and 10 mm wide sheets. A bond length of 50 mm was used between the adhesive and the PMMA substrate. Before bonding the PSA to the acrylic, the backing calibrated steel tape with 0.01 mm of thickness and 12.7 mm of width was applied.

Figure 3.7 presents the peel specimen. The grey line presents the steel backing (the thickness is not represented in scale).

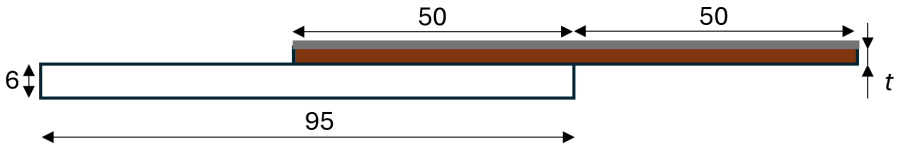


Figure 3.7: Peel specimen configuration, in mm.

Lastly, all the specimens were assembled in a mould, with each joint being subjected to a pressure of 23 kPa for 72 hours before testing.

3.3 Testing setup

All the tests were performed using a quasi-static machine, INSTRON ® 3367 (Illinois ToolWorks, Hopkinton, Massachusetts, USA), equipped with a 1kN load cell. A rate of 5 points per second was used for data collection. At least three specimens were tested for each testing condition.

The images recorded during tests were obtained using a digital camera (Nikon D5300). This camera was equipped with a Nikon AF-P NIKKOR 18-55mm f/3 lens and was positioned in front of the specimens, with the lens perpendicular to the observation surface. As studied and described on [17], to obtain high-quality results, it is crucial to ensure adequate speckle and lighting conditions. A spotlight was used for this purpose and to ensure a consistent test set-up.

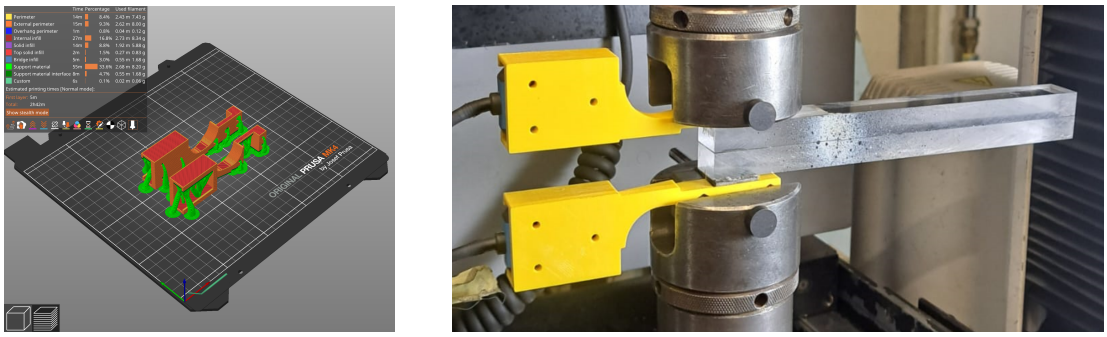
A laser-based method was selected to ensure perpendicularity. A 3D-printed component was used to position the laser perpendicular to the test specimen. An L-shaped part was placed against the surface of the camera lens to ensure that the beam of light coming from the laser was parallel to the edges of this part. This ensures that the plane to be photographed is perpendicular to the axis normal to the camera surface.

In the following sub-chapters, the test configuration used in each case will be described in detail.

3.3.1 DCB mode I testing

As described in section 2.3.4, knowing the values of the rotations of the DCB's substrates is crucial for obtaining the cohesive law through direct method. SICK® (Waldkirch, Germany) TMS22E inclinometers were used for this purpose. To connect the inclinometers to the blocks, 3D-printed parts were utilised. These parts were printed using PETG material, with properties that are the same as the ones previously described in Table 3.3.

The inclinometers were connected to a data acquisition system that registered the voltage variations measured at a rate of 5 points per second (coincident with the data retrieved from the tensile testing machine). The voltage values obtained were subsequently converted into rotations using a constant relation previously obtained through calibrations.



(a) (b)

Figure 3.8: Manufacturing of the inclinometers supports. (a) Slicing of the inclinometers supports using PrusaSlicer software. (b) Assembly of the inclinometers supports to the DCB.

The DCB specimens were mounted on the universal testing apparatus using stiff steel pins to attach the end blocks with the inclinometer supports to the machine. A preload was applied to all tests to avoid noise at the start of the tests and ensure stable crack propagation.

Figure 3.8a shows the slicing of the supports for the inclinometers using PrusaSlicer software, and Figure 3.8b presents the assembled printed pieces on the blocks of the DCB specimens. Figure 3.9 presents the final setup used for the mode I test.

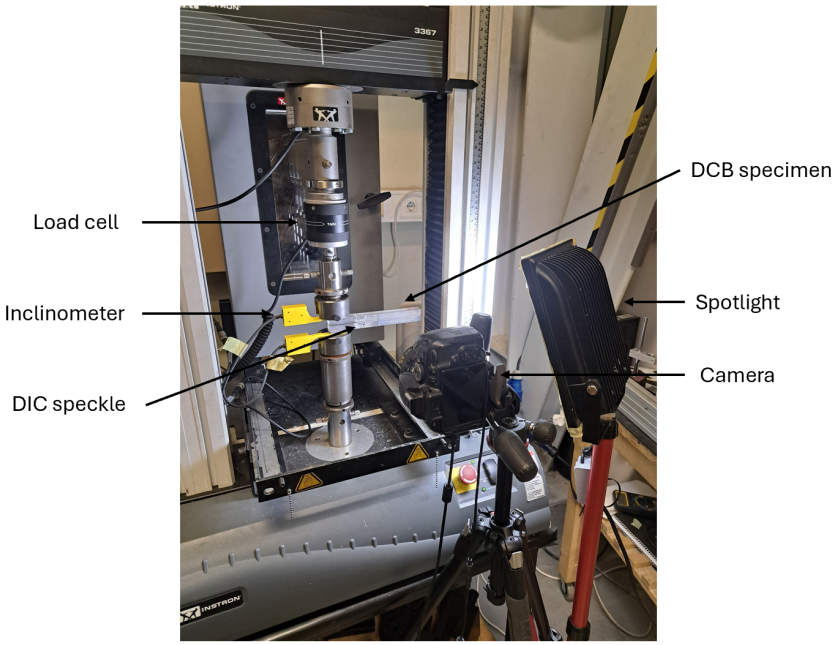


Figure 3.9: DCB mode I testing setup.

3.3.2 DCB mode III testing

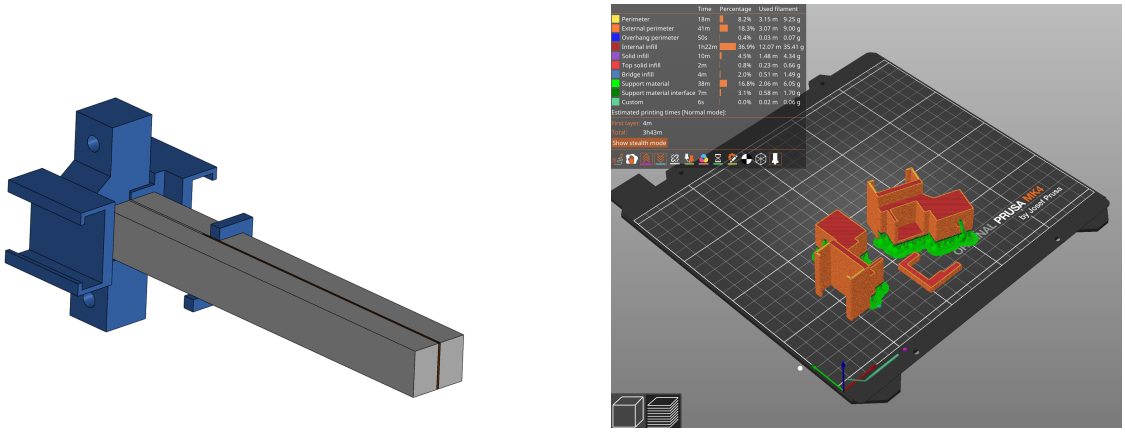
For the DCB mode III tests, a setup similar to the one previously described was used. Due to space limitations in the grip areas, instead of using steel blocks to load the specimens, a 3D-printed part was developed for this purpose. In order to ensure that this component could withstand the loading conditions to which the DCB would be subjected, a Prusament polycarbonate (PC) Blend was used (whose properties are available in Table 3.5) with an 80% percentage of infill. This polymer exhibits particularly good tenacity and tensile strength.

Table 3.5: Properties of the PC filament [78].

Property	Value
Filament diameter [mm]	1.75
Density of the filament [g/cm^3]	1.22
Nozzle recommended temperature [°C]	275
Bed temperature [°C]	110
Maximum service temperature [°C]	113

This piece is attached to the substrate through compression, has a cavity on the side that will support the inclinometers and has a pass-through hole so that it can be loaded using a stiff steel pin connected to the tensile machine, thus ensuring, once again, free rotation of the substrate. In this test, DIC was used in a similar setup to the one used in the mode I test to measure the CTOD.

Nevertheless, in this case, since we are loading the samples on shear, it is impossible to track the speckle in the adherent that stays in the backplane since the adhesive will cover it from the camera's point of view. To get around this problem, a small part was designed and 3D printed. This is attached to the adherent by means of compression and consists of an extension of the adherent so that its displacements can be measured in a plane coinciding with the front face of the other adherent. Figure 3.10a illustrates the CAD model of the supports for the inclinometers and for the DIC assembled on the DCB specimen, and Figure 3.10b presents the slicing of the 3D-printed pieces on PrusaSlicer software.



(a) (b)

Figure 3.10: 3D-printed supports for the inclinometers and DIC: (a) CAD model; (b) Slicing of the supports in the PrusaSlicer software.

The final result of the DCB specimen with the 3D-printed pieces mounted on the testing machine can be seen in Figure 3.11.

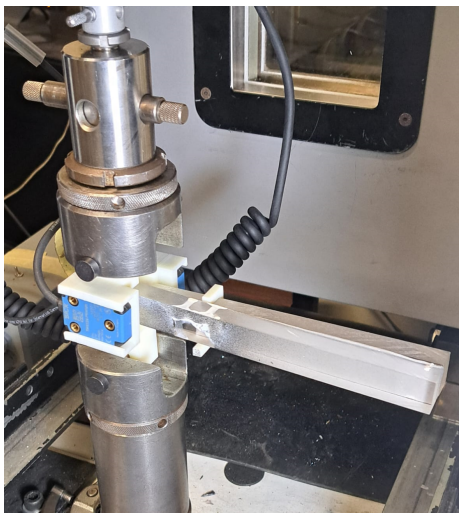


Figure 3.11: DCB specimen with the 3D-printed pieces under mode III loading conditions.

3.3.3 Peel testing

In the scope of this thesis, an apparatus for the tensile testing of peel specimens at different angles was developed.

The idealised device, illustrated in Figure 3.12, consists of two parallel polished steel shafts (2) supported on two fixed aluminium blocks (1), on which a base (4) slides using bearings (3). This base has a slot into which a table can be fitted (5). In this way, tables with different angles can be mounted, making it possible to vary the peel angle at which the tests are carried out. Furthermore, to ensure the alignment of the test over time, a cable (7) and pulley (6) system was used to ensure that the base followed the peeling of the tape. A pre-stretched 1.5 mm diameter stainless steel cable was used for this purpose. Therefore, given that the rigidity of steel is greater than that of PSAs, any elastic deformations in the rope can be considered negligible. This cable is fixed to the moving table, passes through the pulley and is fixed again to a long, rigid pin (8) that is fixed to the top of the load cell (9) of the uniaxial testing machine. In this way, we ensure that when we have a vertical displacement of the grip that pulls the tape, we will have a displacement with the same magnitude in the table. Since the pin that pulls the rope is fixed at a higher level than the load cell, the forces exerted to move the table will not be measured by the load cell.

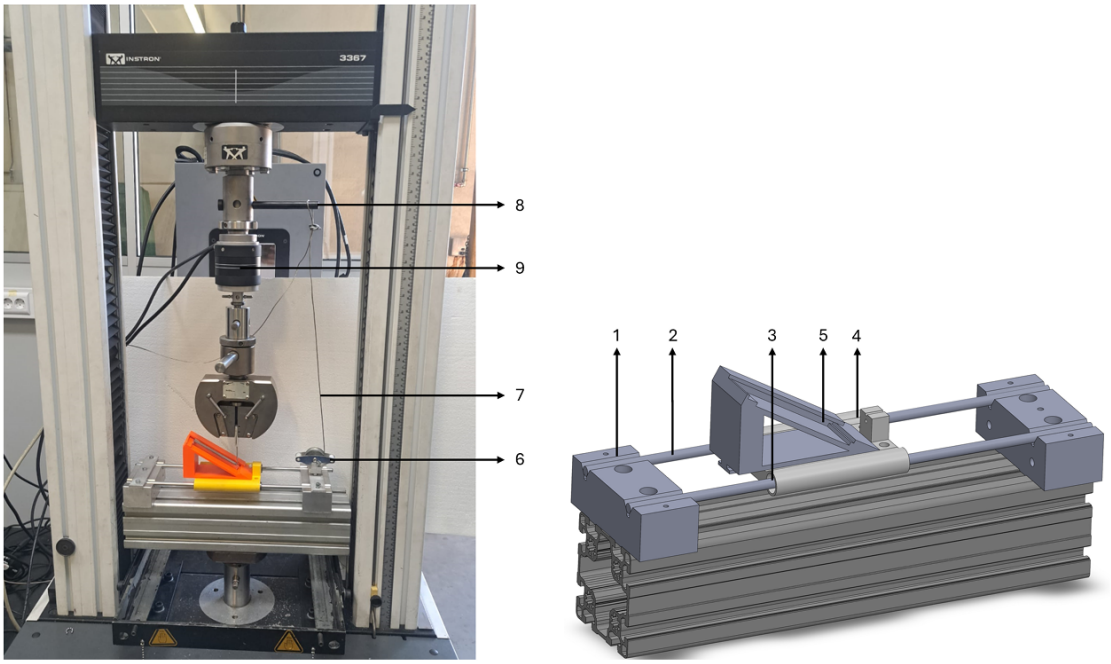


Figure 3.12: Test setup attached to the testing machine (left). CAD model of the test setup (right).

The moving base and the tables were printed using PETG (properties on Table 3.3). The slot where the tables connect with the base was always printed in a direction normal to the printing table in order to ensure their alignment. Additionally, organic supports were incorporated using PrusaSlicer software to improve the quality of the pieces (Figure 3.13). Only the 90, 120 and 150

degrees tables are illustrated for simplicity. A similar setup was used for the moving base and for the 30, 60 and 180 degrees tables.

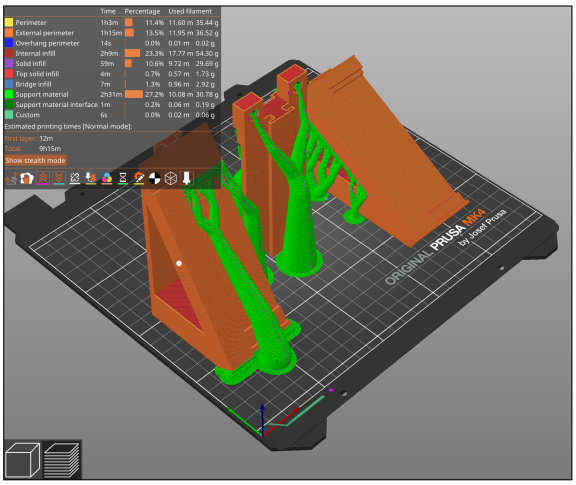


Figure 3.13: Slicing of the different angle tables for the peel tests in the PrusaSlicer software.

As described in section 3.3, a camera was used to follow the opening displacements at the crack tip. In this configuration, as we only have a substrate at the bottom of the sample, it is not possible to use the DIC method. The images were, therefore, digitally processed using a Python code to measure the value of this opening at certain times. A white background was used for easier processing.

3.4 Experimental results

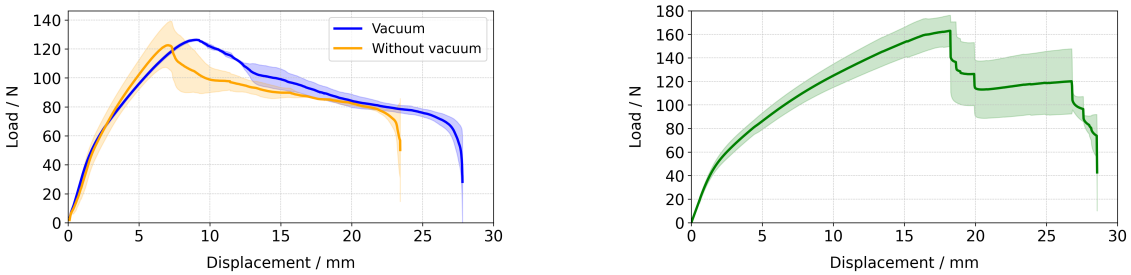
This section describes the experimental results obtained for the mode I and mode III DCB tests and the peel tests.

In this chapter, to avoid repetition, only the general steps are detailed since a detailed analysis and discussion are presented in the attached papers in **Appendixes** A and B.

All outputs from experimental tests presented in this work are illustrated with a solid line presenting the average of all the tests performed for a given condition, surrounded by a shadow area representing the respective standard deviation. At least 3 tests were performed for each condition.

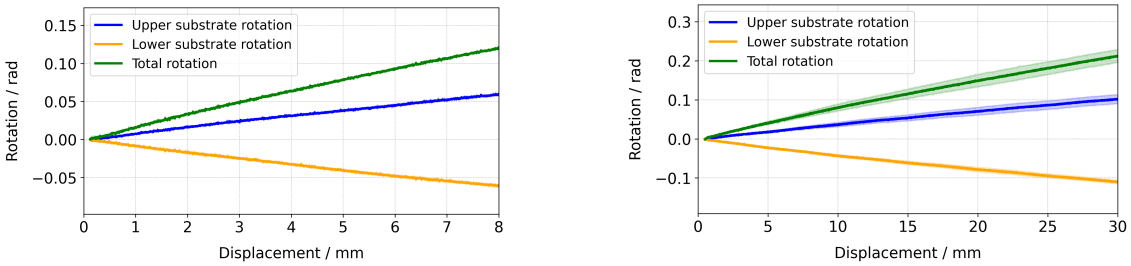
3.4.1 DCB mode I testing

The J-integral approach was used to characterise the fracture behaviour of the adhesives. As previously explained, the loads were measured using a quasi-static machine and the rotations with inclinometers, allowing the computation of the J-integral according to Equation 2.10. The outputs are shown in Figures 3.14, 3.15 and 3.16, respectively, for DCBs tested with adhesives A (produced with and without a vacuum environment) and B.



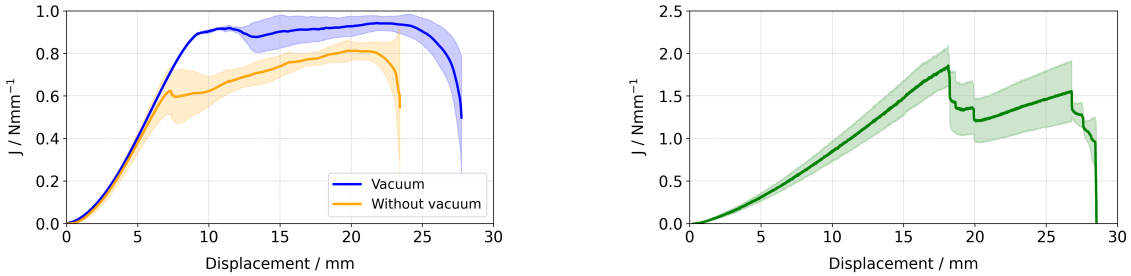
(a) (b)

Figure 3.14: Load-displacement curves for DCB mode I testing with adhesives: (a) A and (b) B.



(a) (b)

Figure 3.15: Rotations of the acrylics for DCB mode I testing with adhesives: (a) A using a vacuum condition manufacturing and (b) B.

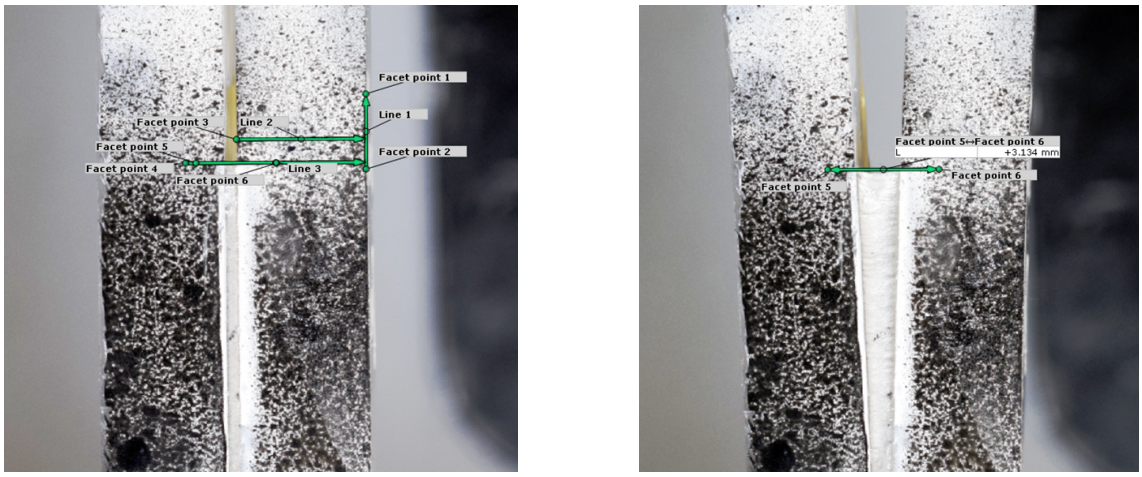


(a) (b)

Figure 3.16: Fracture energy curves based on the J-integral approach for DCB mode I testing with adhesives: (a) A and (b) B.

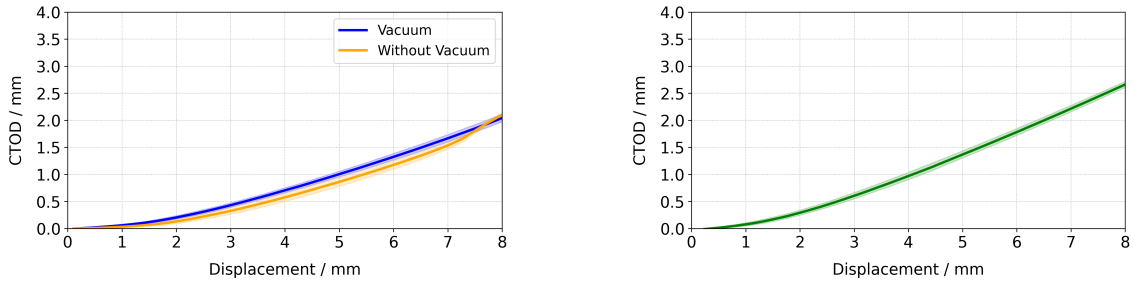
Using the GOM Correlate software, the CTOD was determined by tracking the displacements in the speckle painted on the substrate's lateral surfaces. Figure 3.17a illustrates the procedure used in the software to ensure perpendicularity between the direction of the opening of the crack and the substrate edges. Two points coincident with the substrate edge were initially marked in order to trace a line on over it (line 1). Next, point number 3 was marked on top of the opposite edge of the same substrate, and a straight line was drawn perpendicular to line 1, defined by the limits of line 1 and point 3. A length of 12 mm was assigned to this line (the value of the substrate thickness), and it was used as a reference to determine the scale factor between pixels and mm.

Then, a line perpendicular to line 1 and passing through the crack tip was traced. Finally, two points over this line were selected (5 and 6), the remaining geometric features were deleted, and the relative distance between these two points was measured over time (Figure 3.17b). Figure 3.18 presents the results obtained.



(a) (b)

Figure 3.17: GOM correlate software: (a) procedure to ensure perpendicularity and (b) measuring of the CTOD for DCB mode I testing.



(a) (b)

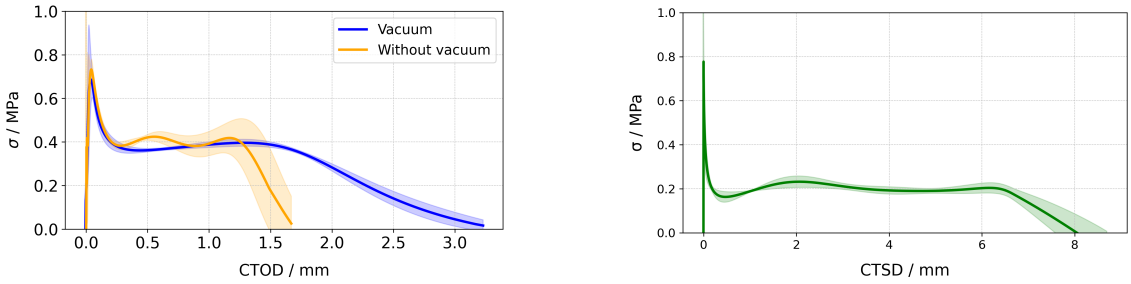
Figure 3.18: CTOD measured using DIC for DCB mode I testing with adhesives: (a) A and (b) B.

The cohesive law was estimated using the values for J-integral and the CTOD acquired by the previously mentioned methods. All the parameters were adjusted using the Savitzky-Golay Filter because noise was inevitable in the raw data. The results were smoothed by adjusting the polynomial order and window length. After that, the cohesive law was determined by direct differentiation:

$$\sigma = \frac{J_{I_{t+\Delta t}} - J_{I_t}}{\mathrm{CTOD}_{t+\Delta t} - \mathrm{CTOD}_t} \tag{3.1}$$

where t is time and δt is the increment between two measurements.

The obtained cohesive laws for both adhesives are present in Figure 3.19.



(a) (b)

Figure 3.19: Average cohesive law for DCB mode I testing with adhesives: (a) A and (b) B.

3.4.2 DCB mode III testing

In order to feed the numerical models with shear test data, DCB tests in mode III load configuration were performed. Due to the high displacements of PSAs, mode II tests, like End-Notched Flexure (ENF), were not an option since the substrates could not sustain the loads until a stable crack propagation had been reached. Therefore, in this thesis, in order to gather shear data, the specimens were loaded in an out-of-plane shear and then it is assumed that $G_{II_c} = G_{III_c}$.

Figure 3.20 depicts the fundamental deformation modes in a two-dimensional context. In three-dimensional scenarios, two orthogonal shear components are additionally considered. Thus, the normal component of the traction vector is denoted as σ, and the in-plane components are τ_1 and τ_2, with the corresponding deformation measures being w, v_1, and v_2, respectively. Fracture mechanics terminology is used when only one of the deformation modes is involved. To be more precise, Mode I loading is defined as σ and w being the most prevalent factors, while Modes II and III are defined as τ and v components being predominant [79].

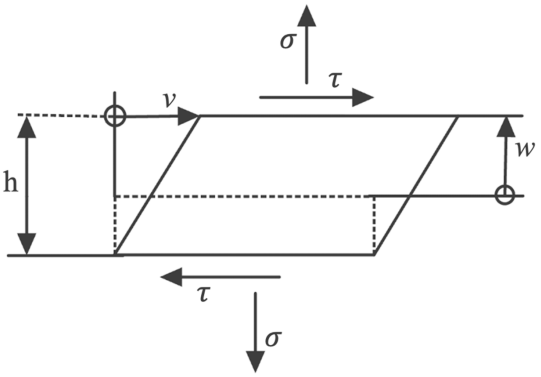


Figure 3.20: The tape with thickness h exhibits two modes of deformation: peel (w) and shear (v). Conjugated stress components σ and τ. Adapted from [79].

According to Stigh et al., [79], we can apply the same principles to derive mode III cohesive law that we apply in mode I (Section 2.3.4), only need to replace σ with τ and w with v.

In this way, a similar procedure to the one described in the previous subsection was used to obtain the cohesive law for adhesives A and B. Since the results obtained for Adhesive A tested

in mode III loading conditions are presented and discussed in the paper in **Appendix** A, only the results for adhesive B are analysed in detail in this section.

Figures 3.21 and 3.22 present images of three different timestamps recorded during testing for adhesives A and B, respectively. While adhesive A shows a similar behaviour to the one observed on mode I tests with a big deformation of the adhesive layer, on the other hand, adhesive B appeared to have a completely different behaviour in comparison to when loaded in an opening mode. Adhesive B, as can be seen in the image on the right (Figure 3.22), had the formation of long fibrils, and the failure of the adhesive was characterised by their gradual failure.

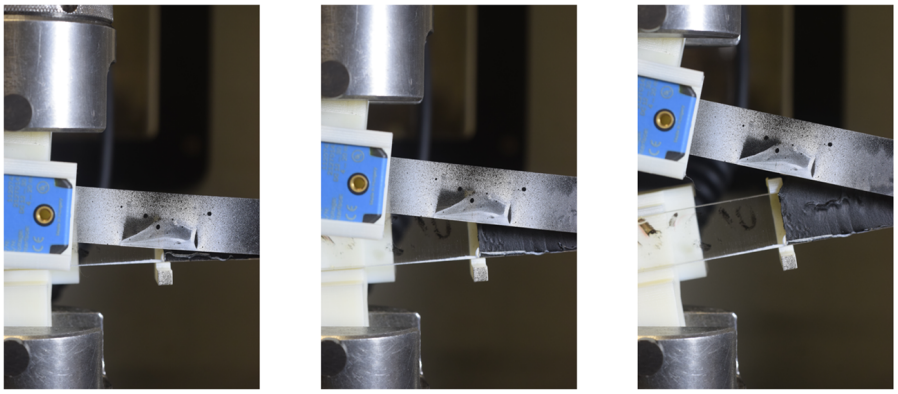


Figure 3.21: Three different timestamps for DCB being loaded in mode III with Adhesive A.

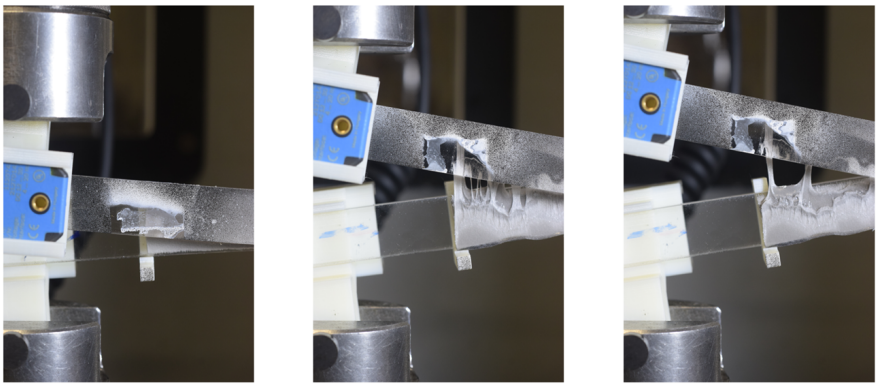
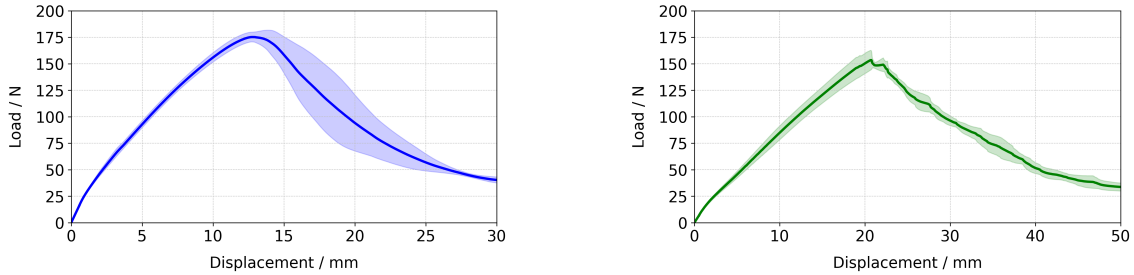


Figure 3.22: Three different timestamps for DCB being loaded in mode III with Adhesive B.

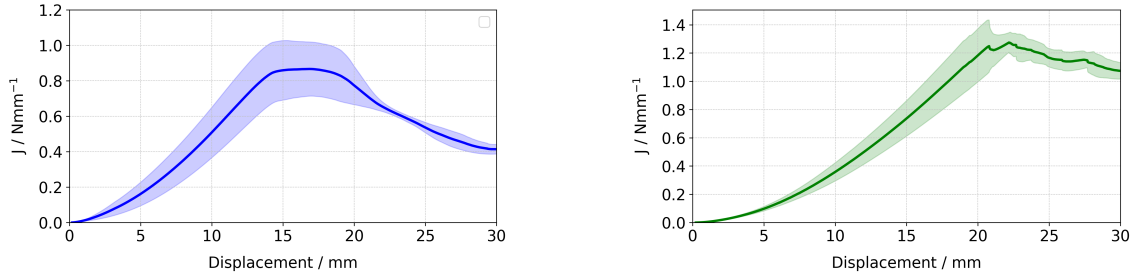
The results obtained for the load-displacement curves and fracture energy are presented in Figures 3.23 and 3.24, respectively, for both adhesives.

Adhesive B reached a peak load of 157.3 $\pm$ 7.0 N, which translates into a fracture energy of 1.33 $\pm$ 0.13 N/mm. In this adhesive, we have a clear reduction in the energy values when loaded in shear compared to tensile loading. These results are in accordance with the behaviour observed in the images and explained previously. In mode I, we have a large accumulation of deformation, leading to a bigger fracture process zone and, consequently, higher values of energy.



(a) (b)

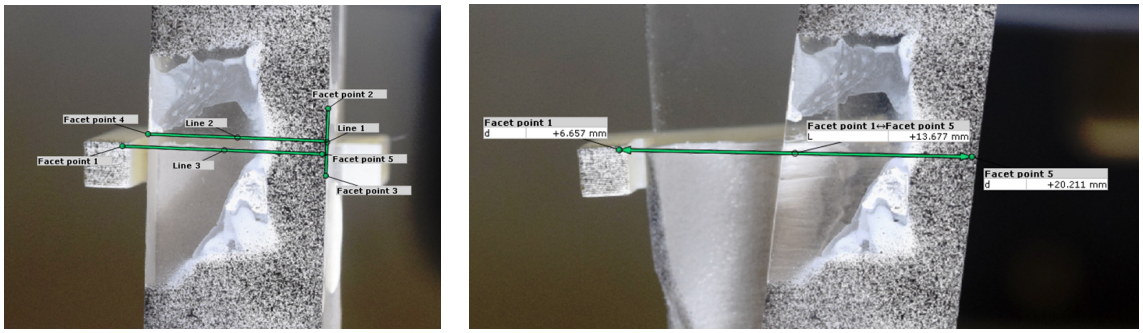
Figure 3.23: Load-displacement curves for DCB mode III testing with adhesives: (a) A and (b) B.



(a) (b)

Figure 3.24: Fracture energy curves based on the J-integral approach for DCB mode III testing with adhesives: (a) A and (b) B.

As illustrated in Figure 3.25, a similar procedure to the one described in the previous section was used to determine the crack tip shear displacements (CTSD) in DCB mode III testing. The main difference is that this time, the points were measured at a greater distance since the speckle was painted on the 3D-printed support.



(a) (b)

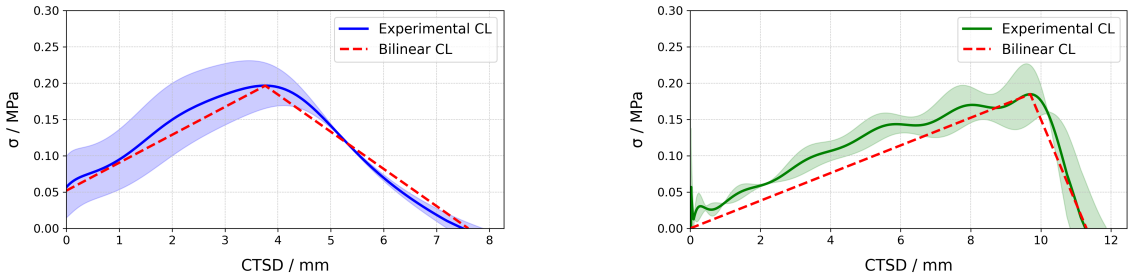
Figure 3.25: GOM correlate software: (a) procedure to ensure perpendicularity and (b) measuring of the CTSD for DCB mode III testing.

The cohesive law was estimated using the values obtained from the previously mentioned methods for J and the CTSD. Due to the presence of noise in the raw data, the Savitzky-Golay Filter was used to smooth their effect.

Based on Equation 3.1 and adjusting the loading and deformations modes according to Figure 3.20, the cohesive laws were obtained by direct differentiation:

$$\sigma = \frac{J_{III_{t+\Delta t}} - J_{III_t}}{\mathrm{CTSD}_{t+\Delta t} - \mathrm{CTSD}_t} \tag{3.2}$$

The obtained cohesive laws for both adhesives when loaded in mode III conditions are present in Figure 3.26. Due to the presence of noise in the extraction of these laws, they were approximated to bilinear cohesive laws (dashed lines), as will be explained further in the numerical details.



(a) (b)

Figure 3.26: Average cohesive law for DCB mode III testing with adhesives: (a) A and (b) B.

3.4.3 Peel testing

The experimental results obtained for the peel tests are provided in Figures 3.27 and 3.28 for adhesives A and B, respectively.

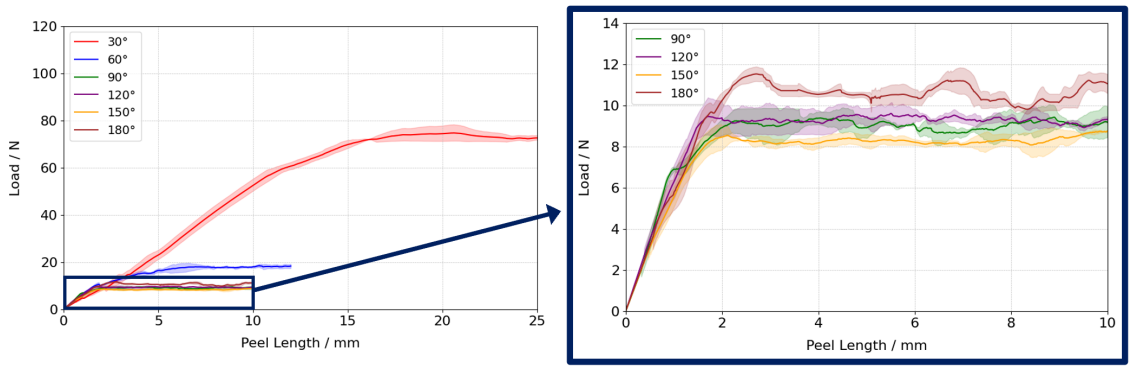


Figure 3.27: Peel curves for adhesive A.

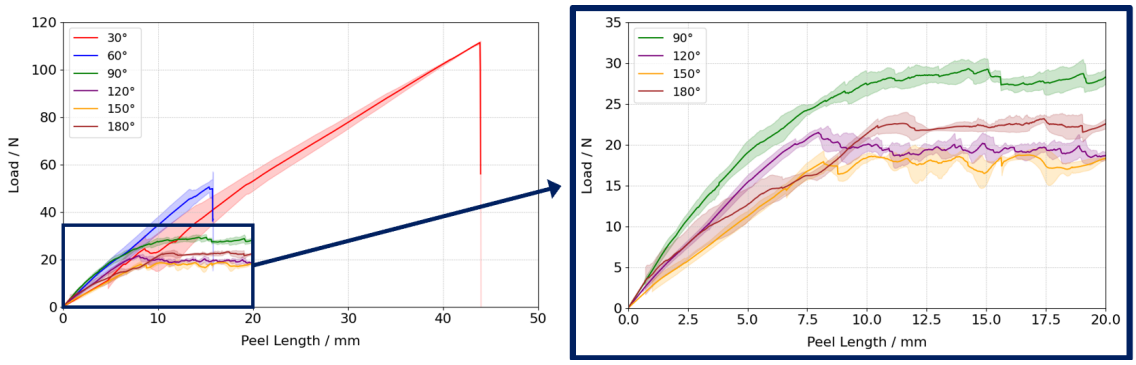


Figure 3.28: Peel curves for adhesive B.

In the paper available in **Appendix** B, a study regarding the adhesion energy was developed according to the theory described in section 2.3.5. The effects of the energy dissipated in the steel backing due to plastic bending were studied, and based on the algorithm provided by Kinloch et al. in [56], a Python code was developed to compute these values. This code is provided in **Appendix** C.

Additionally, an extensive characterisation of the FPZ was performed. This analysis consists of digitally processing the images recorded during the experimental tests using a Python script.

First, the code loads the FPZ image from the user's defined path. Then, functions from the Python library are called to enable dynamic features like mouse clicks and zoom actions for a more precise point selection. Then, the code asks the user to select 2 points defining the acrylic thickness. Since this value is constant and equal to 6 mm, a scale factor is determined based on the measured pixel distance. After that, the user needs to define four additional points: two for the FPZ height and two for the FPZ length. With the previously defined scaling factor, the real distances are computed in mm. This code is provided in **Appendix** D

Chapter 4

Numerical details

This chapter describes the numerical modelling techniques used in this work. All simulations were performed using ABAQUS® (Dassault Systèmes, Suresnes, France) software.

For the DCBs (loaded in mode I and mode III) and peel specimens, a CZM was used to predict the failure behaviour of these joints. Additionally, some studies were performed with hyperelastic models to later combine them with cohesive elements and, therefore, produce a robust model capable of predicting the mechanical behaviour and failure modes of joints in real applications.

4.1 Cohesive zone modeling

4.1.1 DCB mode I testing

A 2D model with an out-of-plane thickness of 19 mm was used to model the DCB tests loaded in mode I. The adhesive layer was modelled using 260 linear quadrilateral cohesive elements (COH2D4) with one element per thickness, while 39422 plain strain elements with reduced integration (CPE4R) were used to model the adherends and the steel blocks.

Using the obtained cohesive laws (Figure 3.19), the damage curves (Figure 4.1) were calculated using Equation 4.1 and implemented in the FE software.

$$Damage = 1 - \frac{\sigma}{K \cdot \delta} \tag{4.1}$$

, where K is the slope of the cohesive law before the maximum stress point and δ is the increase in the CTOD after the initiation of damage propagation.

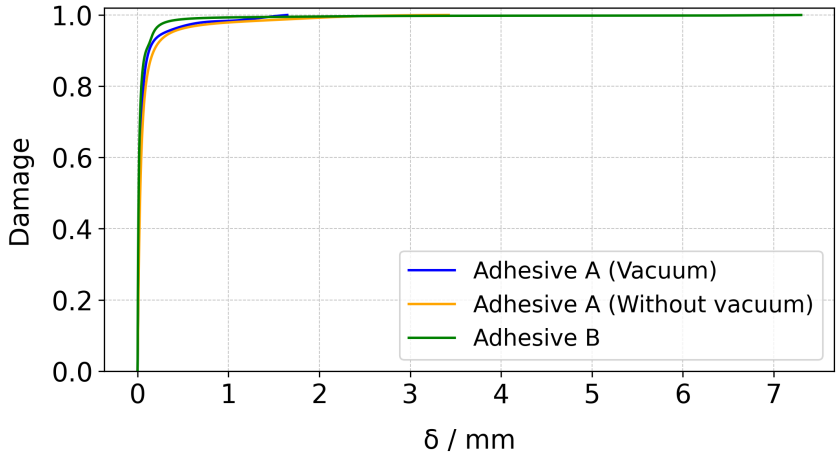


Figure 4.1: Average damage curves.

The final mesh, as well as the boundary conditions applied to the model, can be seen in Figure 4.2 and the results and discussion are presented in the annexed paper (**Appendix** A).

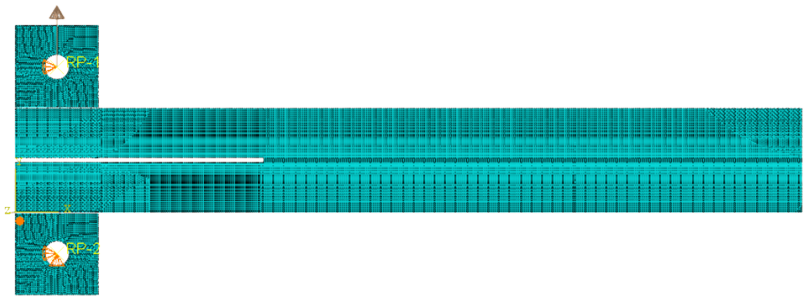


Figure 4.2: Mesh and boundary conditions used in the DCB mode I testing FE model.

4.1.2 DCB mode III testing

Reducing this model to a 2D problem was not possible because the mode III loading of a DCB specimen involves an out-of-plane shear mode. Consequently, in order to avoid simulations that have unreasonably high computational costs and still guarantee accurate results, it is imperative to use a mesh with optimal dimensions. A biased local seed was applied in conjunction with a convergence study to produce a finer mesh at the interface between the adhesive layer and the acrylic. C3D8R elements were used to model the acrylic substrates and the PC supports, while COH3D8 elements were used to model the adhesive. Figure 4.3 displays the final mesh obtained.

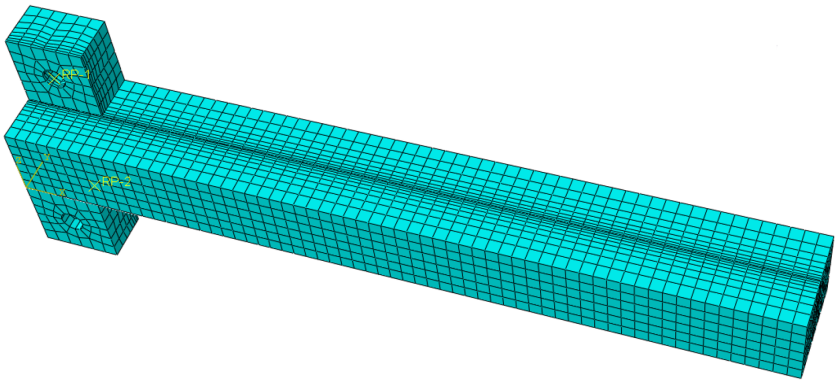


Figure 4.3: Mesh used in the FE model.

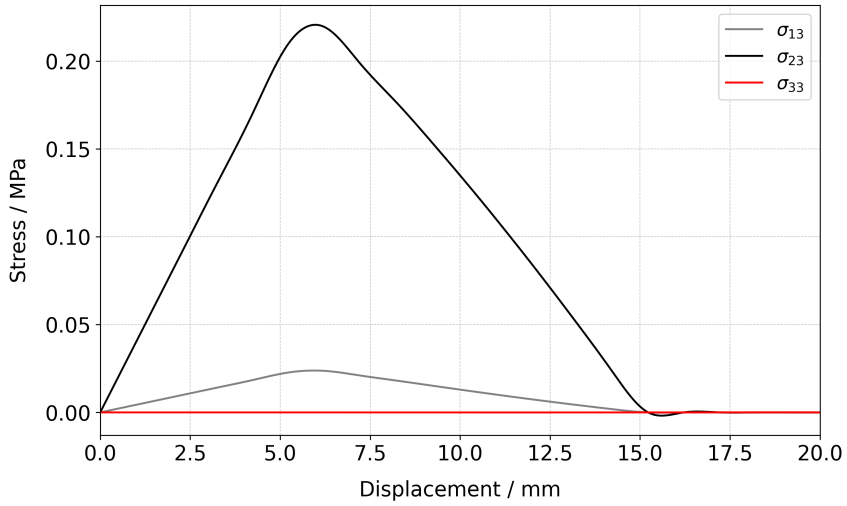
The boundary conditions were applied using a coupling interaction between the cylindrical surfaces inside the PC blocks and a reference point created at their centroid. As shown in Figure 4.4, in the lower block, the movements were constrained in x and y direction, while in the upper block, a velocity of 2 mm/min was enforced in z direction.



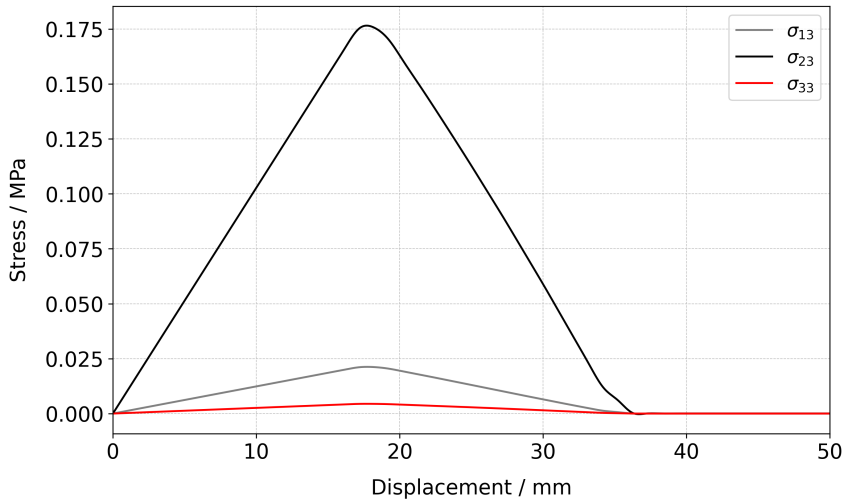
Figure 4.4: Boundary conditions applied in the FE model.

Adhesives A and B were simulated using a CZM, where the cohesive law was extracted from the experimental results (Figures 3.26a and 3.26b, respectively). Considering that both cohesive laws have a triangular shape, to avoid inducing noise in the material models, instead of inputting these in a tabular way (as was done in DCB mode I testing), these laws were adapted to bilinear laws. The damage initiation was defined by an elastic traction stiffness and the maximum stress, while the damage evolution was modelled using the values obtained for the fracture energy.

A stress analysis in the first element in the adhesive layer was done to confirm that the adhesives were being loaded in an out-of-plane shear. A local reference system was used for each cohesive element, where direction 3 is defined as a through-thickness direction, corresponding to the y direction in the undeformed shape, while directions 1 and 2 are aligned with x and z axis, respectively (Figure 4.4). The results obtained were plotted in function of the displacement at the loading point and are presented in Figure 4.5.



(a)

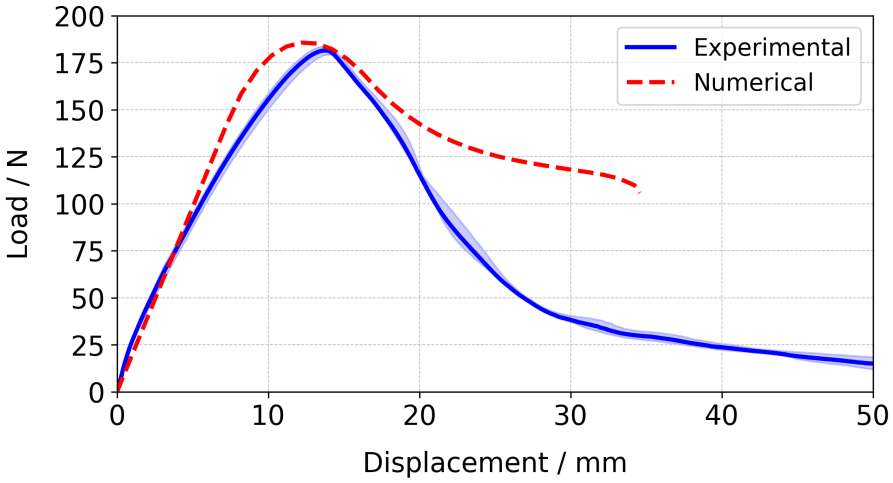


(b)

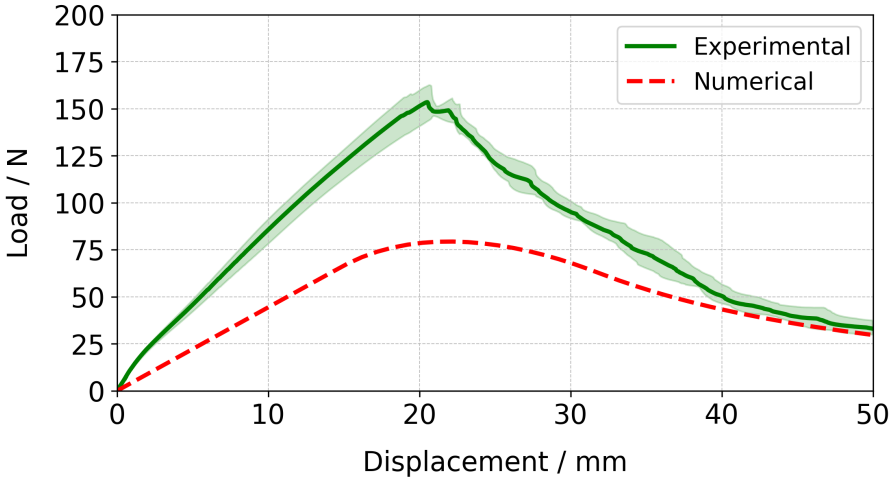
Figure 4.5: Stresses contribution of different loading modes on a cohesive element for adhesives (a) A and (b) B.

Both adhesives presented a similar stress distribution. It is clear that the tensile forces acting through-thickness have no representation in the system. Moreover, the out-of-plane shear forces (σ_{23}), as expected, have a major contribution to the adhesive behaviour, presenting much higher values when compared to the in-plane-shear forces σ_{13}. Nevertheless, despite the larger contribution of σ_{23} to the total stresses in the adhesive, these numerical results need to be carefully analysed since the model is unable to predict if exist tensile forces acting on direction 2, therefore, it is not possible to confirm that the system is under pure mode III loading conditions.

The results obtained for the numerical load-displacement curves for both adhesives are presented in Figure 4.6 in comparison with the previously obtained experimental data.



(a)



(b)

Figure 4.6: Comparison between experimental and numerical load-displacement curves for DCB mode III testing with adhesives: (a) A and (b) B.

Adhesive A presented overall good agreement between the numerical and experimental results, indicating that the cohesive law accurately predicts the damage behaviour of the adhesive under mode III loading conditions. A detailed discussion of this adhesive numerical results is presented in the paper available at **Appendix** A. On the other hand, the results for adhesive B were not as satisfactory. Although the numerical model is able to predict the shape of the curve, the maximum load of the numerical load is approximately half of the values obtained in the experimental results. These results may indicate that the maximum stress obtained in the cohesive law is somehow below the real values, which may be occurring due to excessive filtering of the test data. The process of obtaining the right cohesive law is not always straightforward and may be highly dependent on the parameters used in the data reduction procedure.

Additionally, the results may also be influenced by the values measured using the DIC. As reported in section 3.3.2, for the mode III tests, an additional support had to be used in order to

track the displacements in the substrate that stays in the backplane (Figure 3.10a). Simões, in [17], reported that despite the analysis performed in GOM correlate correspond to the measure of the relative displacement between two points, the initial position (in the opening direction) of the reference points chosen to be tracked on DIC can have an influence on the results. In sum, considering that the speckle is being measured at a considerable distance from the crack tip, and since adhesive B presents much higher deformations than adhesive A, the values measured using DIC might not correspond to the real values of the crack tip opening and, therefore, can explain the error obtained estimating the cohesive law.

4.1.3 Peel tests

A 2D FE simulation with a 10 mm out-of-plane thickness was used to simulate the peel test. Bilinear quadrilateral cohesive elements (COH2D4) were used to model the adhesive, while 4-node two-dimensional plane strain elements with reduced integration (CPE4R) were used to model the remaining components. A mesh seed size of 0.2 mm was employed overall, and one element per unit thickness was employed for cohesive elements. A biased local seed was employed along the thickness of the acrylic substrate. The mesh size and boundary conditions used for a 30-degree peel test are displayed in Figure 4.7. The adhesive was modelled using a CZM, where two different approaches were employed. First, the cohesive law directly obtained from DCB mode I tests was applied to model the adhesive in peel tests, in order to, validate this law in a different geometry. Then, cohesive laws directly extracted from the peel tests at different angles were obtained. The methodology used to extract the two previously mentioned approaches and the detailed results and discussion are available in the annexed papers (**Appendixes** A and B).

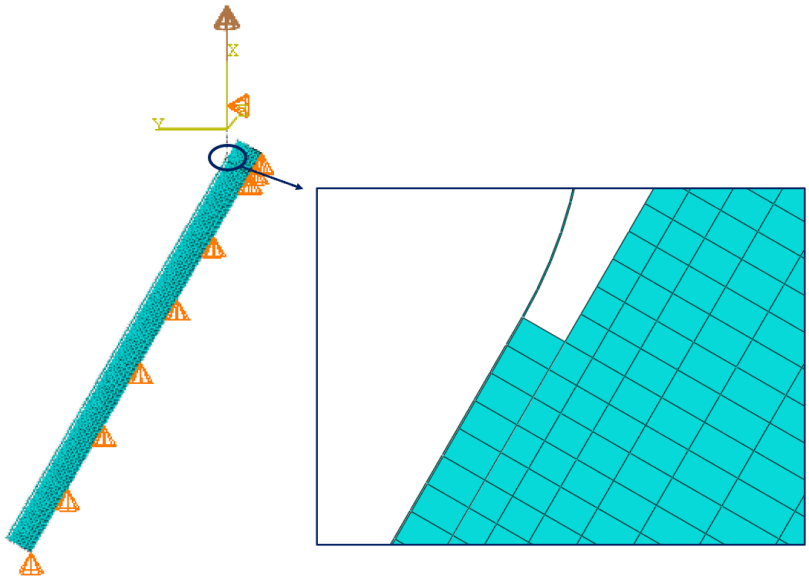


Figure 4.7: Schematic of the FE model.

4.2 Hyperelasticity

In this section, a numerical study with hyperelastic elements is developed to model single-lap joints (SLJ). The experimental data used was obtained from bulk specimens and SLJ, which were previously characterised and reported by Simões et al. in [80] and [81], respectively. Only adhesive B was studied since, in the data previously mentioned, only material information about this adhesive was available.

The substrates measure 107.5 mm in length and are 2 mm thick, with the adhesive layer having an overlap area of 10×10 mm^2. These dimensions correspond to those of the joints that were experimentally tested. For the boundary conditions, the joints were fixed on one end, and the other end was only able to move in the loading direction, so movement in the normal directions was constrained. To keep the same loading conditions used in the experimental tests, the joint was loaded at 1 mm/min, which was imposed at the free end of the joint. A more refined mesh was employed, using a biased local seed, in the zones near the interface between the adhesive and substrates since these are the zones where stress concentrations will occur. The final mesh is composed of CPE4H elements (linear plane strain quadrilateral elements with hybrid formulation) for both adhesive and substrates. The boundary conditions applied and the mesh used are shown in Figure 4.8.

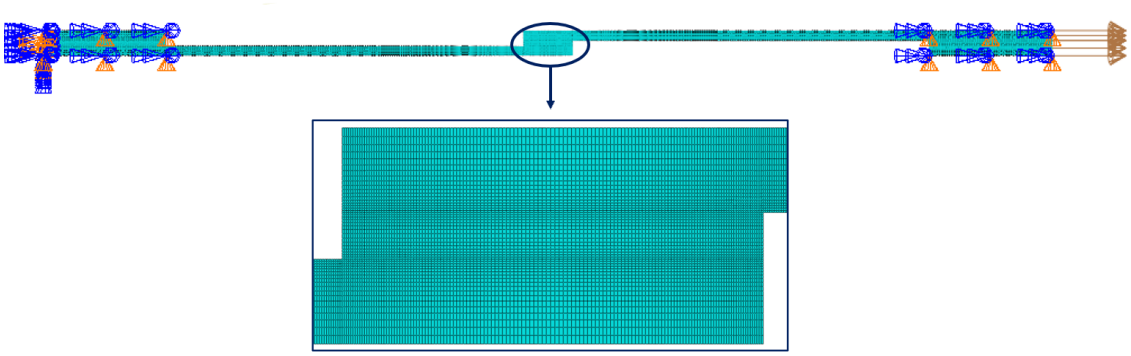


Figure 4.8: Mesh and boundary conditions applied in the FE model of SLJ.

The comparison between the numerical model's output using experimental data from bulk tests and experimental tests for quasi-static loading for SLJs are presented in Figure 4.9. Different models were employed between the ones exposed in section 2.3.6, but only the ones that present the best results are illustrated here. Despite none of the models being able to predict the behaviour of the adhesive, it is clear that the Mooney-Rivlin criteria is the one that presents the best similarity with the experimental results.

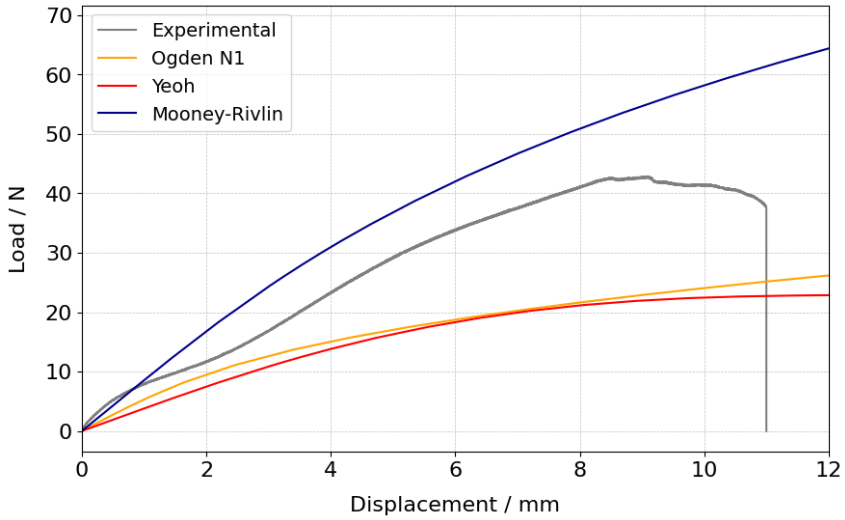


Figure 4.9: Experimental and numerical results for SLJ using bulk test data. Comparison between the different models.

Due to the inaccuracy of the results obtained, a different approach was employed. The uniaxial test data used in Abaqus to obtain the hyperelastic material constants was directly extracted from SLJ test data. The best model fits are displayed in Figure 4.10

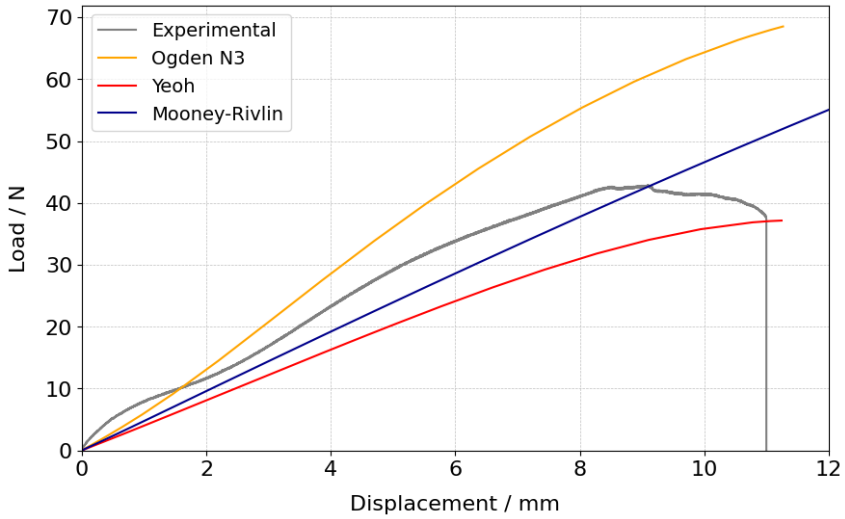


Figure 4.10: Experimental and numerical results for SLJ using SLJ test data. Comparison between the different models.

Notwithstanding the slight improvement in the results obtained, none of the models manages to reproduce the singularities present in the experimental curve. To obtain better results, it is clear that more test data, namely planar and/or biaxial test data, is necessary to provide the model with information regarding the behaviour of the adhesive when loaded in shear.

A study was developed to try to understand the ratio between the shear and the tensile forces acting on the adhesive layer. Therefore, numerical modelling of a block in shear with the same

dimensions (10 mm in length and 1.1 mm in thickness) as the adhesive layer in an SLJ was developed (represented in Figure 4.11).

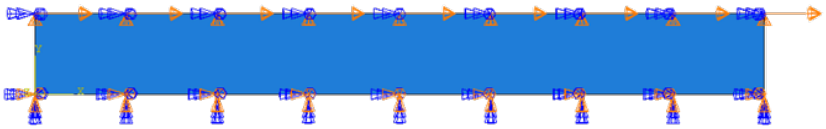


Figure 4.11: Boundary conditions applied to the block in shear.

The results obtained were then compared to the values obtained from an analytical model described in [82], where the stress components are expressed as a function of the shear strain in the loading direction, which is expressed as a function of the stretch ratios in and of itself and are derived using an Ogden strain energy function.

Figure 4.12 compares the results from the analytical and numerical approaches, where "A" stands for "Analytical" and "N" for "Numerical."

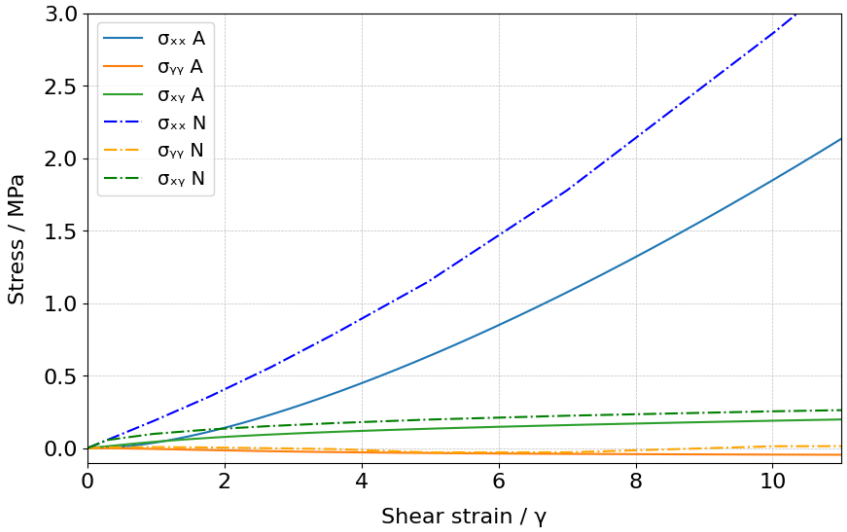


Figure 4.12: Experimental and numerical results for the stress tensor components in function of the shear stress.

These results show that for lower shear strain, the shear effects significantly impact the results obtained, and it is crucial to account for these effects for the correct modelling of SLJ. Additionally, despite that for large deformations, the tensile forces are predominant in the adhesive layer, the shear components still represent between 10% to 20% of the total stress. This reinforces the idea that, although, due to the high displacements characteristic of PSAs, tensile stresses are predominant under shear loading, the shear effects also need to be considered in hyperelastic models for an accurate prediction of the joint behaviour.

Chapter 5

Cyclic creep stations

It is crucial to carry out experiments and look into creep behaviour in materials in order to understand more about how parts and structures behave and work. This will enable engineers to consider this phenomenon in the design of structures to guarantee their functionality and safety throughout their entire service life.

Since creep tests can take long hours or even days (especially for low load levels), the cyclic station concept, developed by Simões et al. [83] (Figure 5.1 (left)), was adapted for a three-station layout (Figure 5.1 (centre)) in order to enable the realization of multiple tests at the same time. Additionally, two thermal chambers were developed and assembled, one capable of reaching high temperatures only and a second, capable of reaching high and low temperatures. This combination allows to test a large number of SLJs under creep conditions at different temperatures.

Both thermal chambers use a resistance based heating element, to produce heat for high-temperature testing, a fan for a better temperature distribution inside the chamber, and a thermocouple to measure the temperature within the chamber. This temperature value is supplied to a controller, which is used to define the desired temperature and ensure a stable temperature evolution. The chambers also include a power button for regular use, and an emergency power shutdown button, for safety purposes.

For the low temperature capable chamber, an hydraulic circuit was projected, consisting of:

- Directional retaining valve;
- Safety overpressure valve;
- Cryogenic electro valve;
- Diffusor;
- Adaptors and lines.

The cyclic machine (Figures 5.1 (left and centre)) consists of a grip system to maintain the specimen's position while making sure it is aligned to allow for appropriate loading and the capture of creep deformation, a lever for applying a load to the test specimen that makes use of actuators

or hanging weights, and, precision potentiometers for measuring the rotation of the lever, which is then converted to the deformation acting on the joint [40]. Since the temperatures (both low and high) experienced inside the thermal chamber are out of the range of operation of the actuators, this needs to stay outside the chamber. Therefore, as shown in Figure 5.1 (right), the shaft holding the weights was extended and the base that supports the weights was placed outside the chamber. To support the cameras, as well as the bases of the actuators, two structures were built using Bosch Reworth aluminium profiles.

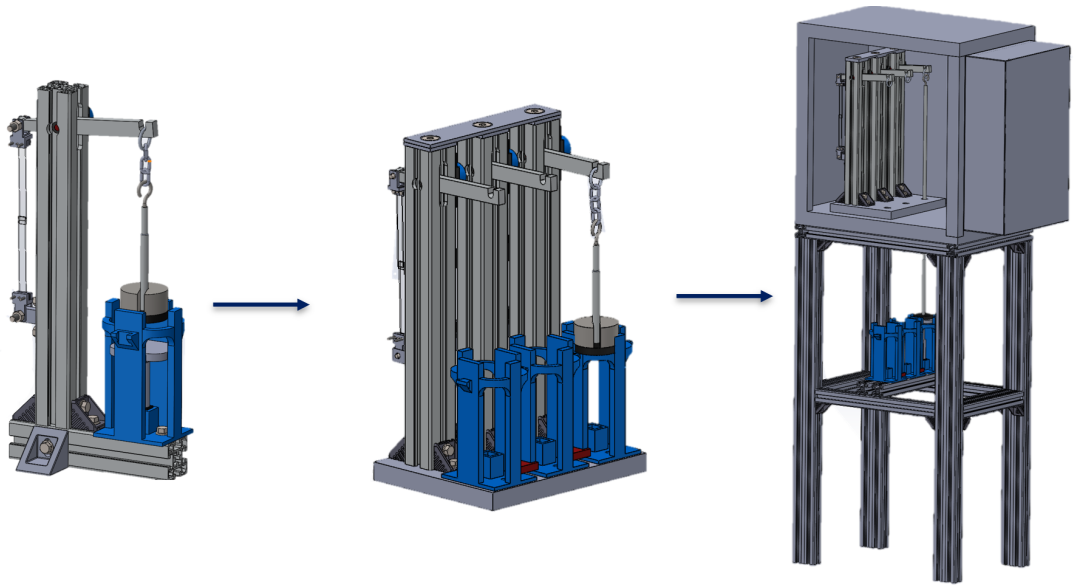


Figure 5.1: Cyclic creep station evolution.

Figure 5.2 shows the current state of the thermal chambers. At the time this dissertation was submitted, the cameras were not operational as they still do not have the complete electronic system (work that will be carried out by a specialised technician). It has therefore not yet been possible to test their performance.



Figure 5.2: Thermal chambers.

Chapter 6

Conclusions and Future Work

In the present work, the failure modes of two acrylic PSAs were experimentally characterised through DCB tests load in mode I (opening mode), mode III (out-of-plane shear mode) and peel tests. The experimental data obtained was used to feed multiple numerical models, and both results were compared and analysed.

For DCBs modes I and III, the direct method was applied to the adhesive, and the failure behaviour and fracture energy were obtained. The CTOD was evaluated through a DIC analysis, allowing the computation of cohesive laws for both adhesives in the different loading modes. A CZM was developed, and the material model of the adhesive was modelled using cohesive elements governed by the experimentally obtained cohesive laws. With the exception of adhesive B loaded in mode III, the numerical results exhibited overall good agreement with the experimental data. The obtained cohesive law for adhesive A in DCB mode I testing was later used to simulate peel specimens under different peeling angles. A good agreement was found between the average loads obtained in the plateau of the peel tests and the numerical results, especially for the tests where there was a minor influence of shear modes, like 90° peeling.

Regarding the peel tests, an apparatus was developed to allow the testing of the peel specimens under different inclinations. The peel specimens were composed, besides the PSAs, of an acrylic substrate and a 0.01 mm thickness steel backing. Both adhesives were characterised by 30, 60, 90, 120, 150 and 180° peeling, allowing for the creation of a complete load failure envelope. A study was done regarding the adhesive energy. It was concluded that if we account for the energy dissipated due to the bending of the steel backing, the adhesion energy remains approximately constant when varying the peeling angle, confirming the hypothesis that this is a material property. The fracture process zone was also characterised by digital processing of the images recorded during experimental tests. It was observed that for peeling angles smaller than 90°, the reduction in the angle promotes an increase in the length of the FPZ and a reduction in the height. For angles higher than 90° and smaller than 180°, we have a decrease in both dimensions of the FPZ, suggesting that, due to the direction of the force, we have higher cleavage forces, promoting higher stress concentrations at the peel front and consequently, an early failure of the adhesion, leading to smaller FPZ. For the 180° peel, it was observed that, due to the alignment of the peeling direction

with the sample, we have an increase in the shear forces, confirmed by an increase in the length of the FPZ and, therefore, a slight increase in the failure load when compared with the 120° and 150° peeling tests. A CZM was developed, where the obtained adhesion energies, together with the values obtained for the crack tip opening during stable crack propagation, were used to estimate a cohesive law. The numerical results presented very good agreement with the experimental values.

Regarding the hyperelastic study, the numerical results obtained show that the model developed is not able to accurately predict the adhesive's behaviour, highlighting the shortage of data to feed the model, particularly in a shear mode.

As future works, it is suggested to try to develop a CZM capable of predicting the behaviour of joints in real-life applications. For that, modes I and III needed to be combined to give more flexibility to the numerical model in different applications. Additionally, the hyperelastic model can be improved if more experimental data can be gathered. Planar tests and/or biaxial tests are good hypotheses for enhancing the performance of the numerical model since they can provide some data in a shear mode. If the previous two points are successful, the ultimate goal for future work will be to attempt to create a robust model consisting of a hyperelastic model capable of predicting the behaviour of adhesives combined with thin layers of cohesive elements or cohesive contact capable of predicting the failure mode of the joint.

Additionally, with the developed thermal chambers and cyclic creep stations, the PSAs can be studied under creep and cyclic creep conditions at different temperatures, allowing for a better overview of the applicability of these adhesives in real-life applications.

References

[1] Ricardo Carbas, Lucas Filipe Martins da Silva, Eduardo Marques, Alireza Akhavan-Safar, and A. Francisco G. Tenreiro. *Structural Adhesive Bonding in Aerospace Applications*. Engebook, 1st edition, 2022.

[2] Lucas FM Da Silva, Andreas Ochsner, and Robert D Adams. *Handbook of Adhesion Technology*. Springer Science & Business Media, 2011.

[3] S. Wu. *Polymer Interface and Adhesion*. CRC Press, New York, NY, 1 edition, 1982.

[4] Robert D Adams, John Comyn, William Charles Wake, and WC Wake. *Structural Adhesive Joints in Engineering*. Springer Science & Business Media, 1997.

[5] Edward M. Petrie. *Handbook of Adhesives and Sealants*. McGraw-Hill Education, 2007.

[6] S. L. A. H. Ebnesajjad and W. Andrew, editors. *Adhesives Technology Handbook*. 3 edition, 2015.

[7] S. Ebnesajjad and A. H. Landrock. *Adhesives Technology Handbook*. William Andrew, 2014.

[8] E. Marques, A. Barbosa, R. Carbas, A. Akhavan-Safar, and L. da Silva. *Introduction to Adhesive Bonding*. Wiley, 2021.

[9] D. E. Packham. *Handbook of Adhesion*. apr 2005.

[10] U.S. Lindholm. Some experiments with the split hopkinson pressure bar. *Journal of the Mechanics and Physics of Solids*, 12(5):317–335, 1964.

[11] C. d. S. P. Borges. Fracture envelope of automotive adhesives under impact. Master's thesis, Department of Mechanical Engineering, Faculty of Engineering of the University of Porto, 2019.

[12] L. F. M. da Silva, António G., and M. F. Moura. *Juntas Adesivas Estruturais*. Publindústria, 1 edition, 2007.

[13] R. Carbas, E. Marques, A. Akhavan-Safar, A. Barbosa, and L. da Silva. *Adhesive Bonding Technology and Testing*. Wiley, 2023.

[14] R. Adams. *Adhesive Bonding: Science, Technology and Applications*. Woodhead Publishing, 2021.

[15] M. F. S. F. de Moura Filipe J. P. Chaves, L. F. M. da Silva, D. A. Dillard, and V. H. C. Esteves. Fracture mechanics tests in adhesively bonded joints: A literature review. *The Journal of Adhesion*, 90(12):955–992, 2014.

[16] Lucas F. M. da Silva and Raul D. S. G. Campilho. Advances in numerical modeling of adhesive joints. In *Advances in Numerical Modeling of Adhesive Joints*, pages 1–93. Springer Berlin Heidelberg, Berlin, Heidelberg, 2012.

[17] Beatriz Duarte Simões. Determination of the cohesive law of structural adhesives using the direct method. Master's thesis, Department of Mechanical Engineering, Faculty of Engineering of the University of Porto, 2022.

[18] Toru Sugaya, Tatsuya Obuchi, and Chiaki Sato. Influences of loading rates on stress-strain relations of cured bulks of brittle and ductile adhesives. *Journal of Solid Mechanics and Materials Engineering*, 5:921–928, 2011.

[19] FJP Chaves, MFSF de Moura, LFM da Silva, and DA Dillard. Numerical validation of a crack equivalent method for mixed-mode i+ii fracture characterization of bonded joints. *Engineering Fracture Mechanics*, 107:38–47, 2013.

[20] Aleksandar Karac, Bamber R. K. Blackman, V. Cooper, Anthony J. Kinloch, S. Rodriguez Sanchez, Wern Sze Teo, and Alojz Ivanković. Modelling the fracture behaviour of adhesively-bonded joints as a function of test rate. *Engineering Fracture Mechanics*, 78:973–989, 2011.

[21] J. R. Rice. A Path Independent Integral and the Approximate Analysis of Strain Concentration by Notches and Cracks. *Journal of Applied Mechanics*, 35(2):379–386, June 1968.

[22] In Lin Ye, editor, *Recent Advances in Structural Integrity Analysis - Proceedings of the International Congress (APCF/SIF-2014)*, pages 595–598. Woodhead Publishing.

[23] J. D. Eshelby. The force on an elastic singularity. *Philosophical Transactions of the Royal Society of London. Series A, Mathematical and Physical Sciences*, 244(877):87–112, November 1951.

[24] Anders Biel and Ulf Stigh. Comparison of J-integral methods to experimentally determine cohesive laws in shear for adhesives. *International Journal of Adhesion and Adhesives*, 94:64–75, 2019.

[25] A. Wells. Unstable crack propagation in metals: cleavage and fast fracture. In *Proceedings of the crack propagation symposium*, volume 1, page 26028, 1961.

[26] Julien Jumel, Naoufel Ben Salem, Michal K. Budzik, and Martin E.R. Shanahan. Measurement of interface cohesive stresses and strains evolutions with combined mixed mode crack propagation test and backface strain monitoring measurements. *International Journal of Solids and Structures*, 52:33–44, 2015.

[27] B. Krull, J. Patrick, K. Hart, S. White, and N. Sottos. Automatic Optical Crack Tracking for Double Cantilever Beam Specimens. *Experimental Techniques*, 40(3):937–945, June 2016.

[28] Yoshitaro Sakata Nao Terasaki, Yuki Fujio, Shin Horiuchi, and Haruhisa Akiyama. Visualization of crack propagation for assisting double cantilever beam test through mechanoluminescence. *The Journal of Adhesion*, 94(11):867–879, 2018.

[29] J. Manterola, M. Aguirre, J. Zurbitu, J. Renart, A. Turon, and I. Urresti. Using acoustic emissions (ae) to monitor mode i crack growth in bonded joints. *Engineering Fracture Mechanics*, 224:106778, 2020.

[30] Vasco Daniel Castro Pires. Study of a novel curved single lap joint concept with non-uniform adhesive thickness. Master's thesis, Department of Mechanical Engineering, Faculty of Engineering of the University of Porto, 2023.

[31] Jianping Jing, Feng Gao, Janine Johnson, Frank Z. Liang, Richard L. Williams, and Jianmin Qu. Simulation of dynamic fracture along solder–pad interfaces using a cohesive zone model. *Engineering Failure Analysis*, 16(5):1579–1586, 2009.

[32] Istvan Benedek and Mikhail M. Feldstein. *Technology of Pressure-Sensitive Adhesives and Products*. CRC Press, 1 edition, 2009.

[33] David Yarusso. *Effect of rheology on PSA performance*, volume 1, pages 499–533. 12 2002.

[34] Copyright. In Michael J. Troughton, editor, *Handbook of Plastics Joining (Second Edition)*. William Andrew Publishing, Boston, second edition edition, 2009.

[35] Istvan Benedek. *Pressure-Sensitive Adhesives and Applications*. CRC Press, 2 edition, 2004.

[36] W. Brockmann and R. Hüther. Adhesion mechanisms of pressure sensitive adhesives. *International Journal of Adhesion and Adhesives*, 16(2):81–86, 1996. Special Issue: In honour of Dr K. W. Allen on the occasion of his 70th birthday.

[37] Gary A. Korba Lihua Li, Matthew Tirrell and Alphonsus V. Pocius. Surface energy and adhesion studies on acrylic pressure sensitive adhesives. *The Journal of Adhesion*, 76(4):307–334, 2001.

[38] I. Márquez, N. Paredes, F. Alarcia, and JI Velasco. Influence of acrylonitrile content on the adhesive properties of water-based acrylic pressure-sensitive adhesives. *Polymers (Basel)*, 14(5):909, 2022.

[39] M.J. Zajaczkowski. *Pressure Sensitive Adhesives in High Performance Applications*. The Adhesive and Sealant Council, Inc, 2010.

[40] Elio Michaël Dias Fernandes. Study of the cyclic creep behaviour of pressure sensitive adhesives. Master's thesis, Department of Mechanical Engineering, Faculty of Engineering of the University of Porto, 2023.

[41] D. Martina, Costantino Creton, P. Damman, Mélanie Jeusette, and A. Lindner. Adhesion of soft viscoelastic adhesives on periodic rough surfaces. *Soft Matter*, 8:5350–5357, 04 2012.

[42] P. Tordjeman, E. Papon, and J-J. Villenave. Tack properties of pressure-sensitive adhesives. *Journal of Polymer Science Part B: Polymer Physics*, 38(9):1201–1208, 2000.

[43] Ulf Stigh and Anders Biel. Effects of strain rate on the cohesive properties and fracture process of a pressure sensitive adhesive. *Engineering Fracture Mechanics*, 203:266–275, 2018. 8th ESIS TC4 International Conference- Fracture of Polymers, Composites and Adhesives.

[44] Mahzan Johar, King Jye Wong, and Nasir Tamin. Characteristics of adhesive joints under rate-dependent tensile loading. volume 660, 08 2014.

[45] Yasuhiro Goda and Toshiyuki Sawa. Study on the effect of strain rate of adhesive material on the stress state in adhesive joints. *The Journal of Adhesion*, 87(7-8):766–779, 2011.

[46] Arnaud Chiche, Pascal Pareige, and Costantino Creton. Role of surface roughness in controlling the adhesion of a soft adhesive on a hard surface. *Comptes Rendus de l'Académie des Sciences - Series IV - Physics*, 1(9):1197–1204, 2000.

[47] Marta Ortega Iguña, Mariane Chludzinski, and Jose Sánchez-Amaya. Comparative mechanical study of pressure sensitive adhesives over aluminium substrates for industrial applications. *Polymers*, 14:4783, 11 2022.

[48] A. Biel and U. Stigh. Cohesive zone modelling of nucleation, growth and coalesce of cavities. 204(2):159–174.

[49] Q. Yang and M. Thouless. Mixed-mode fracture analyses of plastically-deforming adhesive joints. *International Journal of Fracture*, 110:175–187, 2001.

[50] U. Stigh, K. S. Alfredsson, T. Andersson, et al. Some aspects of cohesive models and modelling with special application to strength of adhesive layers. *International Journal of Fracture*, 165:149–162, 2010.

[51] P. Olsson and U. Stigh. On the determination of the constitutive properties of thin interphase layers - an exact inverse solution. *International Journal of Fracture*, 41:R71–R76, 1989.

[52] F. Sun and B.R.K. Blackman. A dic method to determine the mode i energy release rate g, the j-integral and the traction-separation law simultaneously for adhesive joints. *Engineering Fracture Mechanics*, 234:107097, 2020.

[53] A. N. Gent and R. E. Petrich. *Proceedings of the Royal Society A*, 310:433–448, 1969.

[54] A. N. Gent and A. J. Kinloch. *Journal of Polymer Science: Polymer Physics Edition*, 9:659–668, 1971.

[55] PB Lindley. Ozone attack at a rubber-metal bond. *J Instn Rubb Ind*, 5(6):243–248, 1971.

[56] A. J. Kinloch, C. C. Lau, and J. G. Williams. The peeling of flexible laminates. *International Journal of Fracture*, 1994.

[57] I. Georgiou, H. Hadavinia, A. Ivankovic, A. J. Kinloch, V. Tropsa, and J. G. Williams. Cohesive zone models and the plastically deforming peel test. *The Journal of Adhesion*, 79(3):239–265, March 2003.

[58] Michael D. Bartlett, Scott W. Case, Anthony J. Kinloch, and David A. Dillard. Peel tests for quantifying adhesion and toughness: A review. *Progress in Materials Science*, 137:101086, August 2023.

[59] A. N. Gent and G. R. Hamed. Peel mechanics of adhesive joints. *Polymer Engineering & Science*, 17(7):462–466, 1977.

[60] A. N. Gent and G. R. Hamed. Peel mechanics. *The Journal of Adhesion*, 7(2):91–95, 1975.

[61] A.N. Gent and G.R. Hamed. Peel mechanics for an elastic-plastic adherend. *Journal of Applied Polymer Science*, 21(10):2817 – 2831, 1977.

[62] K. S. Kim and N. Aravas. Elastoplastic analysis of the peel test. *International Journal of Solids and Structures*, 24(4):417–435, 1988.

[63] K. S. Kim and J. Kim. Elasto-plastic analysis of the peel test for thin film adhesion. *Journal of Engineering Materials and Technology*, 110(3):266–273, 1988.

[64] Allan F Bower. *Applied mechanics of solids*. CRC press, 2009.

[65] M. Mooney. A Theory of Large Elastic Deformation. *Journal of Applied Physics*, 11(9):582–592, 09 1940.

[66] K.K. Dwivedi, P. Lakhani, S. Kumar, and N. Kumar. A hyperelastic model to capture the mechanical behaviour and histological aspects of the soft tissues. *Journal of the Mechanical Behavior of Biomedical Materials*, 126:105013, Feb 2022.

[67] R.W. Ogden, G. Saccomandi, and I. Sgura. Fitting hyperelastic models to experimental data. *Computational Mechanics*, 34(6):484–502, Aug 2004.

[68] H. Gründemann and R.W. Ogden. *Non-linear elastic deformations*, volume 65. Ellis Horwood Ltd, Chichester, distributors: John Wiley & Sons Ltd., 1984. XV, 532 S., £35.00.

[69] Eduardo W. V. Chaves. Hyperelasticity. In Eduardo W. V. Chaves, editor, *Notes on Continuum Mechanics*, pages 423–464. Springer Netherlands, Dordrecht, 2013.

[70] V. Dias, C. Odenbreit, O. Hechler, F. Scholzen, and T. Ben Zineb. Development of a constitutive hyperelastic material law for numerical simulations of adhesive steel-glass connections using structural silicone. 2013.

[71] Stephen K. Melly, Liwu Liu, Yanju Liu, and Jinsong Leng. A review on material models for isotropic hyperelasticity. *International Journal of Mechanical System Dynamics*, 1(1):71–88, 2021. _eprint: https://onlinelibrary.wiley.com/doi/pdf/10.1002/msd2.12013.

[72] A.F. Müller et al. Evaluation of hyperelastic constitutive models applied to airway stents made by a 3d printer. In *IFMBE Proceedings*, volume 83, pages 881–889, 2022.

[73] M.E. Çetin. Fabrication, characterization and mechanical testing of carbon fiber sandwich composites with nanoparticle included polyurethane adhesives. *Journal of Composite Materials*, 56:589–603, Dec 2021.

[74] Hyperelastic behavior of rubberlike materials.

[75] IIT library. 6.777j/2.751j material property database. https://yourlibrary.iit.edu/material_property_database, 2024. Accessed: 2024-02-27.

[76] Prusa Polymers. Technical Datasheet Prusament PETG, feb 2022.

[77] Simplify3D. Filament properties table, 2023. Accessed: March 2024.

[78] Prusa Polymers. Technical Datasheet Prusament PC Blend, feb 2022.

[79] Ulf Stigh, Anders Biel, and Daniel Svensson. Cohesive zone modelling and the fracture process of structural tape. 2:235–244.

[80] Beatriz D. Simões, Eduardo A. S. Marques, Ricardo J. C. Carbas, Steven Maul, P. Stihler, Philipp Weißgraeber, and Lucas F. M. da Silva. Rheological and mechanical properties of an acrylic psa. *Polymers*, 15(18), 2023.

[81] Beatriz D. Simões, Élio M. D. Fernandes, Eduardo A. S. Marques, Ricardo J. C. Carbas, Steven Maul, Patrick Stihler, Philipp Weißgraeber, and Lucas F. M. da Silva. An exploratory study on determining and modeling the creep behavior of an acrylic pressure-sensitive adhesive. *Materials*, 16(5), 2023.

[82] Stefanos Giannis and Robert D. Adams. Failure of elastomeric sealants under tension and shear: Experiments and analysis. *International Journal of Adhesion and Adhesives*, 91:77–91, 2019.

[83] Beatriz Simões, Élio Fernandes, Eduardo Marques, Ricardo Carbas, Steven Maul, Patrick Stihler, Philipp Weißgraeber, and Lucas Silva. Development of a cyclic creep testing station tailored to pressure-sensitive adhesives. *Machines*, 12:76, 01 2024.

Appendix A

Paper 1 - Development of a cohesive zone model to characterise the fracture behaviour of PSAs

Development of a cohesive zone model to characterise the fracture behaviour of PSAs

Hugo C. Sousa[1], Beatriz D. Simões[1], Eduardo A.S. Marques[2], Ricardo J.C. Carbas[1], Steven Maul[3], Patrick Stihler[3], Philipp Weißgraeber[4] and Lucas F.M. Silva[2]

1 Institute of Science and Innovation in Mechanical and Industrial Engineering (INEGI), Rua Dr. Roberto Frias, 4200-465 Porto, Portugal

2 Department of Mechanical Engineering, Faculty of Engineering, University of Porto, Rua Dr. Roberto Frias, 4200-465 Porto, Portugal

3 Robert Bosch GmbH, Corporate Research and Advance Engineering, 71272 Renningen, Germany

4 Faculty of Mechanical Engineering and Marine Technology, University of Rostock, 18059 Rostock, Germany

Abstract: In this study, the mode I fracture behaviour of two double-sided acrylic pressure-sensitive adhesives (PSAs) was studied using double cantilever beam (DCB) geometries. The J-integral was estimated, and the opening displacements at the crack tip were measured using a DIC analysis, thereby allowing the extraction of a cohesive law using the direct method. The study was then focused on the adhesive that presented a stable crack propagation under opening loading conditions and a similar procedure was adopted to obtain a cohesive law for mode III testing conditions. The obtained cohesive laws were implemented in finite element software through a cohesive zone modelling approach. The load-displacement curves of the experimental and numerical models were compared to evaluate the performance of the cohesive law. Moreover, the mode I law was validated using a different geometry. Peel tests were numerically simulated using the cohesive law obtained from DCB geometries. The results were compared with previously performed peel tests.

Keywords: Adhesive joints, Pressure-sensitive adhesives, J-integral, Cohesive law

1 Introduction

Pressure-sensitive adhesives (PSAs) are a flexible class of adhesives that don't require heat, solvent, or water activation to form bonds when applied lightly. Because of this special quality, PSAs are useful for a variety of purposes, such as labels, tapes, and decals, as well as in vital sectors like medical, automotive, electronics, and construction [1].

In the present work, double cantilever beam (DCB) specimens produced with PSAs are experimentally tested under mode I and mode III loading conditions. The J-integral is evaluated, and the displacements at the crack tip are measured using a DIC approach. Moreover, the cohesive law is estimated using the direct method and further implemented

in a cohesive zone model (CZM). The numerical results are then compared with the experimental data. For additional validation of the obtained cohesive law, this is implemented in a numerical model using peel specimen geometries.

1.1 Cohesive zone modeling

Damage mechanics examines the initiation and propagation of damage, integrating concepts from both continuum mechanics and fracture mechanics. For such analyses, a cohesive zone model (CZM) is frequently employed. CZMs typically utilize non-thick elements defining the interface between two solid surfaces. When a stress threshold is reached, these elements undergo a relaxation process based on the fracture energy criterion, simulating material degradation [2].

As stress increases to a critical level, a CZM element begins to exhibit damage, resulting in reduced stiffness and strength. These elements are connected through cohesive tractions and relative displacements, enabling the simulation of elastic behaviour [3]. This behaviour is linearly characterized in CZMs for all laws until critical thresholds for tension (t_n^0) or shear (t_s^0) are reached. The elastic response of cohesive elements is governed by an elastic constitutive matrix that relates stress and strain in both tension and shear:

$$\mathbf{t} = \begin{bmatrix} t_n \\ t_s \end{bmatrix} = \begin{bmatrix} K_{nn} & K_{ns} \\ K_{ns} & K_{ss} \end{bmatrix} \begin{bmatrix} \epsilon_n \\ \epsilon_s \end{bmatrix} = \mathbf{K}\epsilon \tag{1}$$

Damage initiation is determined by various criteria, with the quadratic nominal stress criterion being a common method, expressed as:

$$\left\{ \frac{\langle t_n \rangle}{t_n^0} \right\}^2 + \left\{ \frac{t_s}{t_s^0} \right\}^2 = 1 \tag{2}$$

In Equations 1 and 2, t_n and t_s represent the cohesive tractions in tension and shear, while ϵ_n and ϵ_s denote the corresponding strains. The use of Macaulay brackets indicates that compressive stresses do not contribute to damage initiation [4,5]. When this criterion is met, material degradation occurs, leading to softening as dictated by the CZM until failure.

1.2 J-integral

The J-integral, pioneered by Rice [6], serves as a fundamental approach in fracture mechanics, capable of evaluating the deformation near crack tips across both linear and non-linear elastic materials. It can be defined as:

$$J = \int_\tau \left(U\, dy - T \frac{\partial u}{\partial x}\, d\tau \right) \tag{3}$$

where U represents strain energy density, T is the traction vector, and u is the displacement field. The J-integral is particularly valued for its path independence. This feature allows the integral to measure the energy release rate for crack propagation reliably, irrespective of the integration path (τ) around the crack tip, under certain conditions. These conditions include consistent energy storage across the x-direction and the absence of any obstacles within the contour that could affect the energy calculations [6, 7].

This method's robustness is exemplified in its application across varied experimental conditions where it remains accurate despite potential complexities in crack tip geometry. The J-integral's ability to precisely define fracture mechanics makes it an indispensable tool in the characterisation of materials under stress, aiding in the accurate assessment of the critical crack tip opening displacement (CTOD) through methods like Digital Image Correlation (DIC) [8]. This technique utilises non-contact optical measurements to track displacement and strain, facilitating a detailed analysis of fracture behaviour and stress fields at the crack tip.

1.3 Direct method for DCB testing

The CZM utilises a cohesive law that specifies the tractions exerted by the substrates onto the adhesive surfaces, essentially representing the adhesive's material volume properties. The cohesive law fundamentally depends on the separation of the bonded surfaces, as discussed extensively by Yang and Thouless [9] and Stigh et al. [10].

The cohesive law describes the relationship between the traction vector components and the separation vector of the surfaces. Theoretical groundwork for measuring these laws using the DCB specimen has been laid by Olsson and Stigh [11]. In this project, the cohesive law is derived through the direct method.

The direct method assumes that during stable crack propagation, the fracture process zone (FPZ) translates in a self-similar manner along the specimen ahead of the crack tip. The cohesive law is then deduced by differentiating the fracture toughness with respect to the initial crack tip opening displacement [12].

In DCB specimen configurations, stable mode I crack growth is facilitated by loading through transversal forces F [13]. The J-integral is calculated as follows:

$$J = \frac{1}{b} F(\theta_{up} - \theta_{lo}), \tag{4}$$

where θ represents the rotation at the loading points (for the upper (up) and lower (lo) beams), and b is the width of the crack propagation region.

Choosing the integration path τ vertically simplifies the calculation since $d\tau = dy$ and the tractions T at the free edge are zero. Considering w as the CTOD , the J-integral can be described as:

$$J = \int_0^{w_0} \sigma(w)\, dw. \tag{5}$$

Here, w_o is the critical CTOD (when traction becomes 0) and σ is identified as the average cohesive stress across the tape thickness, facilitating the determination of the cohesive law, $\sigma(w)$, by differentiating J with respect to w. This setup assumes nearly uniaxial strain due to stiff adherends, ensuring path independence of J.

Combining Equations 4 and 5, the cohesive law is obtained:

$$\sigma = \frac{\partial J}{\partial w} = \frac{1}{b}\frac{\partial}{\partial w}F(\theta_{up} - \theta_{lo}) \tag{6}$$

Shear modes testing

Figure 1 illustrates the fundamental deformation modes in a two-dimensional context. In three-dimensional scenarios, two orthogonal shear components are also considered. Therefore, the normal component of the traction vector is denoted as σ, and the in-plane components are τ_1 and τ_2, with the corresponding deformation measures being w, v_1, and v_2, respectively. When only one of the deformation modes is active, terminology from fracture mechanics is adopted. Specifically, Mode I loading is characterized by the dominance of σ and w, whereas Modes II and III are characterized by the dominance of τ and v components [14].

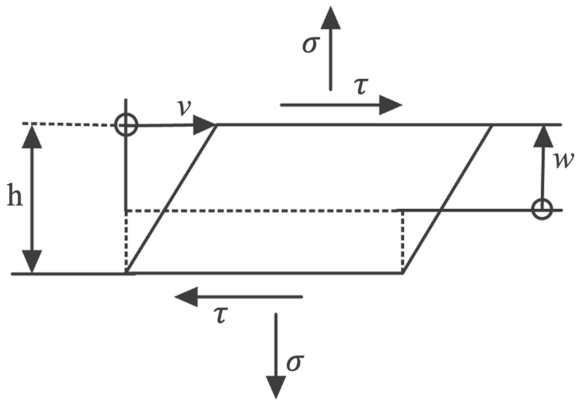


Figure 1: The tape with thickness h exhibits two modes of deformation: peel (w) and shear (v). Conjugated stress components σ and τ. Adapted from [14].

According to Stigh et al. [14], the same principles used to derive the Mode I cohesive law can be applied to derive the Mode III cohesive law, with the only changes being the replacement of σ with τ and w with v. Therefore the cohesive law, for a shear mode loading condition, can be extracted as:

$$\tau = \frac{\partial J}{\partial v} = \frac{1}{b}\frac{\partial}{\partial v}F(\theta_{up} - \theta_{lo}) \tag{7}$$

2 Experimental details

2.1 Materials

This work investigated two distinct double-sided acrylic PSAs: Adhesive A, composed of a highly shock-absorbing black acrylic foam, and Adhesive B, a grey foam acrylic. Adhesives A and B are 0.3 and 1.1 mm thick, respectively, and both have a Young modulus of 0.499, according to their manufacturers.

Due to its clear optical properties, transparent polymethyl methacrylate (PMMA) was selected for the substrates in the DCB specimens. PMMA facilitated direct visual observations of the PSA's fracture behaviours and damage processes throughout the testing phases. The mechanical properties of PMMA are detailed in table 1 [15].

Table 1: Mechanical properties of PMMA [15].

Density	Young's modulus	Poisson's ratio
1200 kg/m^3	1.8 - 3.2 GPa	0.35 - 0.4

2.2 Specimen manufacturing

DCB specimens were made for mode I and III testing to determine the cohesive laws and fracture energy of the acrylic PSAs. The PMMA substrates were cleaned with isopropyl alcohol to get rid of any grease and residue that might have affected the adhesion process. The geometry of the DCB specimens was based on the work developed in [13], and is shown in Figure 2, where t is the adhesive tape thickness.

To load the DCB in mode I while allowing it to rotate freely, two steel blocks with a passing-through hole were bonded to the substrates using a two-component polyurethane structural adhesive (SikaForce®—325 TC L 60). The steel block faces that maintained contact with the PMMA adherents were previously subjected to sandblasting and cleaned with acetone.

The surface of the specimens near the crack tip was coated with white matte paint and speckled with black dots to allow for a further DIC analysis. Lastly, all the specimens were assembled with the acrylic PSA in a mould with 23 kPa applied to each joint and then rested for 72 hours before being tested.

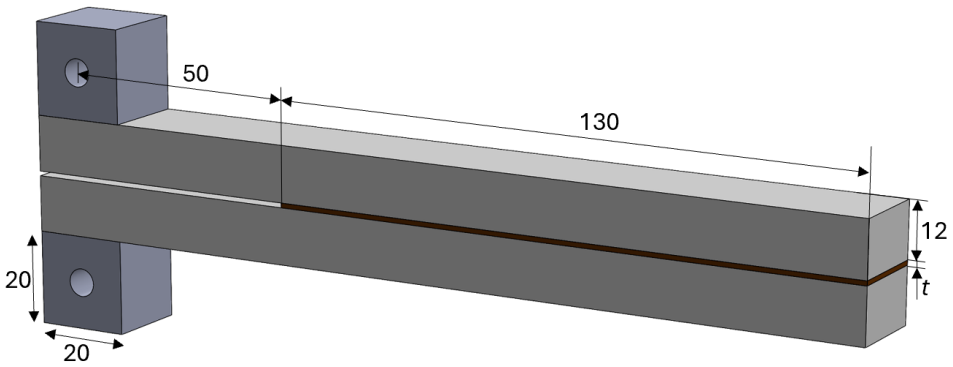


Figure 2: DCB specimens' geometry for mode I testing, in mm.

Vacuum condition manufacturing

During the manufacturing process of joints using these adhesives, the presence of air entrapment has been notice at the interface between the adhesive and the second substrate that needs to be fixed. This complication was noted mainly in Adhesive A. Adhesive B is thicker and foamier, so the pressure exerted by the mould and the weights on the DCBs produced with this adhesive is sufficient to remove the air bubbles and guarantee good adhesion. To overcome this problem, the DCB specimens were produced in a closed atmosphere with low pressure. Although it was not possible to achieve a perfect vacuum environment during the manufacture of these joints, from now on the samples produced in this condition are labelled as vacuum-produced for simplicity. Figure 3 clearly illustrates the difference between the adhesives produced with and without vacuum condition manufacturing. As can be seen, the samples produced under the latter conditions, although still presenting some defects on the lower edge, show considerable improvements over the others.

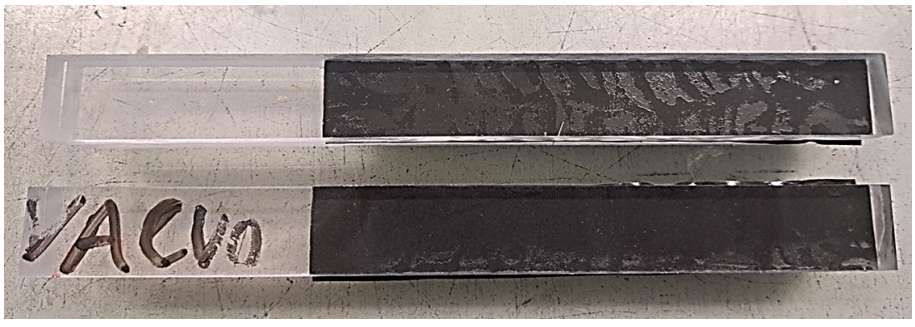


Figure 3: Adhesive A DCBs produced with (bottom) and without (top) a vacuum condition manufacturing.

2.3 Testing procedure

A quasi-static machine, INSTRON® 3367 (Illinois ToolWorks, Hopkinton, Massachusetts, USA), equipped with a 1 KN load cell, was used for all tests. The tests were performed in displacement control at a load rate of 2 mm/min. Data was collected at a rate of 5 points per second. For every test condition, a minimum of three specimens were examined.

The test images were captured using a digital camera (Nikon D5300) with a Nikon AF-P NIKKOR 18-55mm f/3 lens. The camera was positioned in front of the specimens using a laser beam leveler to ensure that the lens plane was perpendicular to the observation surface.

2.3.1 DCB mode I testing

The DCB specimens were fixed to a universal testing machine using stiff steel pins that connected the end blocks to the machine's attachment elements. SICK® (Waldkirch, Germany) TMS22E inclinometers were also attached to the end blocks to measure the rotation angles at the load introduction points, a crucial aspect of the direct method. This method requires the synchronised monitoring of the applied load and rotation angles (to assess Mode I fracture toughness) and CTOD (to derive the cohesive law). In sum, the testing machine captured the load-displacement curve, inclinometers measured the rotations at loading points, and the camera equipment recorded the opening displacements at the crack tip. The images for the CTOD estimation were processed using the GOM Correlate software through a DIC analysis. To ensure stable crack propagation, the specimens were initially subjected to a small pre-load in tension. Figure 4 shows the DCB mode I testing setup.

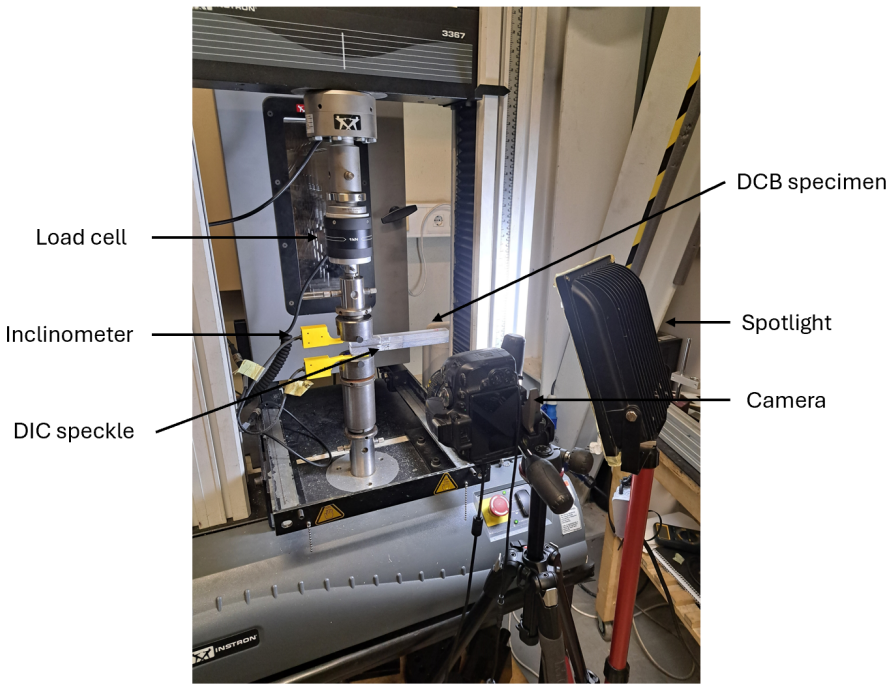
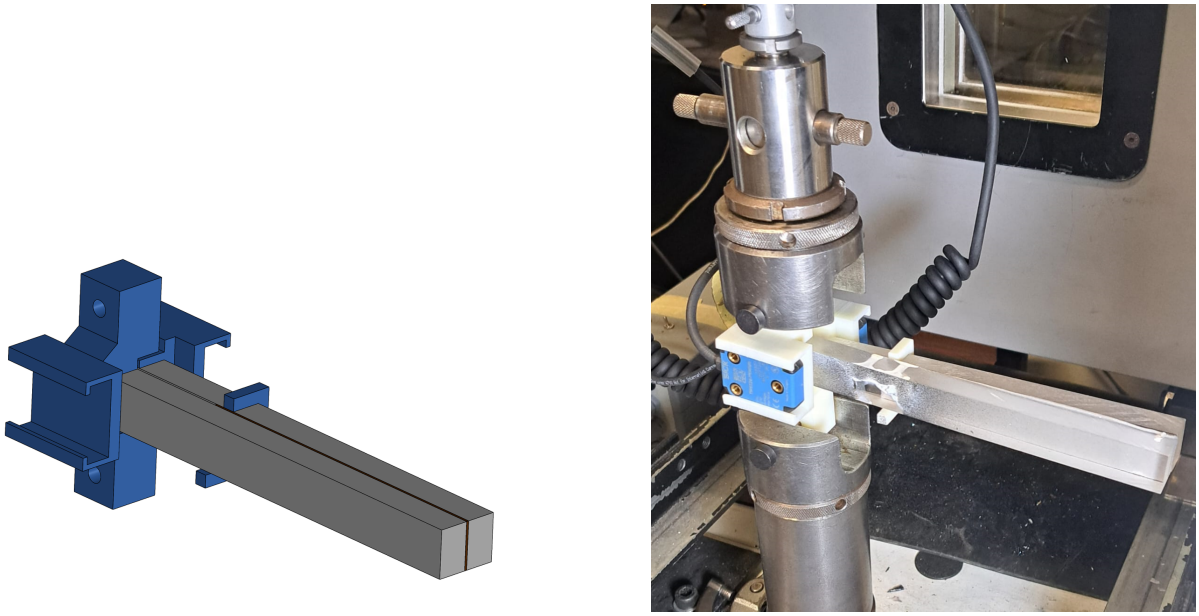


Figure 4: DCB mode I testing setup.

2.3.2 DCB mode III testing

The mode III DCB tests were conducted using a similar configuration to the one mentioned previously. Considering that, due to space limitations, the inclinometer supports used in the mode I tests could not be employed, a 3D-printed component was created to load the specimens instead of steel blocks. This component was printed with an 80% infill using a Prusa filament of polycarbonate (PC). This material was chosen since it produces better mechanical properties when compared to other commercially available filaments like PLA or PETG while allowing for relatively unproblematic manufacturing.

The component is attached to the substrate through compression and features a side cavity to support the inclinometers. It also has a pass-through hole for loading via a stiff steel pin connected to the tensile machine, ensuring the substrate can freely rotate. During this test, DIC was used in a similar setup to the one used in the mode I test to measure the CTOD. However, since the samples are subjected to shear loading, tracking the speckle pattern on the backplane of the adherent is not feasible because the adhesive obstructs the camera's view. To address this, a small part was designed and 3D printed. This is attached to the adherent through compression and extends the adherent so that its displacements can be measured on a plane aligning with the front face of the other adherent. Figure 5a shows the CAD model of the supports for the inclinometers and DIC on the DCB specimen, and Figure 5b displays the final setup with the DCB specimen mounted in the testing machine with the 3D-printed supports.



(a) (b)

Figure 5: DCB specimens with the 3D-printed supports for the inclinometers and DIC: (a) CAD model and (b) testing setup.

3 Experimental results

This section presents the experimental results. In all the graphs here illustrated, the solid lines represent the average curve of all the tests done for a given condition, while the shadow areas represents the respective standard deviation.

3.1 DCB mode I testing

The results for the load-displacement curves measured by the test machine for Adhesive A and B are presented in Figures 6 and 8. In both adhesives, we can see that, in the elastic region, we have two different stages. As reported by Simões et al. in [16], in the initial phase of the test, the load rises almost linearly, reflecting the linear elastic behaviour of the substrate. At this stage, the PMMA substrate's properties predominantly influence the joint's overall behaviour. At higher loads, the non-elastic behaviour of the PSA becomes evident, resulting in a change in the slope of the curve. This second phase concludes when damage appears and starts to propagate.

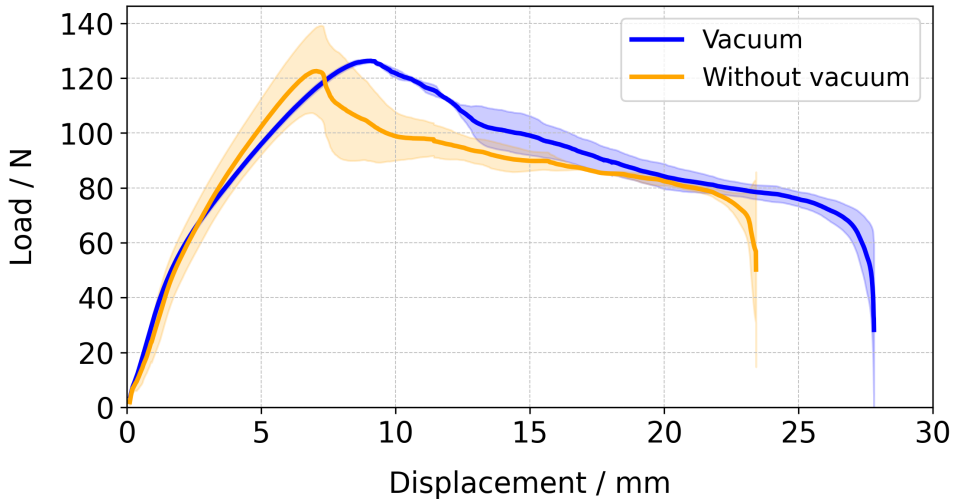


Figure 6: Load-displacement curves for DCB tests of adhesive A.

In adhesive A DCB test specimens, it was observed that the samples produced in a vacuum environment, which presented fewer defects, had a much smaller dispersion in the results. The vacuum samples presented approximately a 4% increase in the peak force (121.3 ± 12.92 N versus 126.4 ± 0.49 N) and a 15% increase in the average displacement at failure when compared to the samples produced at ambient pressure.

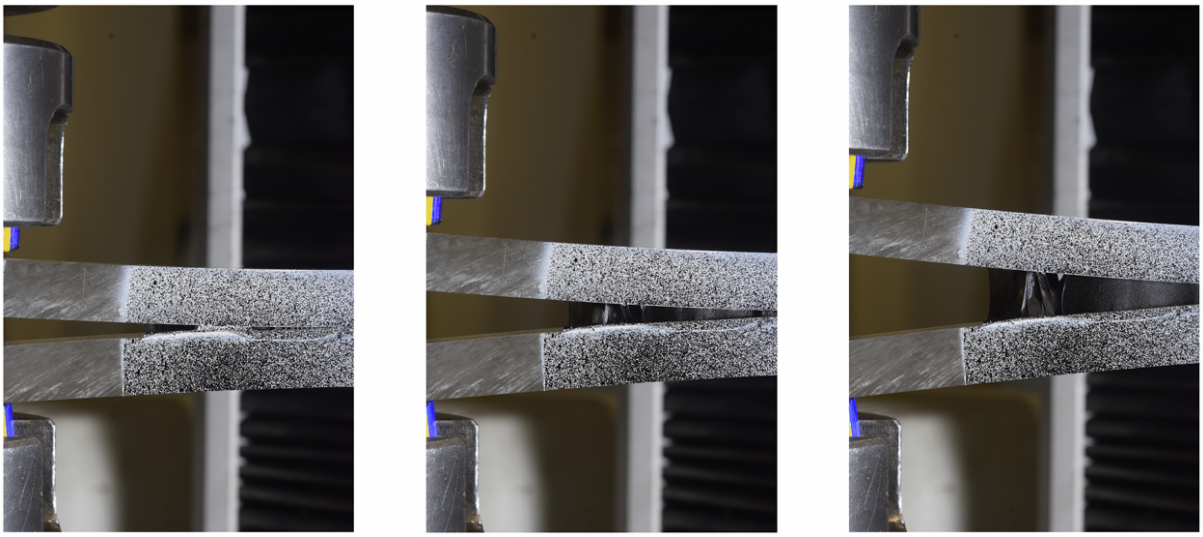


Figure 7: Three different timestamps for DCB being loaded with Adhesive A: elastic region (left), when reaches the maximum load (centre) and during damage propagation (right).

When the specimen was loaded, the air entrapment shown in Figure 3 (top) caused random interfacial failure through the specimen, producing high scatter values in the damage propagation portion of the load-displacement curve. This dispersion resulted directly from the abrupt failure that occurred each time the propagation of the interfacial

crack reached a non-bonded area. Figure 7 presents, for a DCB produced with adhesive A, the evolution of the CTOD in three different timestamps: in the elastic region (left), when it reaches the peak load (centre), and on the stable damage propagation zone (right). This adhesive, due to its dark colour, makes it difficult to observe the phenomenon of cavitation and fibrillation.

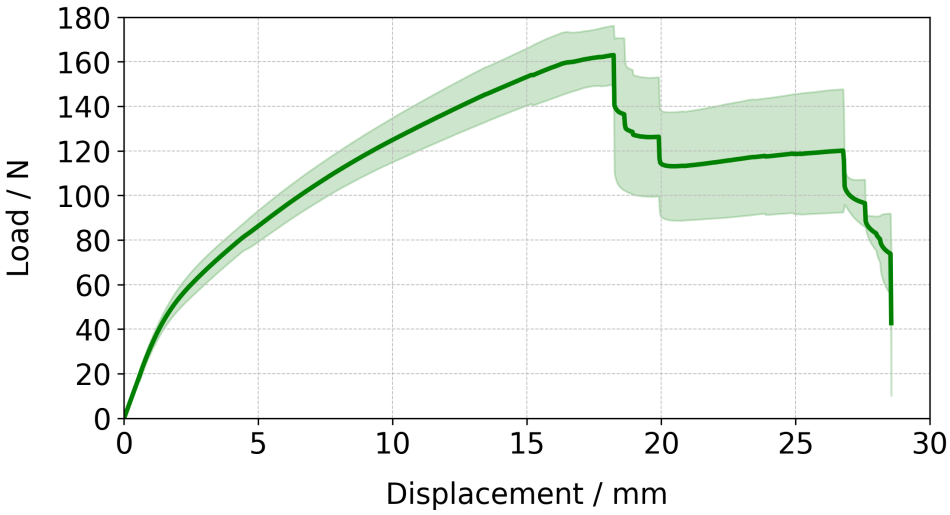


Figure 8: Load-displacement curves for DCB tests of adhesive B.

In adhesive B DCB test, we obtain a peak load of 152.27 ± 12.00 N. This curve presented a failure by steps, as can be observed in Figure 9.

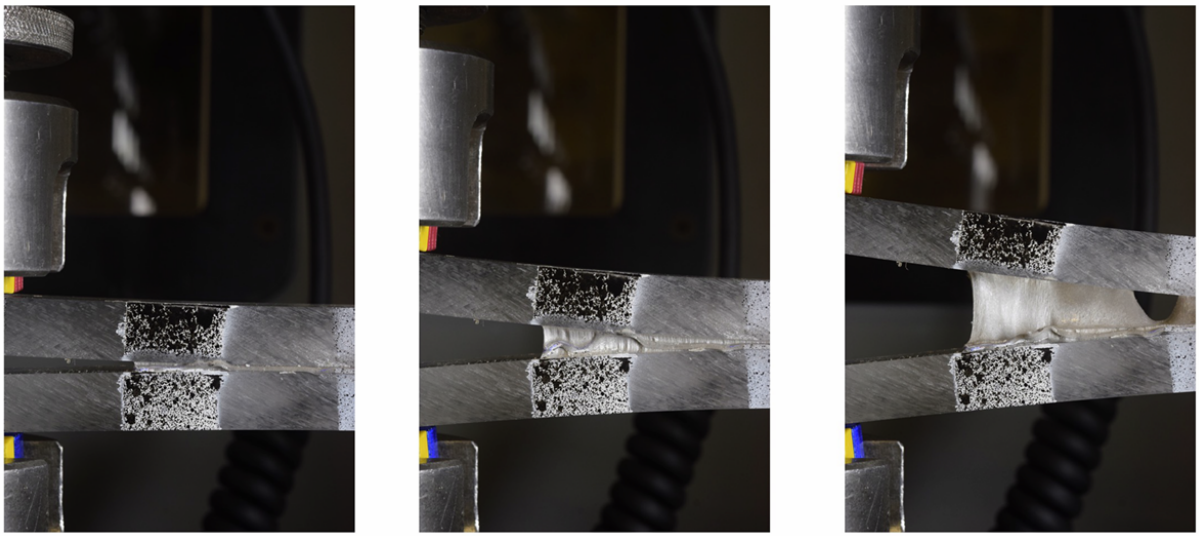


Figure 9: Three different timestamps for DCB being loaded with Adhesive B: elastic region (left), when reaches the maximum load (centre) and during damage propagation (right).

Adhesive B, being a double-sided tape, has adhesive layers on both sides of a carrier. This dual-layer structure causes, as can be seen in Figure 9, asymmetric loading on the

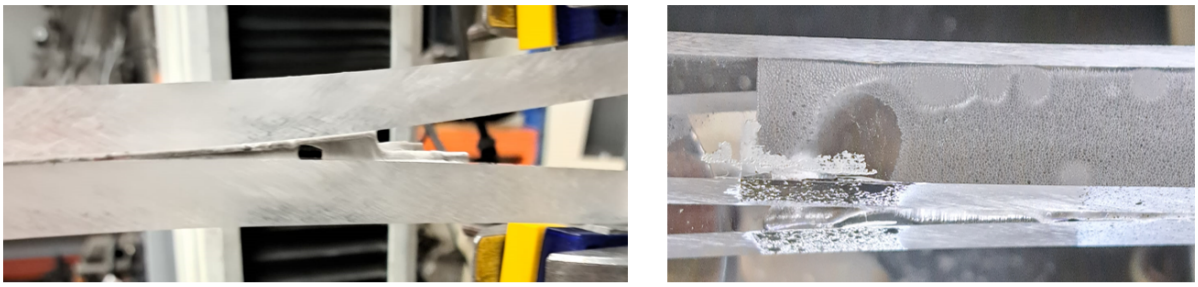


Figure 10: Detail of interfacial failure propagation (left), and cavitation phenomena (right) in adhesive B.

adhesive's top and bottom sides, which causes asymmetric fibrillation. In Yamaguchi's work, [17], this behaviour of the adhesive has also been observed, and, additionally, it was also noted that under certain circumstances, the elongated side tends to detach before the system returns to the symmetric state.

It is noticeable in Figure 10 (left) that the abrupt propagation of a crack throughout the interface is directly responsible for the large decreases in load. In contrast to adhesive A, where the cavity coalescence forms multiple fibrils that, by multiple breaking, ensure a smoother crack propagation, the adhesive B layer is being loaded not only in the crack front but in a large area of the adhesive layer, preventing smoother crack propagation. It can be seen, from a top point of view (Figure 10 (right)), that the phenomena of cavitation in adhesive B expand for a large area before the sudden failure of a large portion of the adhesive.

Based on the load-displacement curves and using Equation 4, the critical energy release rate in mode I was evaluated. Figure 11 shows the obtained values of J for adhesive A. As expected, the DCBs produced in a vacuum condition led to higher energy release rate values than those made at ambient pressure (0.90 ± 0.0088 N/mm versus 0.63 ± 0.11 N/mm). These samples presented a smoother crack propagation with a well-defined plateau.

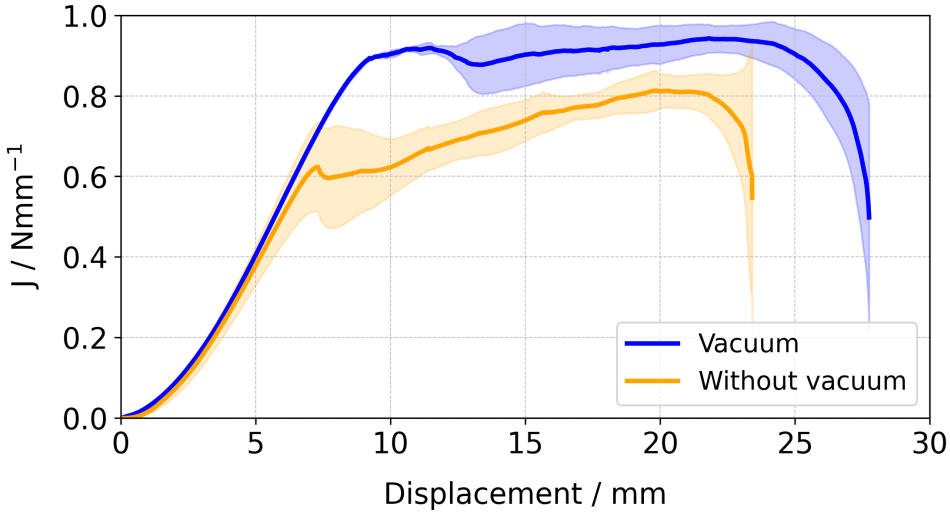


Figure 11: Fracture energy curves based on the J-integral approach for adhesive A.

Adhesive B (Figure 12), as expected based on the results obtained for the load-displacement curve, presented sudden drops in fracture energy after reaching the peak value (1.90 ± 0.19 N/mm). This indicates that the fracture energy curve will show initiation values rather than a plateau area each time a section of the adhesive tape debonds from the substrate. Nevertheless, when calculating the cohesive law, the most critical part of the curve is the segment leading up to the maximum energy value. Consequently, the unusual behaviour observed in the energy beyond this point will have minimal impact on the derived cohesive law. When comparing the values obtained for Adhesive A and B, it is clear that the latter can absorb much more energy when loaded in mode I.

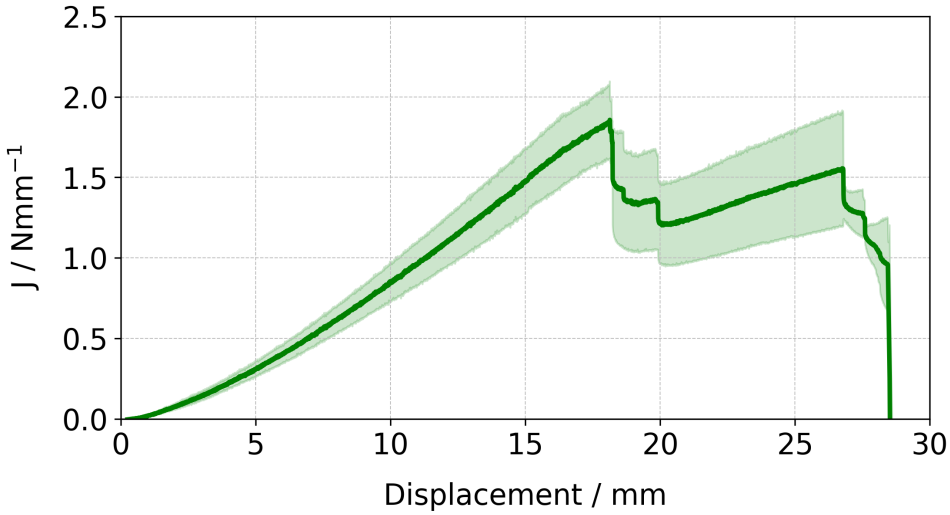


Figure 12: Fracture energy curves based on the J-integral approach for adhesive B.

The CTOD was measured through a DIC analysis, and, using Equation 5, it was possible to determine the cohesive law for both adhesives. Due to the noise associated

with the measuring devices, like inclinometers, load cell, and DIC, the experimentally collected data was filtered using a Savitzky-Golay filter in order to produce a smoothed cohesive law for both adhesives.

For adhesive A (Figure 13), the average peak stress was nearly the same for both approaches (0.74 MPa without a vacuum condition manufacturing versus 0.69 MPa with). However, as expected and in agreement with the values obtained for the J-integral approach, by analysing the obtained cohesive law, it is clear that the samples produced in a vacuum environment were able to accumulate considerably more plastic energy before failure.

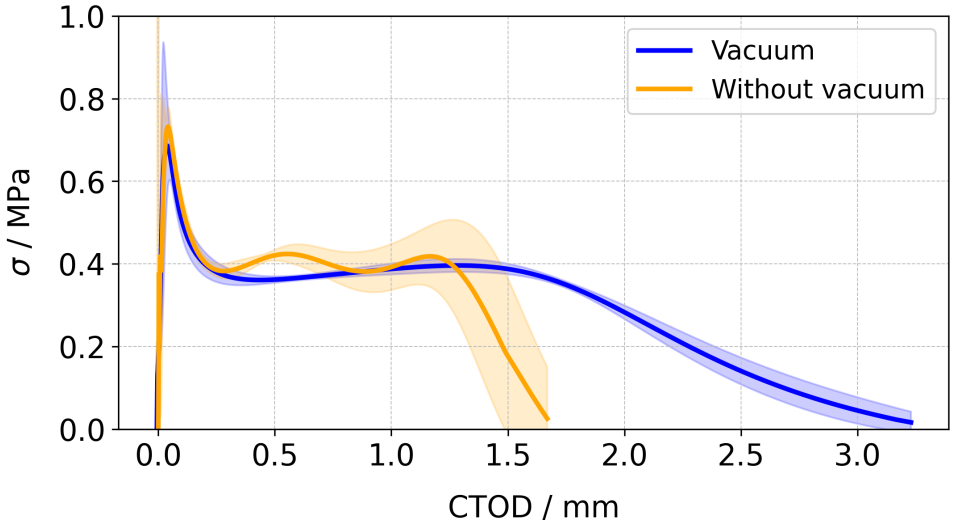


Figure 13: Average cohesive law for adhesive A.

For adhesive B, the average maximum stress was 0.93 MPa, and the critical separation length value was approximately 7.4 mm.

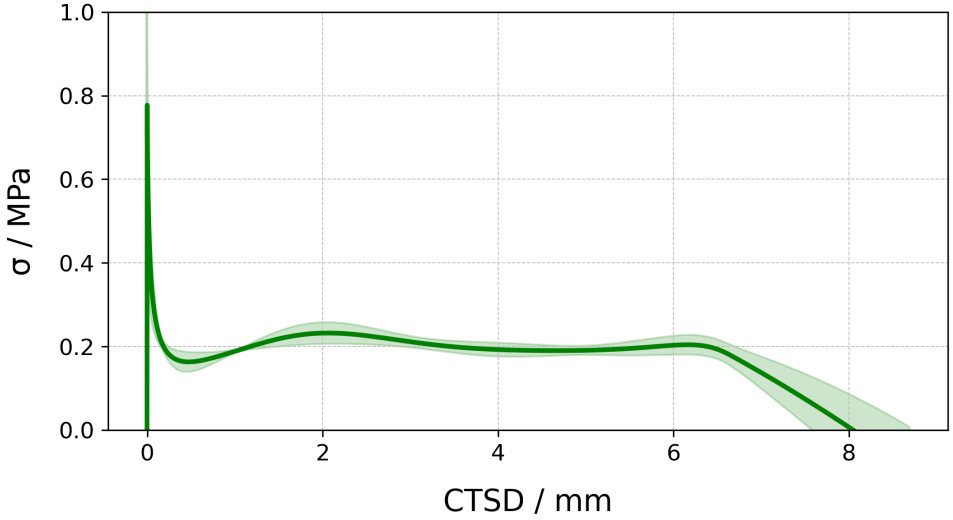


Figure 14: Average cohesive law for adhesive B.

Considering that adhesive B did not achieve a stable crack propagation, only adhesive A will be studied in the rest of this work.

3.2 DCB mode III testing

The high displacement characteristics of PSAs made mode II tests, such as End-Notched Flexure (ENF), impractical because the substrates failed to withstand the required loads for stable crack propagation. Therefore, to characterize these materials under shear loading conditions, mode III DCB tests were conducted.

Figure 15 represents the evolution of the crack tip shear displacement (CTSD) during three different timestamps. This adhesive showed the deformation of a large layer of adhesive, a behaviour similar to that observed in the mode I test conditions.

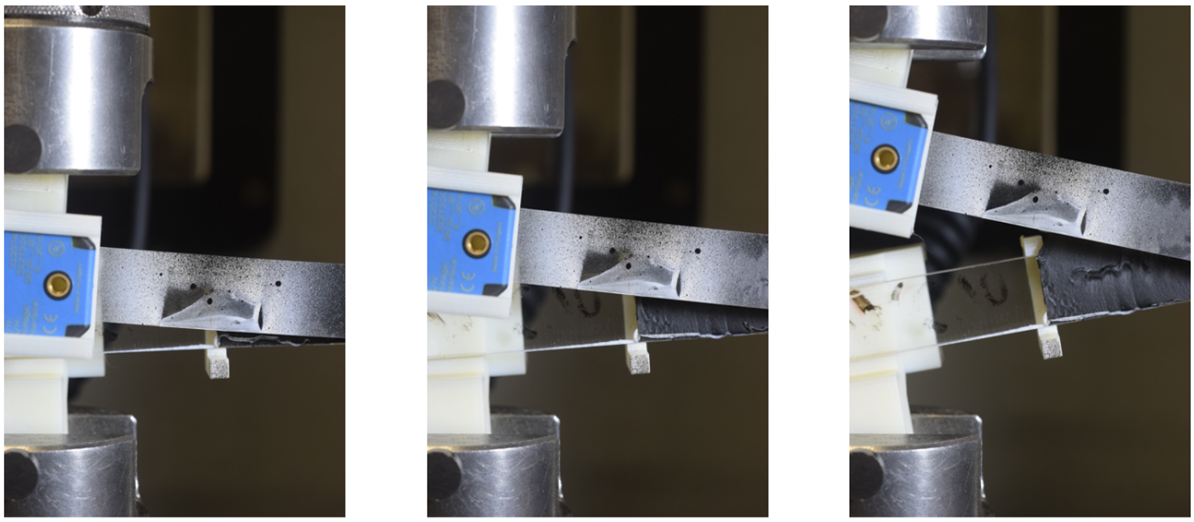


Figure 15: Three different timestamps for DCB being loaded in mode III with Adhesive A.

The results obtained for the load-displacement curves and fracture energy are presented in Figures 16 and 17, respectively.

Adhesive A presented a maximum load of 177.6 ± 5.6 N and a fracture energy of 0.80 ± 0.1. Despite the increase in the values of load in comparison to the mode I result, the values of energy remain approximately the same due to a decrease in the rotations of the substrates.

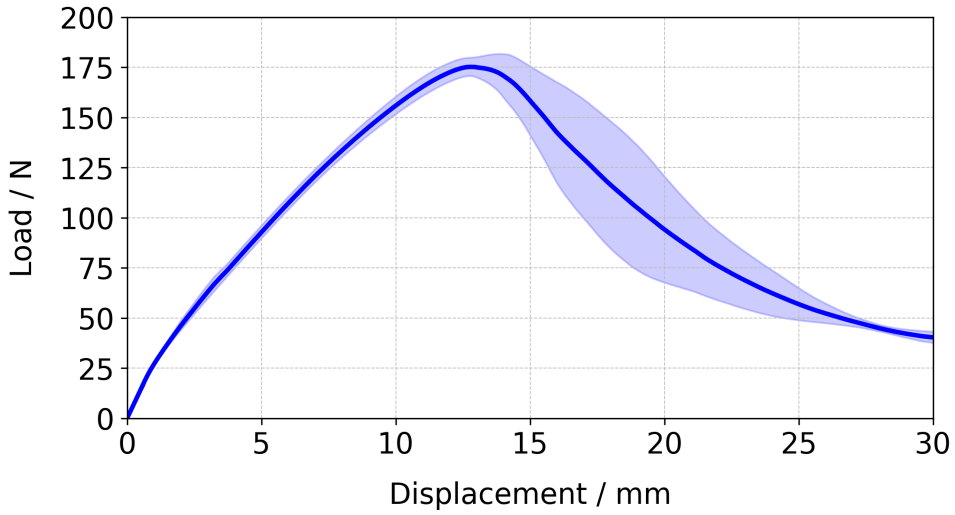


Figure 16: Load-displacement curves for DCB mode III testing with adhesive A.

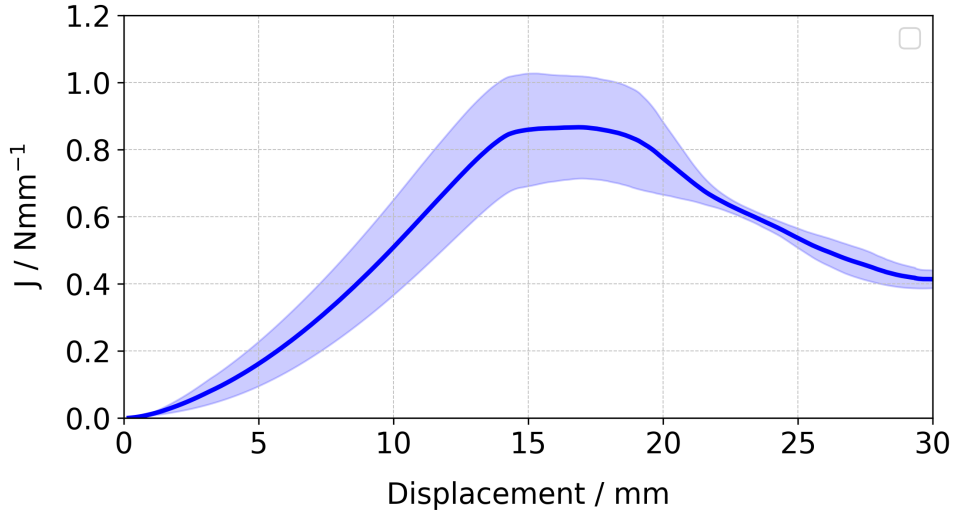


Figure 17: Fracture energy curves based on the J-integral approach for DCB mode III testing with adhesive A.

As described in section 1.3, since in mode III loading conditions the shear components are dominant, Equation 7 can be used to directly calculate the cohesive law. The CTSD were measured using DIC and the obtained cohesive law is presented in Figure 18. The shear stresses increase until a maximum of around 0.2 MPa, for a CTSD of 3.7 mm and then decrease to zero for an average crack displacement of 7.4 mm. Despite both tensile and shear loading modes presenting similar values of fracture energy, it was expected that the obtained stresses would be smaller in the latter since in this loading mode the displacements at the crack tip were much higher, leading to larger areas of adhesive layer. As will be further explained in the numerical details, the obtained laws were approximated to a bilinear cohesive law (dashed line) due to the presence of noise in the extraction

process.

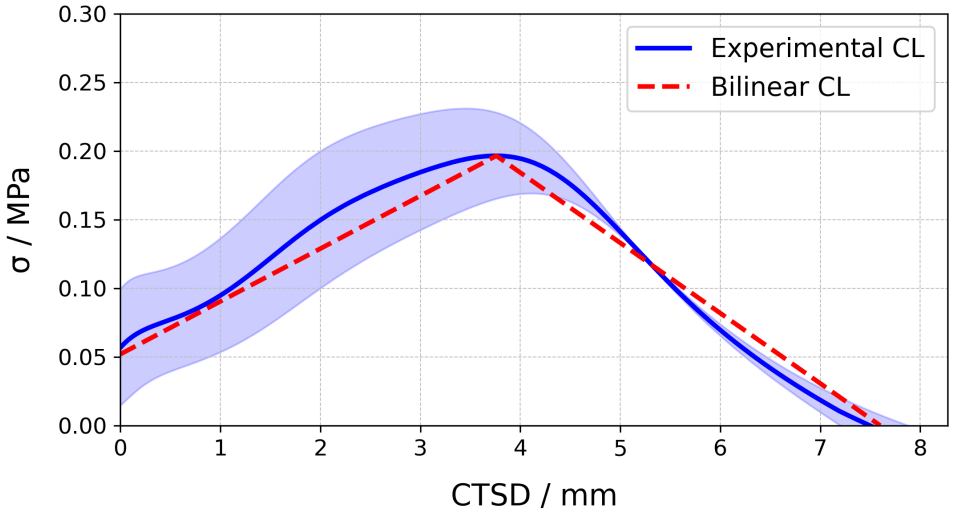


Figure 18: Average cohesive law for DCB mode III testing with adhesive A.

4 Numerical analysis

4.1 DCB mode I modelling

ABAQUS® software was used for the finite element simulations. A 2D model (with an out-of-plane thickness of 19mm) was employed to reduce the computation cost. A convergency study was performed to ensure that the mesh size accurately predicted the behaviour of the adhesive without unnecessarily increasing the computational time. The adherents and the steel blocks were modelled using 39422 plain strain elements, with reduced integration (CPE4R), while the adhesive was modelled using 260 linear quadrilateral cohesive elements (COH2D4) with one element per thickness. The steel blocks were fixed to the acrylic substrates using a tie constraint since the displacements that occur at the interface between these two bodies are not relevant. The final mesh, as well as the boundary conditions applied in the model, can be seen in Figure 19.

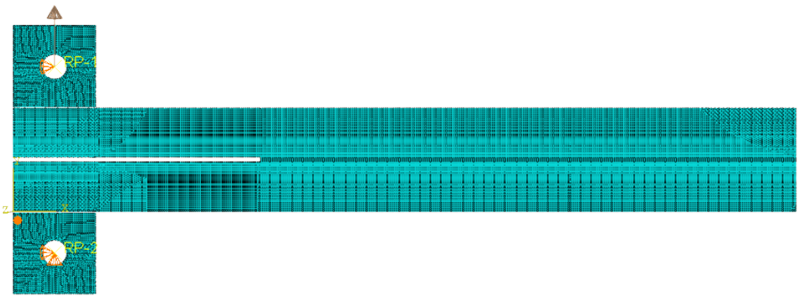


Figure 19: Mesh and boundary conditions applied in the DCB numerical model.

The cohesive law obtained for adhesive A was used to feed the CZM model. The numerical model fed with experimental data obtained from DCBs produced in a vacuum environment (Figure 21) presented exceptional accuracy in predicting this adhesive's load-displacement curve. Due to the low variability in experimental outcomes, the average curve excellently represented all tested specimens, enhancing the predictive accuracy of the model. Notably, the production of DCB specimens in vacuum conditions significantly reduced air entrapment at the interface, resulting in smooth and stable crack propagation strictly along the interface. Consequently, the cohesive elements in the numerical model, which specifically address crack propagation direction, were able to simulate this behaviour precisely.

In contrast, as illustrated in Figure 20, the results show higher dispersion, which compromised the model's ability to accurately predict the joint behaviour. Not only was the failure load lower than expected, but the damage propagation was also inaccurately predicted. This outcome was expected since, in the absence of vacuum conditions, damage propagation tends to be highly irregular throughout the specimen.

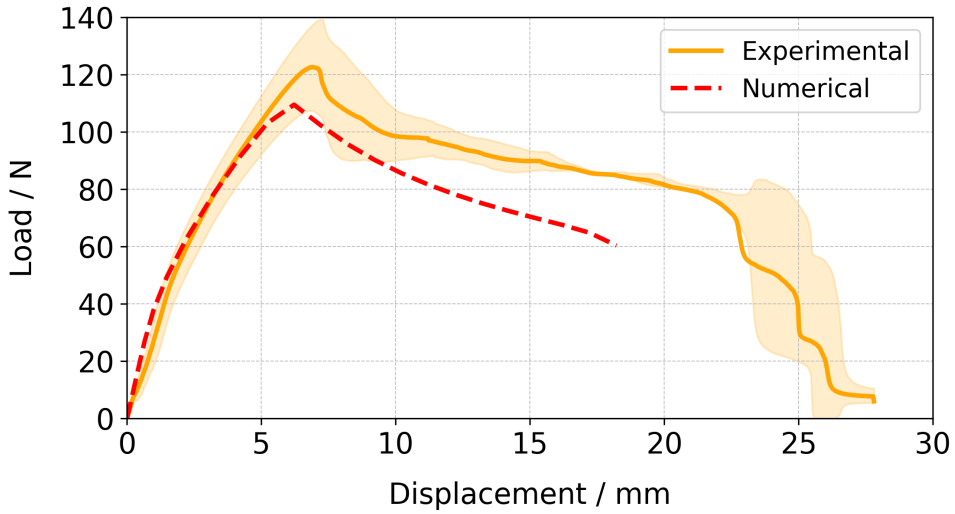


Figure 20: Comparison between experimental and numerical load-displacement curves for DCB mode I testing with adhesive A produced without vacuum condition manufacturing.

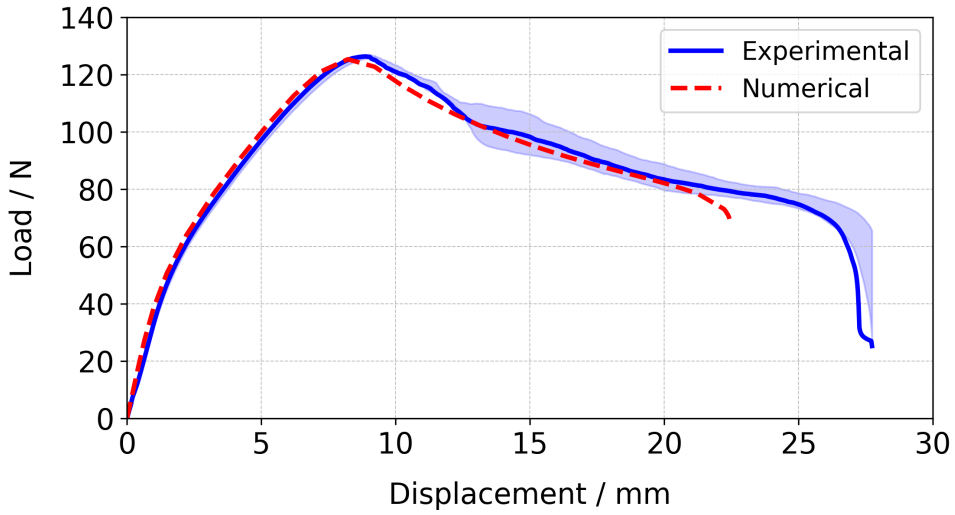


Figure 21: Comparison between experimental and numerical load-displacement curves for DCB mode I testing with adhesive A produced with vacuum condition manufacturing.

4.2 DCB mode III modelling

Given that the mode III loading of a DCB specimen involves an out-of-plane shear mode, simplifying this model to a 2D problem was not feasible. Consequently, it is crucial to use a mesh with optimal dimensions to avoid simulations with prohibitively high computational costs while still ensuring accurate results. A convergence study was conducted, and a biased local seed was utilized to achieve a more refined mesh at the interface between the acrylic and the adhesive layer. The acrylic substrates and the PC supports were modeled using CPE4R elements, whereas the adhesive was modeled using COH2D4 elements. The final mesh obtained is shown in Figure 22. A coupling interaction between the cylindrical surfaces inside the PC supports and a reference point made at their centroid was used to apply the boundary conditions. The lower support allows unrestricted movement in z direction and free rotation around the y axis. The upper support was subjected to a constant speed in the z direction of 2 mm/min.

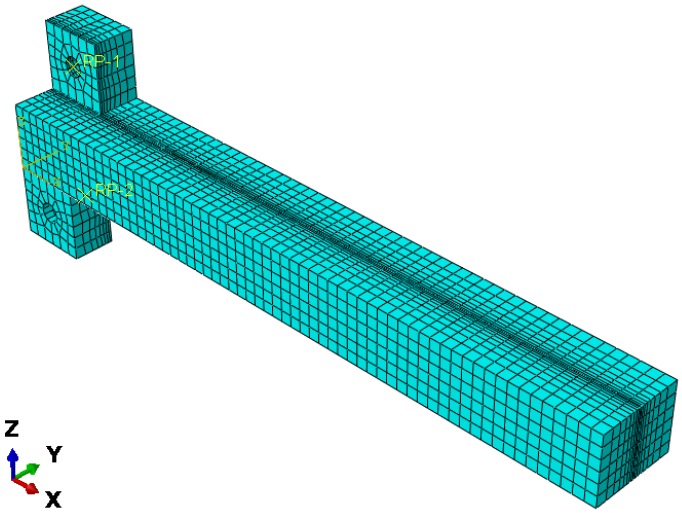


Figure 22: Mesh used in the FE model.

The cohesive law obtained in section 3.2 was used to model the behaviour of the adhesive. Given that the cohesive law has a triangular form, a bilinear law was used to input them (dashed line in Figure 18) rather than a tabular way, as was done in DCB mode I testing, to prevent noise from being introduced into the material models. The maximum stress and elastic traction stiffness defined the damage initiation, and the fracture energy values were used to model the damage evolution.

Figure 23 represents a comparison between the numerical obtained load-displacement curve with the previously obtained experimentally. Regarding the stiffness of the joint, the numerical model could predict the initial part of the curve, which, as already explained for mode I loading conditions, is mainly governed by the mechanical properties of the acrylic substrate. In relation to the zone before the maximum load point, the numerical model could accurately predict this peak value, however, the experimental results showed a little decrease in the stiffness that was not predicted by the FE model. This may occur due to defects present on the adhesive layer, that are not accounted for in the numerical model since this is an ideal scenario. Additionally, in the zone between approximately 17 and 27 mm of displacement, the experimental results showed a much more accentuated decrease in the load than the numerical outputs. Once again, this may occur since although the presence of defects was reduced using the vacuum condition manufacturing approach, we still have, as shown in Figure 3 the presence of some defects on the edge of the adhesive layer. The location of these defects can have a larger impact in a shear loading mode when compared to an opening mode, explaining why we have more significant discrepancies in the results in this scenario.

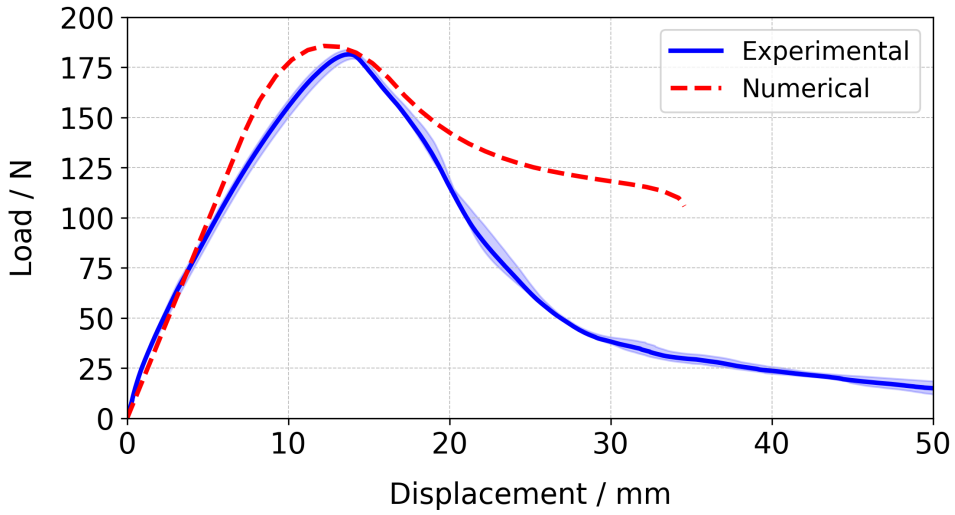


Figure 23: Comparison between experimental and numerical load-displacement curves for DCB mode III testing with adhesive A.

5 Validation in peel tests

Using the previously obtained cohesive law, directly extracted from DCB mode I tests, a different geometry was modelled to simulate adhesives A, and B. Peel specimens were manufactured using these two adhesives, and the experimental details are described by Sousa et al. [18]. The numerical model of the peel specimens was modelled on Abaqus using a 2D finite element simulation with a 10 mm out-of-plane thickness. The peel specimen consists, besides the PSA, of an acrylic substrate, modelled using an elastic material model with the properties available in Table 1 and a steel backing. A bilinear work-hardening material model was used to define the steel stress-strain curve where the elastic modulus (E), Poisson's coefficient, yield strain (ϵ_y), and slope after yielding (αE) were described. Table 2 lists the parameters of the material.

Table 2: Mechanical properties of steel 1.4310 used in the numerical simulations.

E	α	ϵ_y	Poisson's ratio
160 GPa	0.0186	0.64 %	0.28

Additionally, COH2D4 elements were used to model the adhesive and CPS4R elements to model the acrylic substrate and the steel backing. An overall mesh seed size of 0.2 mm was used. A biased local seed was employed throughout the thickness of the acrylic substrate. For the cohesive elements, a mesh with one element per thickness unit was employed. Figure 24 shows, for a 30° peel test, a global view of the mesh used as well as the boundary conditions employed.

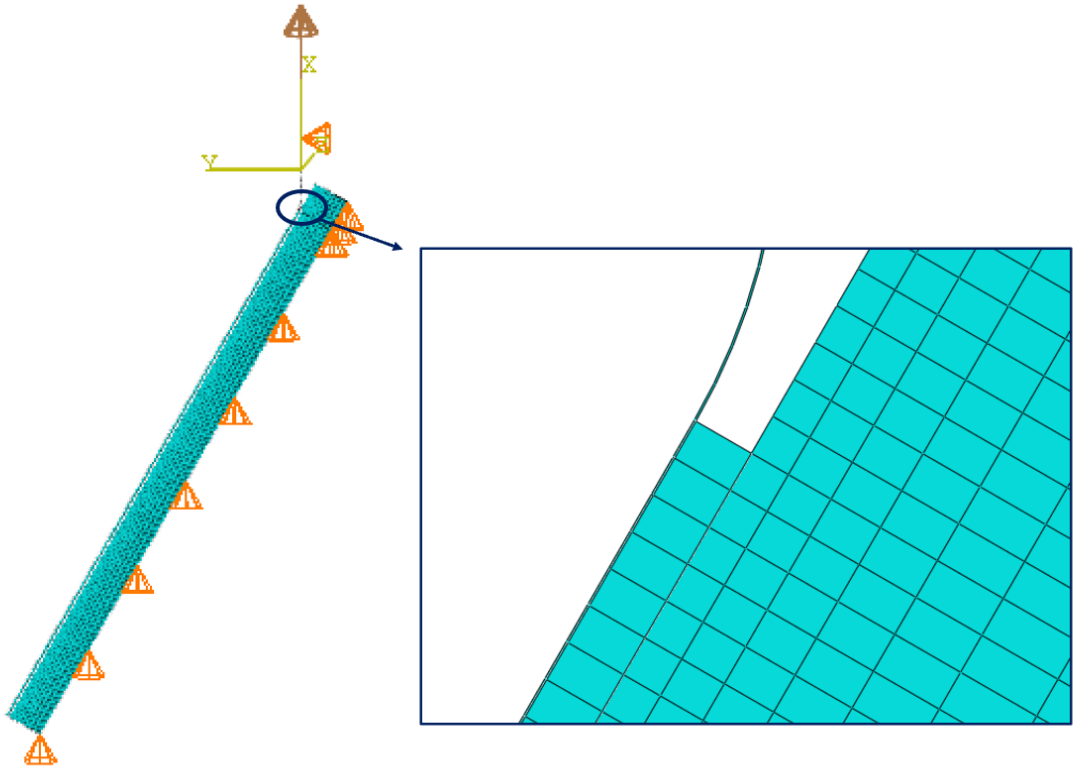


Figure 24: Schematic of the finite element model.

The experimental results were compared with two different numerical approaches. These differ in the way the cohesive law characterising the adhesive was extracted. Firstly, a methodology for obtaining a cohesive law characteristic of the joint directly from the peel results was developed. This consists of assuming that the cohesive law is approximately a triangular law. Therefore, it is assumed that during stable crack propagation, the fracture energy is maximum and constant. Thus, considering that the stresses evolve linearly from zero to the point of maximum stress, it was possible to extract this last value as well as the elasticity of the cohesive law by characterising the fracture process zone of the peel test. The detailed procedures for obtaining this law directly from the peel tests can be found in [18]. The second numerical approach consists of implementing the cohesive law obtained directly from the DCBs loaded in mode I. Only the cohesive law extracted from mode I tests was used to characterise the cohesive law, and it was assumed that all the failure modes behaved in the same way since the fracture energies between mode I and mode III are similar and according to [19] this produces differences in the results of less than 5% and allows the implementation of a simpler numerical model.

Figure 25 presents the values obtained for the average force in the plateau region for these three scenarios. The red dots show the values obtained in the experimental results (with the respective standard deviation at blue), the green triangles represent the values obtained in the numerical model with the cohesive laws extracted directly for each joint

from peel tests, and, finally, the orange crosses shows the outcomes of the FE model using the cohesive law obtained from DCB mode I loading conditions.

As can be seen in Figure 25, the numerical results obtained from the DCB cohesive law show a good agreement for the 30° peel test, with a small relative error, and a perfect outcome for the prediction of the plateau average load for 60° and 90° peel tests. For higher angles, the numerical results obtained are below from the obtained experimental results. For higher angles, the shear effects are more predominant, and, therefore, as we assume the cohesive law obtained for mode I loading conditions to be the same for all three modes, the absence of shear modes can affect these results, leading to values which are below those registered experimentally.

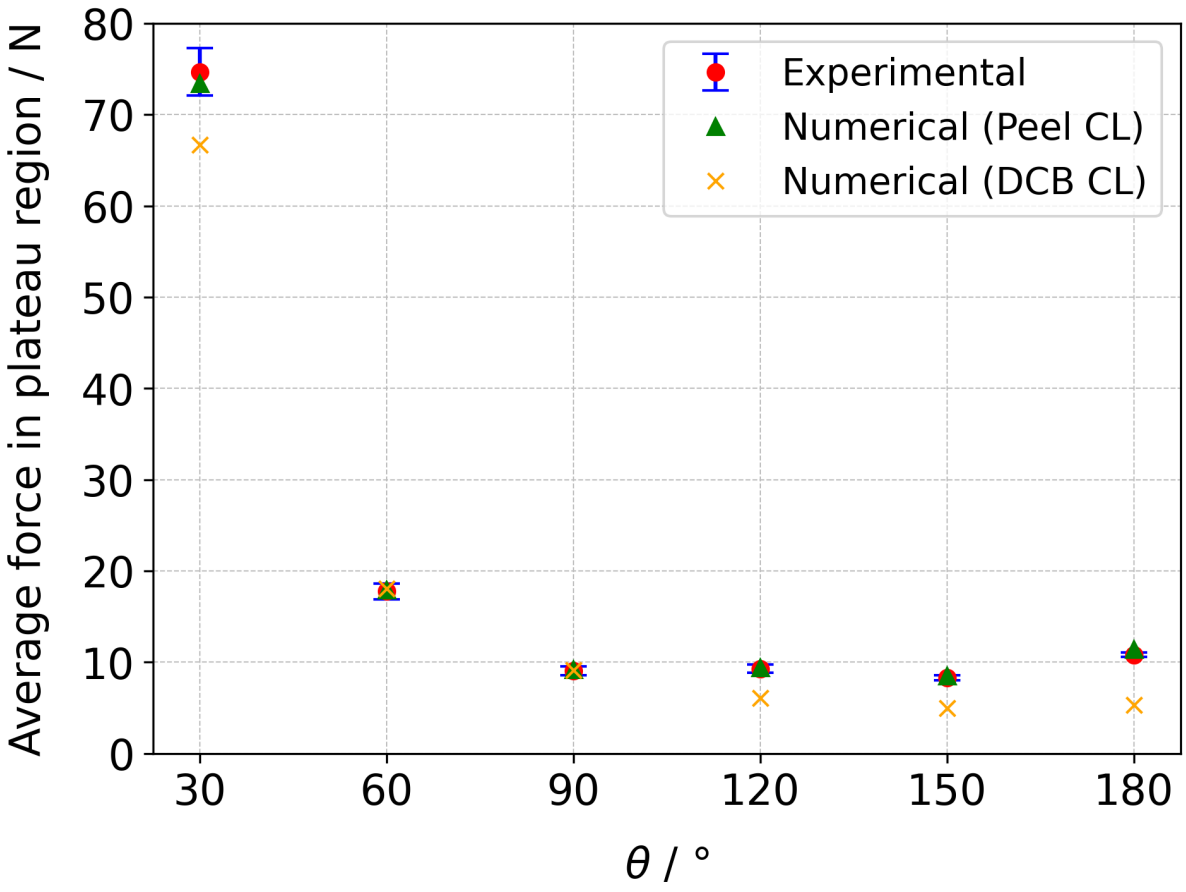


Figure 25: Comparison of the experimental vs numerical results for the average force in the plateau region of a peel test using a cohesive law obtained directly from mode I DCB tests with adhesive A.

Although the cohesive law obtained directly from peel tests provides more accurate results, the law extracted from DCBs provides very interesting results since it has been extrapolated from another geometry and applied in the same way for the different loading angles. In this way, although we lose certainty in the results, we gain flexibility since we are not restricted to applying it to the joint from which it was extracted. In addition,

although it is commonly accepted in the literature that loading modes II and III have similar energy values and are therefore assumed to be equivalent, there is no data proving the applicability of this to the adhesives under study due to the difficulty in carrying out tests in mode II. If the mode II values prove to be higher than those obtained for mode III, the results obtained in the peel tests that are lower than expected could be substantially improved since this occurs predominantly in loading situations where there is a greater force component in a direction parallel to the bonding length.

6 Conclusions

This work has characterised the behaviour of two acrylic PSAs under mode I loading conditions through detailed experimental and numerical analyses. The use of DCB tests to investigate these adhesives under mode I loading has provided critical insights into their failure mechanisms and fracture energies.

Due to the presence of entrapped air in adhesive A during the manufacturing of the DCB specimens, samples using two distinct manufacturing procedures were produced. A vacuum condition manufacturing approach was used to minimise the defects observed on the adhesive layer. The specimens were tested under mode I loading conditions, and the results of both methods were compared. The DCBs produced in a reduced air pressure environment showed less dispersion in the results, higher peak loads and higher displacements until failure.

DCBs produced with adhesive B showed a large capability of accumulating energy, causing larger areas of the adhesive layer to deform. This behaviour did not allow for smooth crack propagation, resulting in a sudden failure of large adhesive portions, creating a stair-like shape in the load-displacement curve.

The CTOD was evaluated using DIC techniques, which allowed for precise measurement of deformation and stress at the crack tip. This robust approach enabled the accurate computation of cohesive laws that are essential for describing the mechanical behaviour of the adhesives under tensile stresses.

Considering that adhesive B did not presented a stable crack propagation in the experimental tests under mode I loading conditions, only adhesive A was further studied.

To characterize the adhesive under a shear loading mode, DCB specimens were loaded under mode III conditions and the cohesive law was extracted using a similar procedure to the one previously applied to mode I tests. The fracture energy revealed similar values when compared between the opening and shear modes, however, the cohesive law obtained for mode III presented lower stresses and higher displacements at the crack tip.

A CZM was developed and integrated into numerical simulations using these experimentally derived cohesive laws. The model effectively captured the interactions at the adhesive interface, and the simulations based on these cohesive laws showed good agree-

ment with the experimental data. Adhesive A produced in a vacuum condition presented outstanding results, showing a perfect agreement between the experimental and numerical data. This concordance validates the cohesive laws' effectiveness in predicting the adhesives' failure behaviour under mode I loading conditions.

Furthermore, peel specimens were modelled in the finite element software using the previously obtained cohesive law in order to validate it for a different geometry. The results showed a good agreement for peeling angles equal to or less than 90°. For higher angles, the comparison between the experimental and numerical results showed a slight discrepancy between them. This may occur due to the material model's absence of shear data.

Future work will focus on extending these methodologies to incorporate more complex loading scenarios and environmental conditions to further validate and refine the numerical models' predictive capabilities. Implementing shear data obtained from DCB tests under mode III loading conditions can provide a more robust CZM capable of predicting the behaviour of joints under mixed-mode applications.

References

[1] Istvan Benedek and Mikhail M. Feldstein. *Technology of Pressure-Sensitive Adhesives and Products*. CRC Press, 1 edition, 2009.

[2] M. F. S. F. de Moura Filipe J. P. Chaves, L. F. M. da Silva, D. A. Dillard, and V. H. C. Esteves. Fracture mechanics tests in adhesively bonded joints: A literature review. *The Journal of Adhesion*, 90(12):955–992, 2014.

[3] Vasco Daniel Castro Pires. Study of a novel curved single lap joint concept with non-uniform adhesive thickness. Master's thesis, Department of Mechanical Engineering, Faculty of Engineering of the University of Porto, 2023.

[4] Jianping Jing, Feng Gao, Janine Johnson, Frank Z. Liang, Richard L. Williams, and Jianmin Qu. Simulation of dynamic fracture along solder–pad interfaces using a cohesive zone model. *Engineering Failure Analysis*, 16(5):1579–1586, 2009.

[5] Lucas F. M. da Silva and Raul D. S. G. Campilho. Advances in numerical modeling of adhesive joints. In *Advances in Numerical Modeling of Adhesive Joints*, pages 1–93. Springer Berlin Heidelberg, Berlin, Heidelberg, 2012.

[6] J. R. Rice. A Path Independent Integral and the Approximate Analysis of Strain Concentration by Notches and Cracks. *Journal of Applied Mechanics*, 35(2):379–386, June 1968.

[7] The force on an elastic singularity. *Philosophical Transactions of the Royal Society of London. Series A, Mathematical and Physical Sciences*, 244(877):87–112, November 1951.

[8] A. Wells. Unstable crack propagation in metals: cleavage and fast fracture. In *Proceedings of the crack propagation symposium*, number 84, page 26028, 1961.

[9] Q. Yang and M. Thouless. Mixed-mode fracture analyses of plastically-deforming adhesive joints. *International Journal of Fracture*, 110:175–187, 2001.

[10] U. Stigh, K. S. Alfredsson, T. Andersson, et al. Some aspects of cohesive models and modelling with special application to strength of adhesive layers. *International Journal of Fracture*, 165:149–162, 2010.

[11] P. Olsson and U. Stigh. On the determination of the constitutive properties of thin interphase layers - an exact inverse solution. *International Journal of Fracture*, 41:R71–R76, 1989.

[12] F. Sun and B.R.K. Blackman. A dic method to determine the mode i energy release rate g, the j-integral and the traction-separation law simultaneously for adhesive joints. *Engineering Fracture Mechanics*, 234:107097, 2020.

[13] A. Biel and U. Stigh. Cohesive zone modelling of nucleation, growth and coalesce of cavities. *International Journal of Fracture*, 204(2):159–174, April 2017.

[14] Ulf Stigh, Anders Biel, and Daniel Svensson. Cohesive zone modelling and the fracture process of structural tape. *Procedia Structural Integrity*, 2:235–244, 2016.

[15] IIT library. 6.777j/2.751j material property database. `https://yourlibrary.iit.edu/material_property_database`, 2024. Accessed: 2024-02-27.

[16] Beatriz D. Simões, Eduardo A. S. Marques, Ricardo J. C. Carbas, Steven Maul, P. Stihler, Philipp Weißgraeber, and Lucas F. M. da Silva. Rheological and mechanical properties of an acrylic psa. *Polymers*, 15(18), 2023.

[17] Tetsuo Yamaguchi, Hiroyuki Muroo, Yutaka Sumino, and Masao Doi. Asymmetry-symmetry transition of double-sided adhesive tapes. *Phys. Rev. E*, 85:061802, Jun 2012.

[18] Hugo C. Sousa, Beatriz D. Simões, Eduardo A.S. Marques, Ricardo J.C. Carbas, Steven Maul, Patrick Stihler, Philipp Weißgraeber and Lucas F.M. Silva. Experimental and numerical characterisation of the interface fracture behaviour of PSAs with peel tests. *In preparation*, 2024.

[19] I.K. Mohammed, M.N. Charalambides, and A.J. Kinloch. Modelling the interfacial peeling of pressure-sensitive adhesives. *Journal of Non-Newtonian Fluid Mechanics*, 222:141–150, August 2015.

Appendix B

Paper 2 - Experimental and numerical characterisation of the interface fracture behaviour of PSAs with peel tests

Experimental and numerical characterisation of the interface fracture behaviour of PSAs with peel tests

Hugo C. Sousa[1], Beatriz D. Simões[1], Eduardo A.S. Marques[2], Ricardo J.C. Carbas[1], Steven Maul[3], Patrick Stihler[3], Philipp Weißgraeber[4] and Lucas F.M. Silva[2]

1 Institute of Science and Innovation in Mechanical and Industrial Engineering (INEGI), Rua Dr. Roberto Frias, 4200-465 Porto, Portugal

2 Department of Mechanical Engineering, Faculty of Engineering, University of Porto, Rua Dr. Roberto Frias, 4200-465 Porto, Portugal

3 Robert Bosch GmbH, Corporate Research and Advance Engineering, 71272 Renningen, Germany

4 Faculty of Mechanical Engineering and Marine Technology, University of Rostock, 18059 Rostock, Germany

Abstract: In this study, the failure mode of two double-sided acrylic pressure-sensitive adhesives (PSAs) was studied using peel tests. In addition to the PSAs, the peel specimens are composed of a steel backing membrane and an acrylic adherent. This paper starts by deriving quantitative expressions to establish the true adhesive fracture energy independent of the peel test geometry. The full envelope of the force distribution in the process zone is determined, and a cohesive zone law is derived based on the fracture process zone height obtained using digital image processing. Finally, a cohesive zone model is developed, and the numerical results are compared to the experimental ones. A stress analysis is performed along the adhesive layer for the different testing conditions to understand the failure mechanisms obtained experimentally.

Keywords: Adhesive joints, Pressure-sensitive adhesives, Peel test, Adhesion energy

1 Introduction

The industry is currently facing various challenges, including the need for increased productivity, a decrease in energy consumption, and the consolidation of more environmentally friendly processes. One method to lower pollution emissions to the ecosystem is the application of more lightweight and effective materials [1–3].

In this context, pressure-sensitive adhesives (PSAs) have emerged as a pivotal solution within engineering and biomedical fields [4–6]. Due to their inherent flexibility, lightweight properties, and rapid bonding capabilities with diverse materials, PSAs facilitate the construction of lighter and more efficient assemblies, thereby contributing directly to environmental sustainability and resource efficiency.

The peel test, commonly utilised in the packaging and electronic industries to assess the failure of flexible laminates, has been the subject of extensive research, exploring numerous parameters such as peel angle, material thickness, intrinsic adhesion, and the impact of test rates and temperatures [7, 8], also accounting for the tensile deformation of the peeling arm, which could affect the energy available for debonding [9]. Kinloch et al. [10, 11] have focused on identifying a characteristic parameter of the adhesive's peeling behaviour that remains constant regardless of the test's geometric specifics.

The modelling of the peeling process, especially within the context of adhesive bonds, requires sophisticated simulation techniques to predict fracture behaviours accurately. Several notable studies have utilised the cohesive zone model (CZM) to analyse the fracture mechanics of fibre composites and adhesively bonded joints. Blackman et al. [12] provide a study on the use of CZM, demonstrating its applicability in evaluating the fracture of such materials. Further analytical explorations by Williams and Hadavinia [13] have offered solutions that enhance the understanding of CZM, enabling more accurate predictions of adhesive behaviour under stress.

Diehl [14] focuses on studying inelastic peeling scenarios using a penalty-based cohesive-zone finite element approach. This is complemented by Martiny et al. [15], who employ a multilevel finite element approach to dissect the energy contributions in peel tests, providing deeper insights into the dynamics at play during the peeling process. Wei and Hutchinson [16] examine the interplay between peel force, interface strength and work of adhesion, taking into account the plastic deformation in the adhesive film. Hadavinia et al. [17] further this by numerically analysing the elastic-plastic behaviour in peel tests, using the virtual crack closure technique as the failure mechanism. Finally, Sauer's [18] work on enriched contact finite elements through an XFEM model highlights the advancements in computational methods for stable peeling computations, reflecting significant progress in the field of numerical methods in engineering.

In this work, we explore the peeling of PSA, with a focus on the energy dissipation due to the plastic bending of the peeling arm. The goal is to derive quantitative expressions from adjusting the measured peel force for energy losses. This method aims to establish a true adhesive fracture energy that is independent of the peel test's geometry. Afterwards, a detailed analysis and characterisation of the peel-front process zone are elaborated to derive a cohesive law. Finally, a numerical model is implemented to validate the obtained cohesive law.

1.1 Adhesion energy

The determination of adhesive fracture energy, G_a, utilises an energy balance approach, calculated as:

$$G_a = \frac{1}{b}\left(\frac{dU_{\text{ext}}}{da} - \frac{dU_s}{da} - \frac{dU_{dt}}{da} - \frac{dU_{db}}{da}\right) \tag{1}$$

where dU_{ext} is the external work, dU_s the stored strain energy in the peeling arm, dU_{dt} the energy lost during tensile deformation, and dU_{db} the energy dissipated from plastic bending at the peel front. G_a is a key parameter, reflecting both the interfacial bonding energy and the localised dissipation of energy [10].

An inextensible backing can be bonded to the peeling arm to lessen elastic deformation during peel tests and enhance the hypothesis that the work potential energy is driving the separation [9,19]. Considering a peeling test with an arm of thickness h and width b, under a load P at peel angle θ, and assuming the arm behaves as an infinitely rigid body, the adhesive fracture energy simplifies to:

$$G_a^{\infty} = \frac{P}{b}(1 - \cos\theta) \tag{2}$$

Nevertheless, if we consider the effects of the extensibility of the peel arm, the external work can be described by:

$$dU_{\text{ext}} = Pda(1 + \epsilon_a - \cos\theta) \tag{3}$$

where ϵ_a is the tensile strain in the arm.

Therefore, we obtain the value of G_a for the non-linear extension of the peel arm, but where bending dissipation is low or only elastic bending (G_{eb}) is intended to occur:

$$G_a^{\text{eb}} = \frac{P}{b}(1 + \epsilon_a - \cos\theta) - h\int_0^{\epsilon_a} \sigma\, d\epsilon \tag{4}$$

The maximum elastic energy in the peel arm per unit width and length, not accounting for work hardening, can be calculated as :

$$G_{\text{max}}^{e} = \frac{1}{2}(\sigma_y \epsilon_y h) = \frac{1}{2}(E\epsilon_y^2 h) \tag{5}$$

where ϵ_y is the yield strain and E is the Young's modulus of the peeling arm.

Plasticity effects

If plastic or viscoelastic bending of the peel arm occurs near the crack front, the determination of the critical energy release rate, G_c, must also account for such energy losses [19]. Has Gent and Hamed have demonstrated, considering these energy losses is necessary to ensure accuracy in calculating the energy required to propagate a crack [20–22]. The total work performed by external forces can be described by subtracting the energy lost due to the plastic deformation of the backing substrate, denoted by G_{db}, from the previously obtained G_a^{eb}. The fracture energy of the system, accounting for the plastic dissipation through bending can be expressed as:

$$G_a = G_a^{\text{eb}} - G_{\text{db}} \tag{6}$$

An iterative method, which accounts for various loading states, including elastic recovery during unbending and both plastic bending and unbending, is employed to calculate the energy dissipated due to plastic bending. The appendix in [10] provides a comprehensive description of this calculation methodology. The iterative calculation of G_{db} uses as inputs the material and geometric properties of the peel arm (used to calculate, according to Equation 5, the maximum elastic energy that the peel arm can store) and the fracture energy of the system assuming that the adhesive behaves as a rigid body (Equation 2).

1.2 Traction separation law

The cohesive zone model CZM is an appropriate approach to explaining the cohesive failure of the adhesive layer. It can explain the nonlinear behaviour of the material at a large deformation scale [23, 24] and can be expanded to take into account the viscoelastic feature using various methods, including the incorporation of rheological models [25, 26].

In peel tests, the CZM is particularly valuable as it provides a realistic depiction of the adhesive interactions and failure processes at the peel front. Unlike traditional fracture mechanics, which may fail to account for the complex interactions in adhesive layers, the cohesive zone law introduces a tractable way to model the progressive damage and separation of adhesive bonds under peel forces. It defines the relationship between the traction forces and the separation displacement, effectively capturing the essential behaviour of adhesive materials as they undergo deformation and failure.

The cohesive zone law is defined primarily by two parameters: the peak stress, σ_{max}, and the critical crack tip opening displacement (CTOD), δ_c. This last parameter is particularly significant as it designates the point just ahead of the crack tip where the material's cohesive forces are unable to sustain any further stress, thus leading to the separation of the material.

In a CZM, the fracture or adhesion energy, denoted as G, represents the energy required to fully separate an interface. This critical parameter is quantified by the integral under the cohesive law curve, which describes the relationship between stress and the CTOD. The relationship can be mathematically expressed as:

$$G = \int_0^{\delta_c} \sigma(\delta), d\delta \tag{7}$$

where $\sigma(\delta)$ is the stress as a function of the opening displacement at the crack tip, detailing how stress varies with increasing separation until complete disengagement.

Further, the peak stress within the cohesive zone can be conceptualised as the maximum stress that the material can withstand before initiating a crack propagation. Considering the use of a bilinear law to define the behaviour of the cohesive element, σ_{max} can be calculated from the total fracture energy divided by the CTOD at which this peak stress occurs:

$$\sigma_{max} = \frac{G}{\delta_c} \tag{8}$$

In this context, δ_c refers specifically to the height of the fracture process zone from which the crack stably propagates.

Assuming that when the adhesive reaches maximum stress is when the load-displacement curve reaches the plateau, the stiffness of the CZM can be obtained as:

$$K = \frac{\sigma_{max}}{\delta_c} \tag{9}$$

2 Experimental details

2.1 Materials

In this work, two distinct double-sided acrylic PSAs were investigated:

- Adhesive A, made of a highly shock-absorbing black acrylic foam.
- Adhesive B, made of grey foam acrylic.

The main mechanical properties of these two adhesives were provided by the manufacturers, and they are summarised in Table 1.

Table 1: General properties of PSAs used.

Adhesive	A	B
Poisson's ratio	0.499	0.499
Thickness [mm]	0.3	1.1

The peel specimens consist of, alongside the adhesives, a PMMA substrate and a calibrated backing tape produced by Helios-Preisser (Gammertingen, Germany) and made from 1.4310 steel. The mechanical properties of the PMMA and the steel tape are summarised in Tables 2 and 3, respectively.

Table 2: Mechanical properties of PMMA [27].

Density	Young's modulus	Poisson's ratio
1200 kg/m^3	1.8 - 3.2 GPa	0.35 - 0.4

Table 3: Mechanical properties of steel 1.4310.

Density	Young's modulus	Poisson's ratio
7900 kg/m^3	160 GPa	0.28

2.2 Specimen manufacturing

Using a scalpel, the adhesive samples were cut to 100 mm long by 10 mm wide sheets. The bond length between the acrylic and the adhesive is 50 mm. Before bonding the PSAs to the acrylics, calibrated steel backing tape, 0.01 mm thick and 12.7 mm wide, was applied.

Figure 1 presents the peel specimen where the grey line illustrates the steel backing (the thickness is not represented in scale).

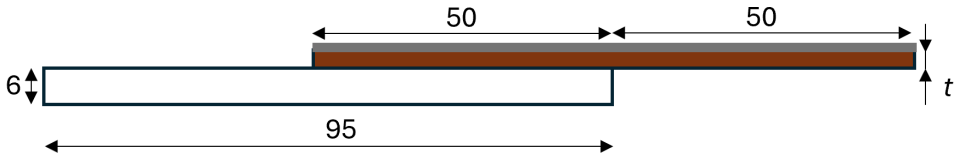


Figure 1: Peel specimen configuration, in mm.

Finally, all the specimens were assembled in a mould, each joint under 23 kPa, for 72 hours before testing.

2.3 Testing procedure

The peel tests were performed using a quasi-static machine, INSTRON® 3367 (Illinois ToolWorks, Hopkinton, Massachusetts, USA) at a loading rate of 2 mm/min. The forces and displacements were measured using a 1kN load cell, and data were collected at a rate of 5 points per second. For each combination of adhesive and peeling angle, at least three tests were performed.

To carry out the experiments, a setup that restricts the specimen only vertically was needed. This setup (Figure 2) consists of two aluminium lateral supports (1) that hold the polished steel bars (2) in place to reduce friction between them and the bearings (3) on which a base (4) is mounted. There is a slot in this base where a table (5) can be attached. This allows for an easy change between tables with different inclinations, allowing the peel angle at which the tests are conducted to be adjusted. In addition, a cable (7) and pulley (6) system were employed to guarantee that the table followed the tape's peeling in order to maintain the test's alignment over time. For this, a pre-stretched stainless steel cable with a diameter of 1.5 mm was used. Therefore, any elastic deformations in the rope can be considered negligible, considering steel has a significantly higher rigidity when

compared to PSAs. This cable is attached to the moving table, passes through the pulley and is fixed again to a long, rigid pin (8) that is fixed to the top of the load cell (9) of the uniaxial testing machine. In this way, we ensure that when we have a vertical displacement of the grip that pulls the tape, we will have a displacement with the same magnitude in the table. The force required to move the table will not be recorded by the load cell since the pin that pulls the rope is fixed at a higher level than the load cell.

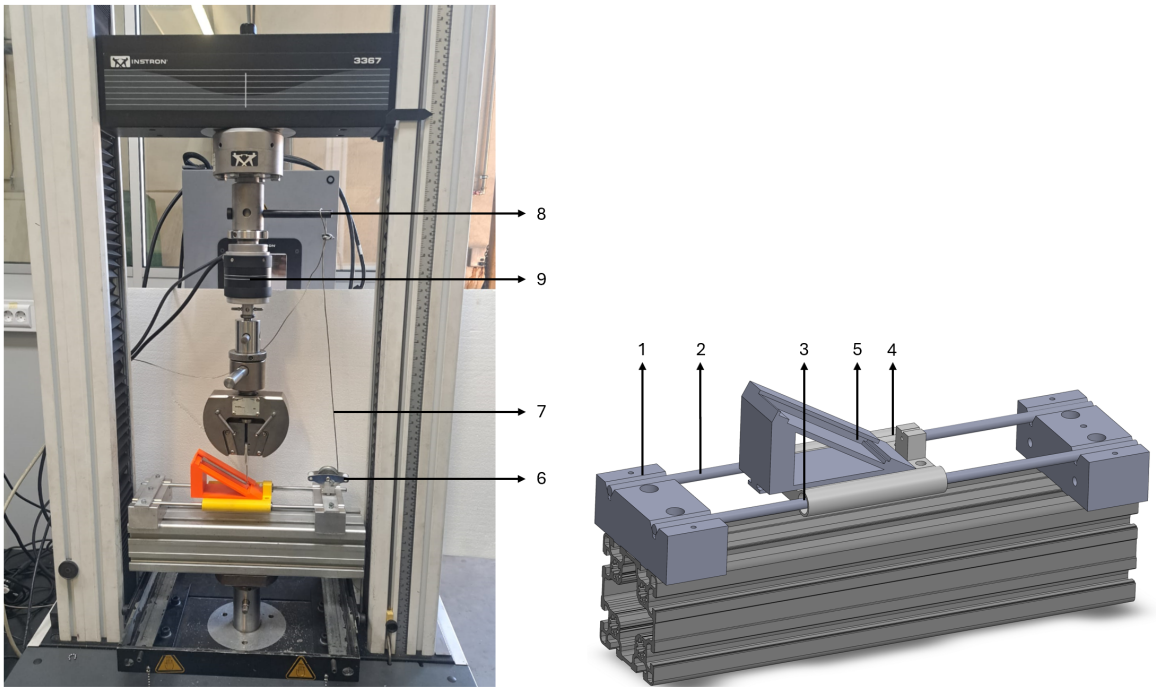


Figure 2: Test setup attached to the testing machine (left). CAD model of the test setup (right).

The images recorded during tests were obtained using a digital camera (Nikon D5300) equipped with a Nikon AF-P NIKKOR 18-55mm f/3 lens. The camera was positioned in front of the specimens, and a laser beam leveler was used to ensure that the lens plane was perpendicular to the observation surface.

3 Numerical details

Peel tests were modelled using finite element (FE) software, ABAQUS®, by performing a 2D FE simulation with a 10 mm out-of-plane thickness. The adhesive was modelled using bilinear quadrilateral cohesive elements (COH2D4), and the remaining parts were modelled as 4-node two-dimensional plane strain elements with reduced integration (CPE4). A convergence study was conducted to ensure that the mesh size correctly predicted the behaviour of the adhesive without unnecessarily increasing the computation time. An overall mesh seed size of 0.2 mm was used. For cohesive elements, a mesh size

of one element per unit thickness was employed. Figure 3 shows, for a 30° peel test, the mesh size used, as well as the boundary conditions employed.

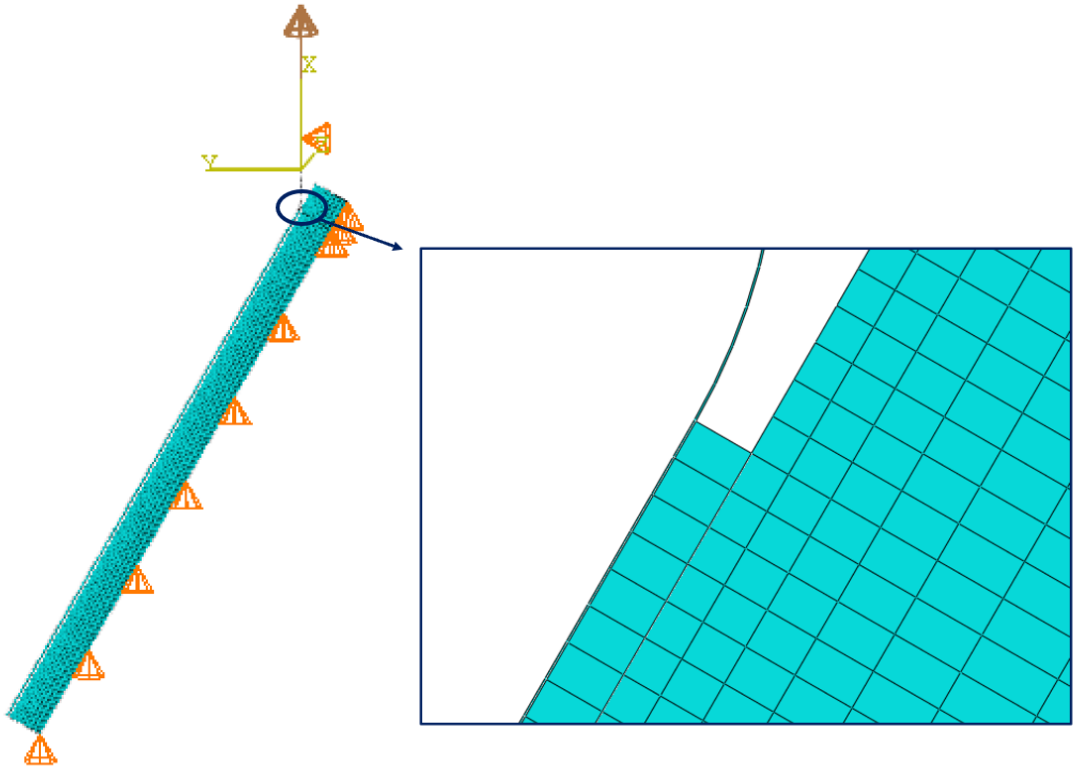


Figure 3: Schematic of the finite element model.

The acrylic substrate was modelled using an elastic material model, whose properties were detailed in Table 2. The steel stress-strain curve was defined as a bilinear work-hardening material model, where the elastic modulus (E), Poisson's coefficient, yield strain (ϵ_y), and slope after yielding (αE) were described. The material parameters are given in Table 4.

Table 4: Mechanical properties of steel 1.4310 used in the numerical simulations.

E	α	ϵ_y	Poisson's ratio
160 GPa	0.0186	0.64 %	0.28

A triangular traction separation law with a linear damage evolution was used to define the behaviour of the cohesive elements. The peak stress was obtained according to Equation 8, and the damage evolution zone was characterised using the fracture energy calculated from Equation 2. It was not considered the dissipation mechanisms that occur in the steel tape when calculating the fracture energy of the adhesive, since it was assumed that ABAQUS already accounts for this in the elastic-plastic material model that

was employed. The stiffness of the adhesive was considered as linear and was extracted according to Equation 9. For the 180° peel test, considering that in this condition, the specimen is being loaded in a direction parallel to its length, for calculating the stiffness and the maximum stress, was used the length of the FPZ instead of the height.

4 Results and discussion

4.1 Experimental results

The curves obtained from the peel test experiments are reported in Figures 4 and 5 for adhesives A and B, respectively. The peel length was defined through a trigonometric relation between the direction of the applied force and the peel direction, expressed as:

$$u = u_{pd}(1 - cos\theta) \tag{10}$$

where u is the displacement measured by the traction machine, u_{pd} is the displacement in the peeling direction and θ is the peeling angle. For the 180° peel test, it was assumed that $u = u_{pd}$, since for this condition there is no displacement of the base.

The force values at the plateau were analysed at an interval of 5 mm after the curve reached this level. This is because, due to limitations of the apparatus, for peeling angles different from 90°, the speed of displacement of the base required to follow the peeling movement is not exactly 2 mm/min. This means that, over time, the force in steady-state propagation will increase slightly due to a small increase in the actual degree of peel. This effect is reported in [28] by Kovalchick, where it is concluded that this will translate into a maximum error of, approximately, 1° inclination in the steady state peel force curve. Therefore, it was decided to limit the length of the plateau under analysis to minimise this effect.

By analysing the obtained curves, it is clear that both adhesives present a higher value of force for the lower angle (30°). The force decreases from there, showing a minimum at around 150°. Between 120° and 150°, the force remains approximately constant, and then, finally, we have a small increase at the 180° peeling. These results are consistent with previous studies [11, 29]. For 90°, adhesives A and B presented different behaviours. While in adhesive A the 90° peel curve presented similar load values as the 120° and 150°, on the other hand, adhesive B, showed much higher forces for the 90° when compared to higher peeling angles. Additionally, while for adhesive A, all the forces reach a steady plateau, for adhesive B, the specimens presented a sudden abrupt failure for lower angles (30° and 60°). This behaviour was extensively analyzed in the research conducted by Sugizaki et al. [30], focusing on the various factors that determine whether a peel test achieves a steady state. Their study delves into the dynamics of peel testing, exploring how different conditions and material properties influence the outcomes and consistency

of the peel tests. According to this, sudden failure in the interface is more likely to happen at lower angles, with thicker adhesives and higher peel velocities. These results will be further discussed with support of the numerical results.

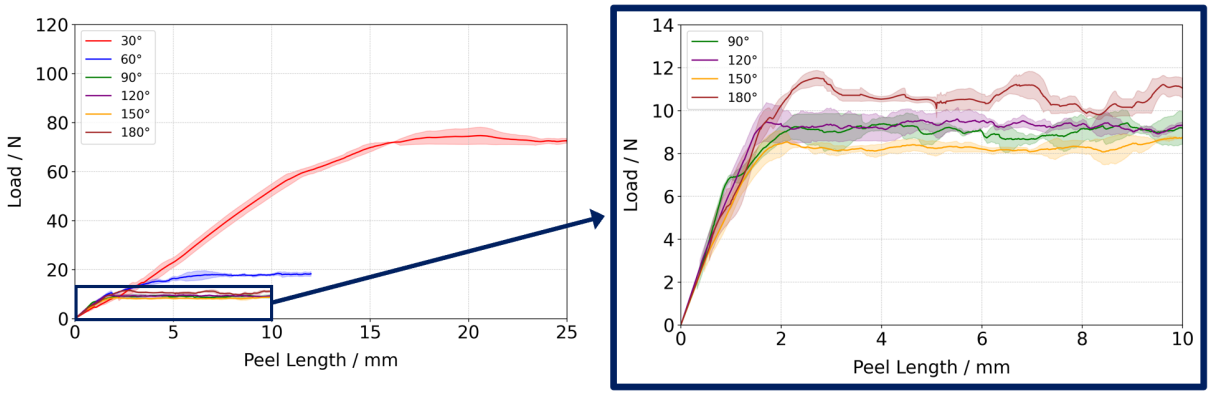


Figure 4: Peel curves for adhesive A (The solid lines and the shadowed areas represent the average curves and the standard deviations, respectively).

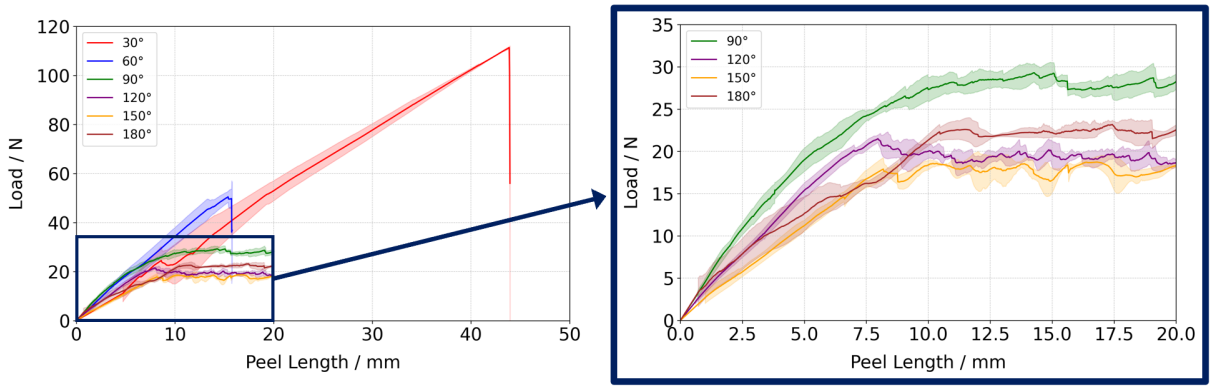
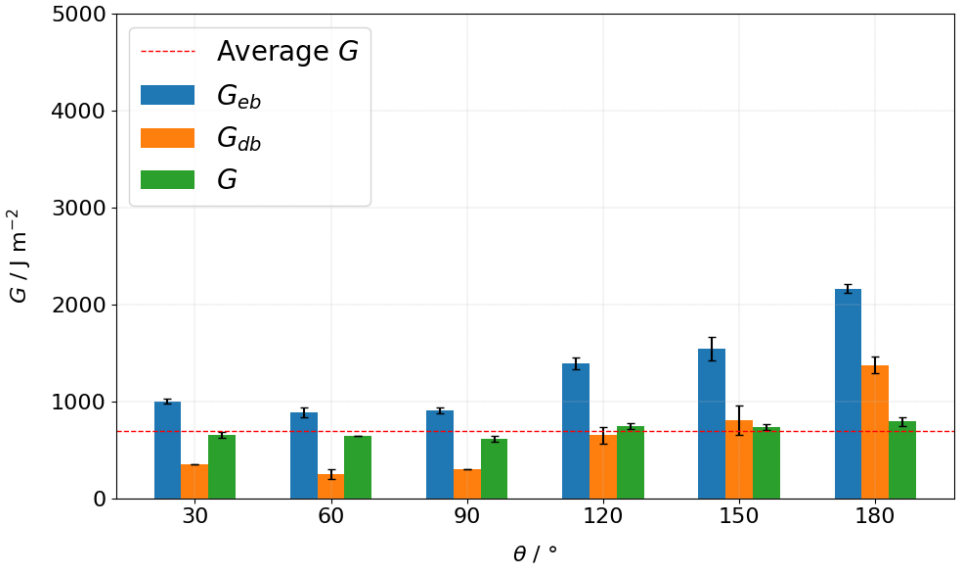


Figure 5: Peel curves for adhesive B (The solid lines and the shadowed areas represent the average curves and the standard deviations, respectively).

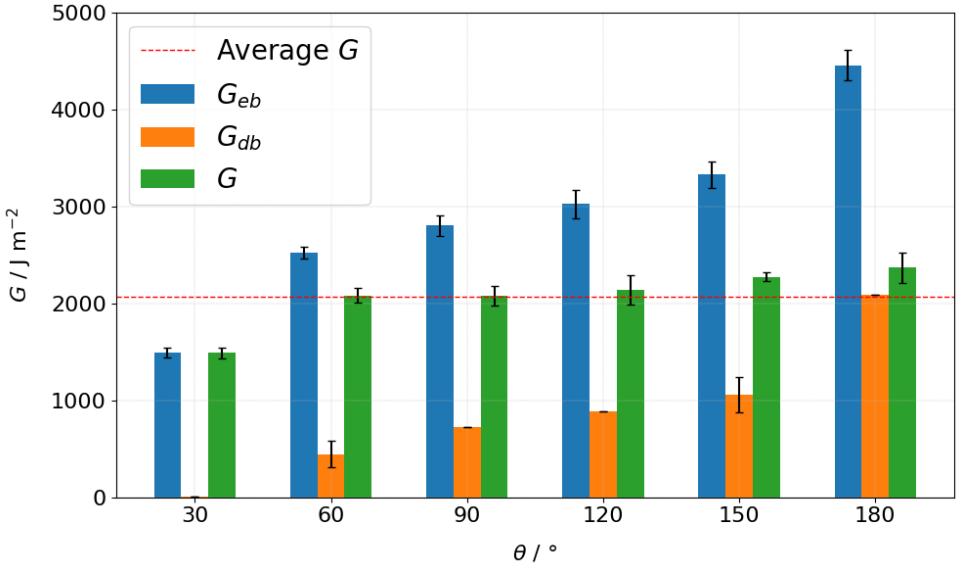
4.2 Adhesion energy

The fracture energy was calculated using an analytical peeling model developed by Kinloch et al. [10, 11], as detailed in Section 1.1. To characterise the peel arm, the steel backing properties, presented in Table 3 were considered. Figure 6 presents, for both adhesives, the work done by external forces where, in the blue bars, only elastic bending is considered (Equation 4). Furthermore, the energy dissipated due to the plastic bending of the peel arm is presented by the orange bars, and, finally, the true fracture energy (green) corresponds to the difference between these two components (Equation 6). In an extreme case, where we would have a peel angle of 0°, the energy dissipation due to plastic bending would be zero, and we would only take into account the effects due to the tensile

deformation of the material. As it can be seen, in accordance with the literature [10,19,31], for higher peeling angles, we have bigger values for the energy dissipated due to plastic bending.



(a) Adhesive A



(b) Adhesive B

Figure 6: Adhesion energy considering solely elastic bending (G_{eb}), energy dissipated due to plastic bending (G_{db}), and true adhesive fracture energy (G_a) for different peel angles.

Adhesive A presented an average fracture energy of 696 J/m^2 and the results obtained showed an overall good agreement with the theoretically expected values. Nevertheless, the result obtained for the 30° peeling test is slightly higher than expected, since it is assumed that at lower angles the plastic energy dissipated in bending is lower. However, this value is probably the result of a mathematical inaccuracy since the analytical model

implemented is highly dependent on the values obtained for G_{eb}, which can sometimes lead to imprecise values.

Adhesive B had an average fracture energy of 2069 J/m^2 and, except for the result for the 30° peel test, the obtained adhesion energies presented good agreement. For this specific case, it was expected that the value obtained would be below expectations since the analysis carried out assumes that the force values used are obtained after the crack has reached a stable propagation, which was not the case. Therefore, the value obtained for the 30° peel test is an outlier derived from the large capability of adhesive B of accumulating energy, creating large deformations areas, and, consequently, abrupt failures. This point will be discussed later with support of the numerical results. Overall, we can conclude that the values of G_a obtained are not significantly dependent on the peel angle used when accounting for plastic deformation of the peel arm.

Furthermore, it is essential to consider that although increasing the thickness of the peel arm generally leads to greater energy absorption due to the higher material volume resisting the peel forces, this relationship does not scale indefinitely. As indicated by [12, 20], once the peel arm reaches a certain thickness, the material's inherent stiffness may reduce its flexibility significantly. This reduction in flexibility limits the material's ability to bend elastically under stress, thus reducing the energy absorbed through bending deformations.

In cases where the peel arm is sufficiently thick, the dominant mechanism of energy dissipation may shift from bending to other modes, such as interfacial adhesion or cohesive failure within the adhesive layer itself. This transition in the dominant mechanism of energy dissipation may explain the stabilisation or small increase in G_{db} values at larger thicknesses. Both adhesives exhibited trends consistent with the literature [10, 19], since, although adhesive B is almost 4 times thicker than adhesive A, this increase in the peel arm did not lead to significant increases in the energy dissipated by the steel backing.

4.3 Fracture process zone characterisation

In the study of fracture mechanics within adhesive bonds, understanding the characteristics of the fracture process zone (FPZ) is pivotal. This region, where the material undergoes significant deformation prior to and during fracture, plays a crucial role in dictating the overall fracture behaviour of the material system. The FPZ's length (L) and height (δ), represented in Figure 7 for 90° peel tests, are indicative of the material's response to stress. Accurate measurement of these parameters is essential for validating theoretical models and optimising material formulations. In this subsection, we discuss the methodologies employed to measure the process zone dimensions, L and δ, using digital image analysis techniques implemented via a Python script. The code used the thickness of the acrylic substrate (6 mm) as a reference to determine the scaling factor in

units of mm/pixel.

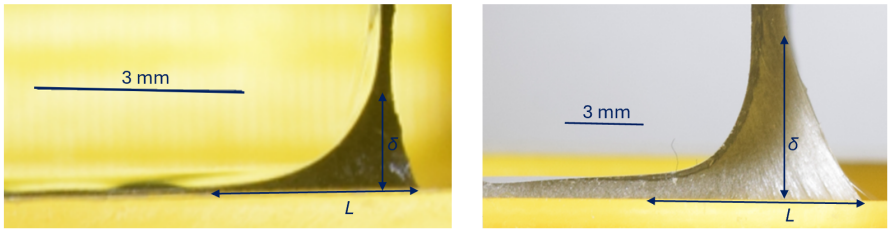
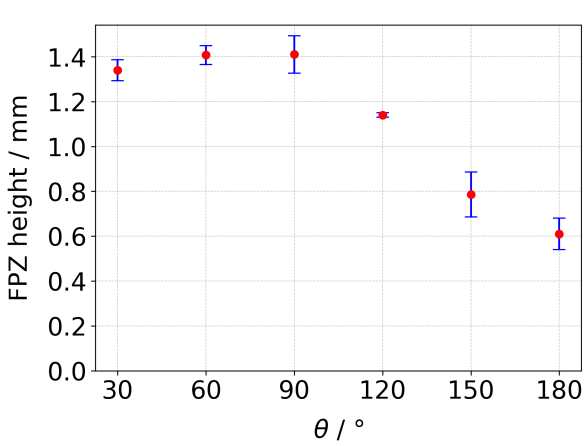


Figure 7: Image of the FPZ for adhesive A (left) and adhesive B (right) for 90º peel test.

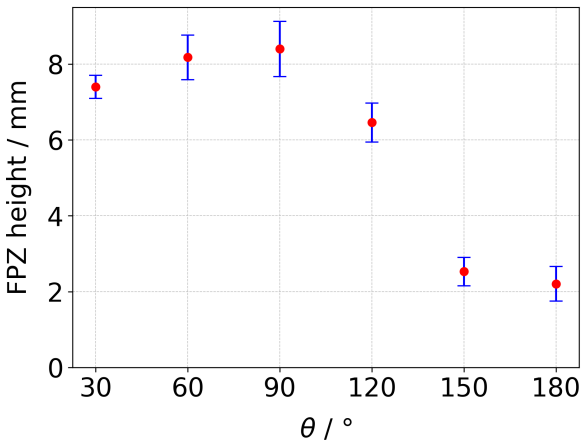
As depicted in Figure 8, both adhesives A and B exhibit similar trends in the FPZ characteristics, namely the height (see Figures 8a and 8b) and the length L (see Figures 8c and 8d). Notably, the maximum height of the process zone is observed during the 90° peel tests, which aligns with expectations since this angle predominantly induces mode I loading on the specimens [32–34].

Upon reducing the peel angle from 90° to 30°, the process zone's length increases noticeably, and its height decreases correspondingly. This behaviour is attributed to a stress distribution over a longer area since the peel force is applied in a direction more parallel to the adhesive-substrate interface, which permits significant elongation of PSA before ultimate failure occurs. In opposition, at lower angles, the component of the peel force acting perpendicular to the adhesive layer is smaller, resulting in a smaller height of the FPZ.

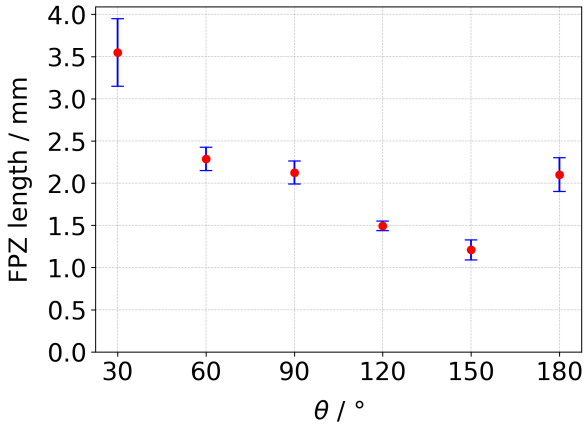
Conversely, at larger angles, specifically between 120° and 150°, cleavage becomes the prevailing failure mechanism. This results in lower overall loads being sufficient to cause failure of the PSA, which is reflected in the minimal values observed for both L and δ, when compared to lower angles. When the peel angle reaches 180°, the direction of the peeling aligns with the orientation of the specimen, enhancing the shear forces exerted. Consequently, this orientation leads to an elongation of the process zone. The observed slight increase in the average force on the plateau for these angles can be attributed to the increased shear forces, which necessitate greater energy dissipation before failure.



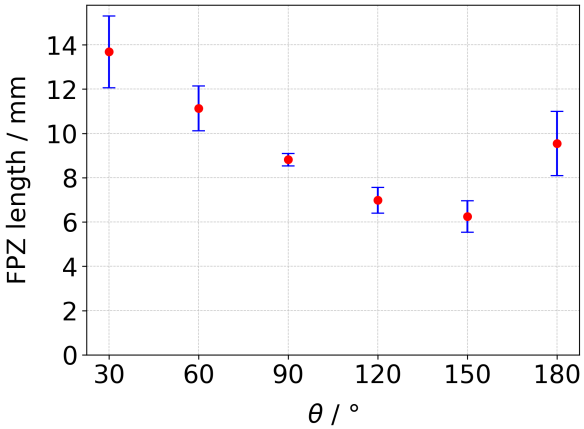
(a) δ - Adhesive A



(b) δ - Adhesive B



(c) L - Adhesive A



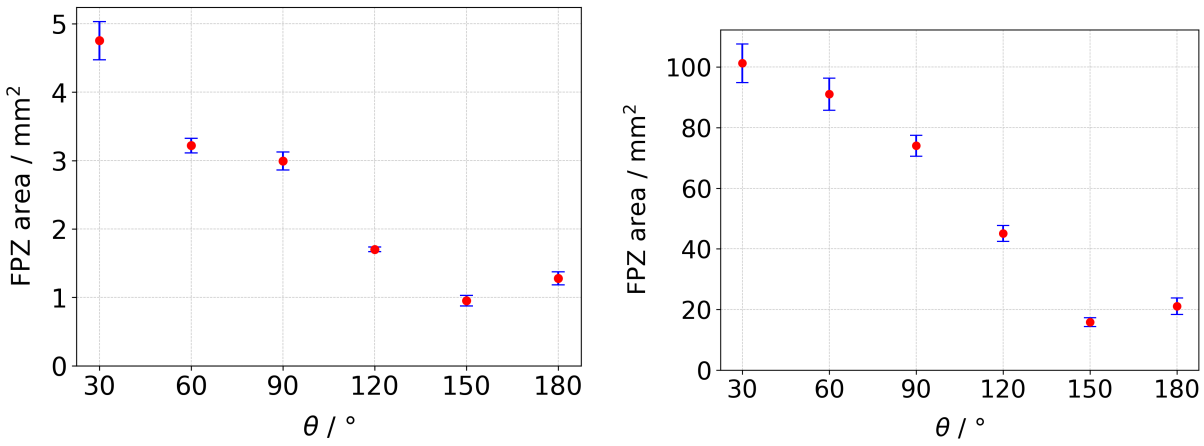
(d) L - Adhesive B

Figure 8: FPZ height (top) and length (bottom) as a function of peel angle.

Additionally, the areas of the FPZ were estimated. These were considered to have approximately a geometric form of a triangle with base L and height δ. For each condition the area was calculated using the average values of these two previously mentioned parameters and the standard deviation of the FPZ area was estimated using the following mathematical formulation:

$$\sigma_A = \frac{1}{2}\sqrt{(\delta \cdot \sigma_L)^2 + (L \cdot \sigma_\delta)^2} \tag{11}$$

where, σ_A, σ_L and σ_δ are the standard deviation of the area, length and height of the FPZ, respectively.



(a) Adhesive A

(b) Adhesive B

Figure 9: Approximate area of the FPZ as a function of the peel angle.

Considering the results obtained for both adhesives, presented in Figure 9, it is clear that the area of the FPZ is related to the values obtained for the force sustained by the joint during stable crack propagation. In a general way, large deformed areas, mean a higher capability of the joint to absorb energy before failure occurs, consequently leading to a greater load-bearing capacity. Furthermore, despite both adhesives presenting a similar trend in the area evolution in function of the peeling angle, the deformations on adhesive B extend for much larger areas, highlighting the capability of this adhesive to sustain higher loads.

4.4 Numerical results

The numerical curves for adhesives A and B were extracted from Abaqus, and compared to the experimental data (Figures 10 and 11, respectively). Considering that a 3 mm radius of curvature was applied to the steel tape in the FE model, in order to avoid sharp angles that would be unrealistic and promote stress concentration at the start of the test, the numerical curves show a small curvature at the start of the test. This is because the peel arm is pulled while it is still free or subject to low stresses. Therefore, given that in the experimental tests a slight pre-load was always applied to ensure that the peel arm was tractioned at the start of the tests, the numerical curves were adjusted to the left to mitigate this effect in the comparison of both results.

In general, the stiffness for adhesive A was similar to the experimental results at the beginning of the curves. Moreover, when we come closer to the zone before the plateau, we can see that the experimental results have a decrease in the stiffness that does not occur in the FE model. This behaviour might occur due to the presence of defects, light voids, entrapped air in the interface, or some wrinkling of the steel backing. The numerical peeling test at 180° showed unusual initial behaviour due to the high plastic bending

deformation that occurs in the steel strip since this is completely bent.

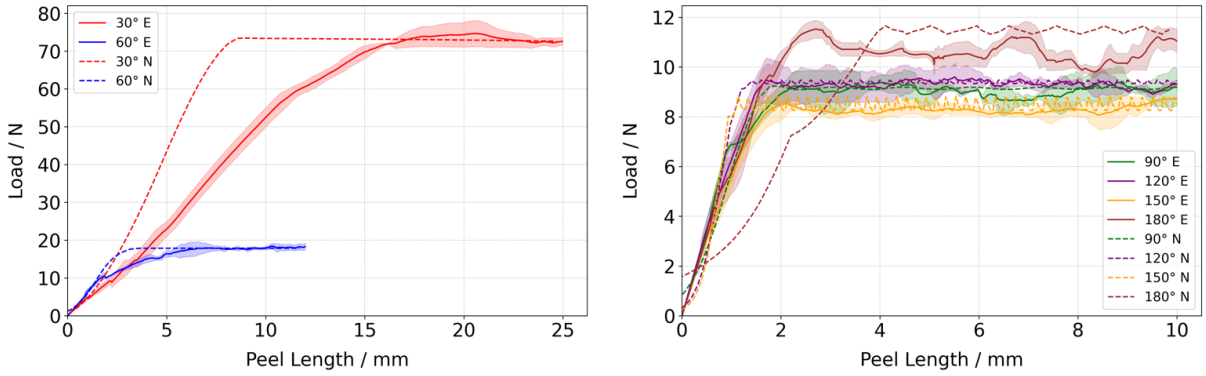


Figure 10: Comparison between the experimental and numerical peel curves obtained with adhesive A.

Regarding adhesive B, the stiffness of the numerical curves showed good agreement with the experimental data except for the 30° (which will be further explained) and 150°. This last scenario might be derived from an inaccurate prediction of the δ. As previously explained, the 180° stiffness was obtained using L instead of δ due to the direction of the peeling force in this condition. Since the 150° test is very close to the previously mentioned case, the value considered for the CTOD may be inaccurate, leading to an unrealistic stiffness.

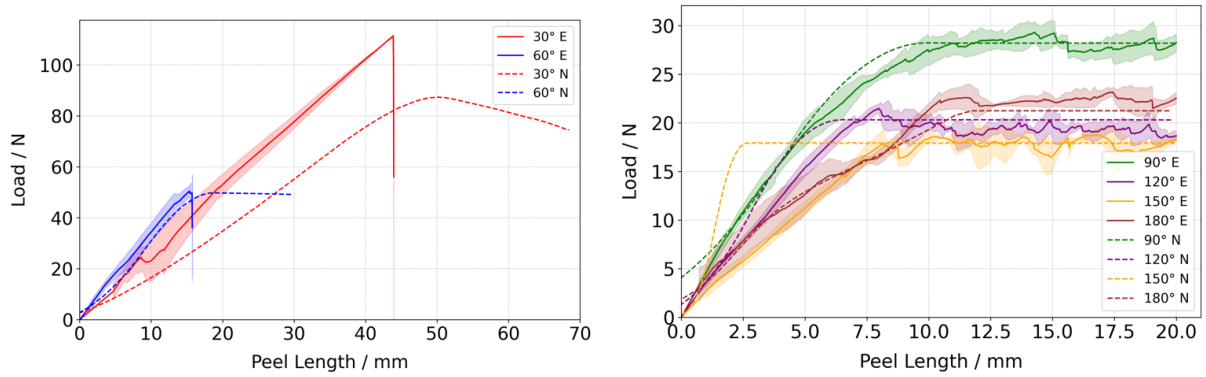


Figure 11: Comparison between the experimental and numerical peel curves obtained with adhesive B.

The stress distributions were plotted and analysed throughout the entire adhesive layer in the instant where stable crack propagation starts, i.e. when the first element in the peel front reaches a damage value of 1. A local reference system was used for each cohesive element where σ_{22} is the direct stress through the thickness and σ_{12} is the transverse shear stress.

Considering the stress distribution for the peel tests with an inclination of 30° and 60°, the two adhesives presented shear forces acting through the entire adhesive layer, allowing

these testing conditions to reach higher loads. This results are presenetd in Figures 12 and 14 for adhesives A and B, respectively.

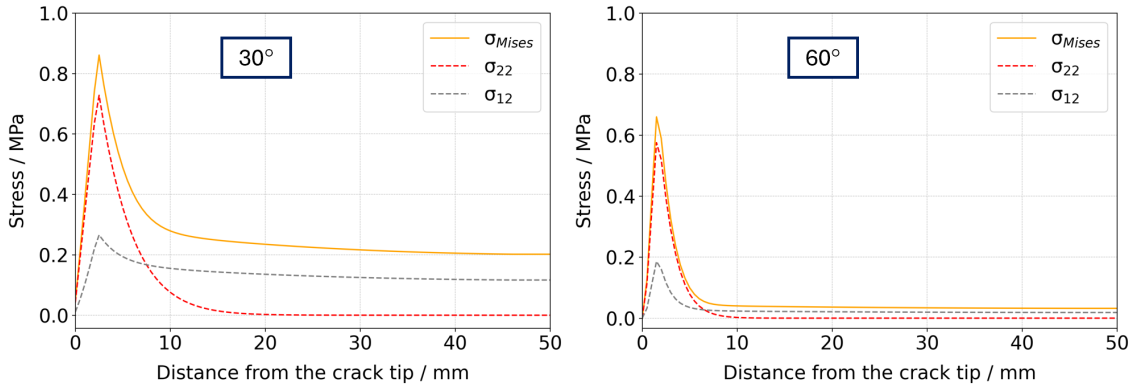


Figure 12: Stress distribution in the adhesive A layer for peeling angles of 30° (left) and 60° (right).

In adhesive B, for the 30° loading scenario, although the numerical model could predict that this condition could not reach a plateau, this FE model did not accurately predict the maximum load obtained in the joint (Figure 11 (left)). Since the peel test did not reach a steady state crack propagation in the experimental tests, the fracture energy employed in the FE model was below from the real one that the adhesive can actually reach. Moreover, as illustrated in Figure 13 and 14, it is clear that the shear forces acting on the adhesive layer are present throughout the entire bonding length, representing about 50% of the stresses acting on the peel front. Overall, adhesive B should be tested with a larger bonding length, ensuring that the adhesive layer at the free edge is stress-free, in order to obtain a stable crack propagation, and, consequently, an accurate value for the fracture energy of this joint.

For the 60° peel test, adhesive B could predict with precision the value obtained at the maximum load. However, while in the experimental tests, adhesive B failed abruptly, in a similar behaviour to the one observed for the 30° peel test, in the FE model, the results showed that the load-displacement curve was able to reach a plateau. This can be explained by the fact that, although the experimental results revealed a catastrophic failure, the adhesive is very close to the threshold that enables the crack to stably propagate. Since the numerical model is an ideal scenario, in which there are no defects in the joint, it predicts that 60° will propagate stably. From Figure 14 (right) it is visible that, although we have fewer shear forces when compared to the lower angle case, we still have the presence of this acting along the entire adhesive layer.

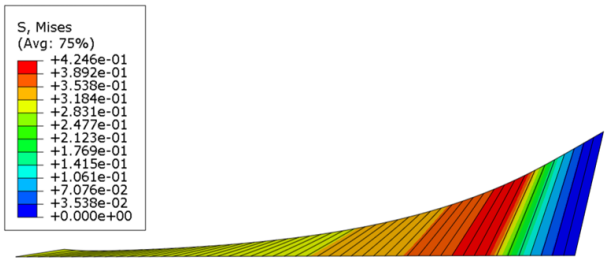


Figure 13: FE visualization of the stress distribution in the adhesive B layer of a 30° peel test.

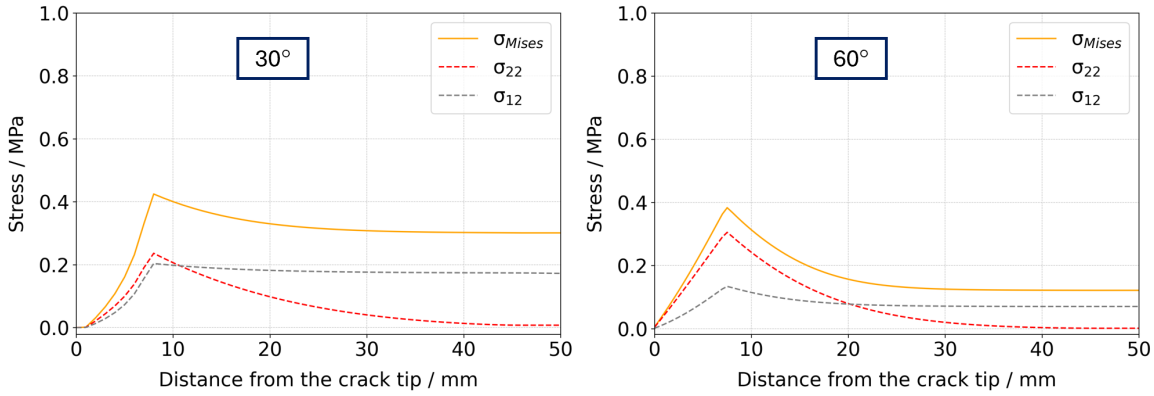


Figure 14: Stress distribution in the adhesive B layer for peeling angles of 30° (left) and 60° (right).

Regarding the higher peeling angles (from 90° to 150°) the numerical model accurately predicts the force obtained in the plateau for both adhesives. Figures 15 and 16 presents the stresses acting along the adhesive layer for 90°, 120° and 150° for adhesives A and B, respectively. Since for this range of peeling angles, the stresses acting on the adhesive are more concentrated at the peel front, the length under analysis was reduced. As we increase the peeling angle, it can be observed that there is an increase in the stress concentrations at the peel front, leading to the failure of the joint at lower loads. Comparing the values obtained in the 90° peel tests with adhesives A and B, it can be seen that, in the latter, we still have, in accordance with what happens at lower angles, stresses acting along the entire layer of adhesive. This phenomenon helps to explain why we have greater forces in the joints produced with adhesive B when peeled at 90° when compared to higher angles and not in the joints produced with adhesive A.

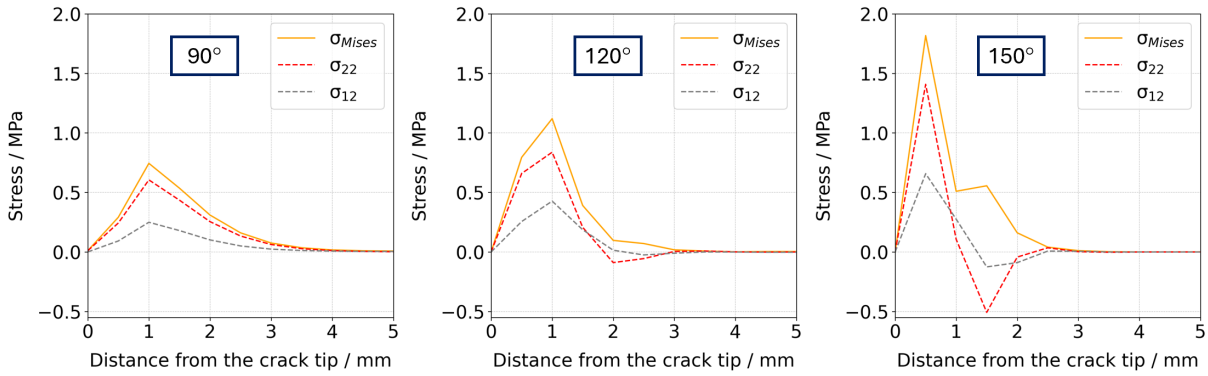


Figure 15: Stress distribution in the adhesive A layer for peeling angles of 90° (left), 120° (center) and 150° (right).

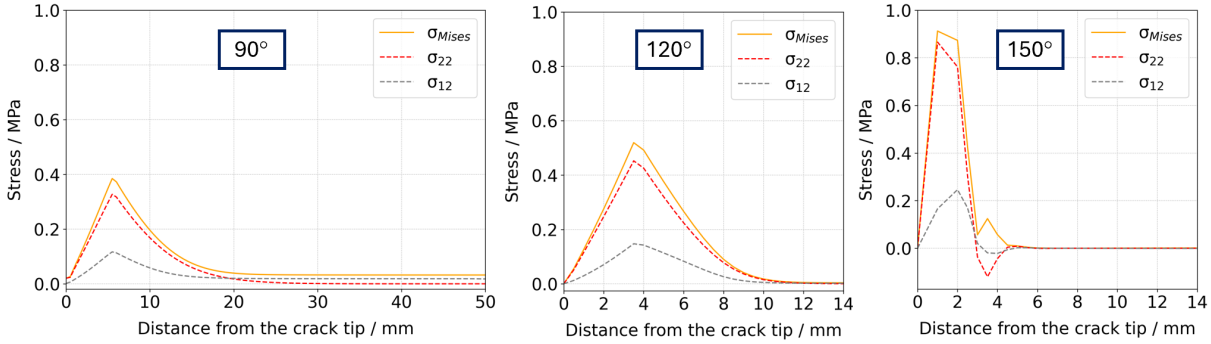


Figure 16: Stress distribution in the adhesive B layer for peeling angles of 90° (left), 120° (centre) and 150° (right).

Additionally, it can be noticed that an increase in the inclination of testing also leads to the appearance and subsequently increase of the compression effects. Figures 17 and 18 show this behaviour on Abaqus software and on the experimental tests for a 150° peel test with adhesives A and B, respectively. It can be seen, in the images on the right, that the compressive effects are present on the adhesive, corroborating the numerical results.

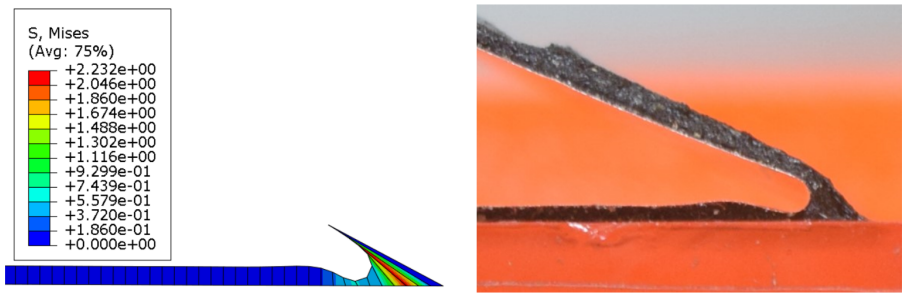


Figure 17: Compression effects on the 150° peel test with adhesive A. FE software (left), experimental test (right).

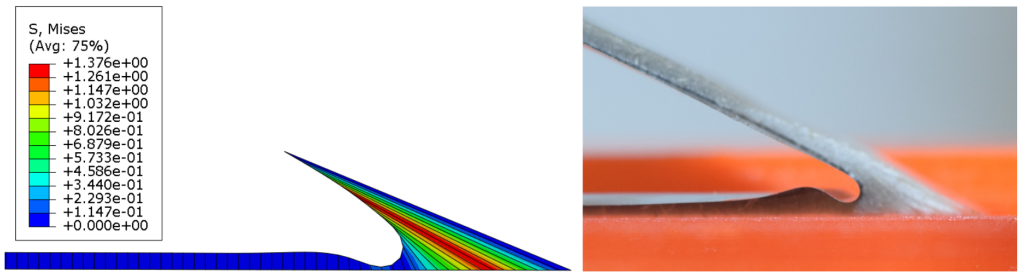


Figure 18: Compression effects on the 150° peel test with adhesive B. FE software (left), experimental test (right).

Finally, observing the performance of the 180° tests (Figure 19), we have a reduction at the peak stress and a greater distribution of the stresses along the adhesive layer. These results are in line with the experimental results, confirming that the larger area of deformation created by the peeling direction leads to a small increase in the load-bearing capacity of the joint.

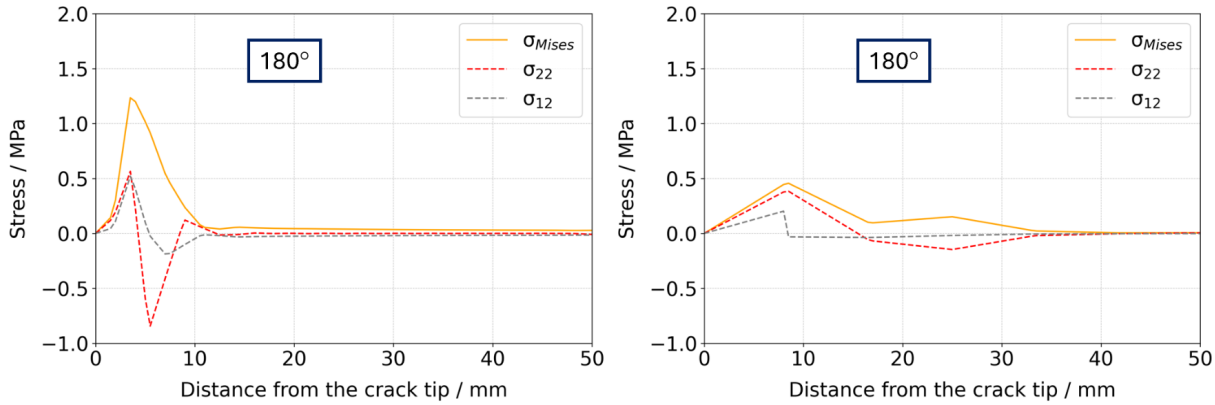


Figure 19: Stress distribution in the adhesives A (left) and B (right) layers for a peeling angle of 180°.

5 Conclusions

This work has made significant strides in understanding the failure mechanisms of two acrylic pressure-sensitive adhesives (PSAs) when subjected to peel testing under various test conditions.

The experiments conducted were designed to evaluate the performance of the adhesives through peel tests at multiple angles, ranging from 30° to 180°. This comprehensive range allowed for the construction of a detailed load failure envelope for each adhesive, providing insights into their behaviour under different loading conditions. Notably, the experimental data underscored the consistency of adhesion energy across varying peel angles when accounting for the energy dissipated due to the bending of the steel backing,

confirming the hypothesis that adhesion energy is an intrinsic material property of the system.

Furthermore, the digital image processing of the recorded peel tests revealed significant variations in the fracture process zone (FPZ) with changes in peel angle. The findings indicated that lower angles resulted in an increase in the length of the FPZ and a decrease in its height, suggesting more effective energy dissipation at these angles. Conversely, angles greater than 90° led to a reduction in both dimensions of the FPZ, highlighting a propensity for early adhesive failure due to increased stress concentration at the peel front. The 180° tests, in particular, demonstrated the influence of shear forces, evidenced by an increase in the FPZ length and a corresponding rise in failure loads.

The cohesion of the experimental approach with numerical simulations was particularly evident in the application of CZM to peel tests. The cohesive laws derived from the experimental tests were effectively used to simulate the behaviour of peel specimens under different angles, with the numerical predictions aligning closely with experimental outcomes. This work provides an effective methodology to extract a cohesive law of a joint capable of accurately predicting its behaviour. Additionally, through an extensive stress analysis of the results obtained along the adhesive layer, it is possible to study the failure modes behind these two acrylic PSAs.

References

[1] R. Ciardiello. Mechanical characterization and separation tests of a thermoplastic reinforced adhesive used for automotive applications. *Procedia Structural Integrity*, 24:155–166, 2019.

[2] Y. Boutar, S. Naïmi, S. Mezlini, C. Carbas, RJ, M. da Silva, LF, and M. Ben Sik Ali. Cyclic fatigue testing: Assessment of polyurethane adhesive joints' durability for bus structures' aluminium assembly. *Journal of Advanced Joining Processes*, 3:100053, 2021.

[3] K. Kawajiri, M. Kobayashi, and K. Sakamoto. Lightweight materials equal lightweight greenhouse gas emissions: A historical analysis of greenhouse gases of vehicle material substitution. *Journal of Cleaner Production*, 253:119805, 2020.

[4] I. Benedek and M. M. Feldstein. *Fundamentals of Pressure Sensitivity*. CRC Press, 2008.

[5] XH Deng. Progress on rubber-based pressure-sensitive adhesives. *Journal of Adhesion*, 94:77–96, 2018.

[6] H. Huang. *Mechanical Characterization of Pressure-Sensitive Adhesive (PSA) Bonded Assembly.* PhD thesis, University of Maryland, College Park, 2019.

[7] A. N. Gent and R. E. Petrich. *Proceedings of the Royal Society A*, 310:433–448, 1969.

[8] A. N. Gent and A. J. Kinloch. *Journal of Polymer Science: Polymer Physics Edition*, 9:659–668, 1971.

[9] PB Lindley. Ozone attack at a rubber-metal bond. *J Instn Rubb Ind*, 5(6):243–248, 1971.

[10] A. J. Kinloch, C. C. Lau, and J. G. Williams. The peeling of flexible laminates. *International Journal of Fracture*, 1994.

[11] I. Georgiou, H. Hadavinia, A. Ivankovic, A. J. Kinloch, V. Tropsa, and J. G. Williams. Cohesive zone models and the plastically deforming peel test. *The Journal of Adhesion*, 79(3):239–265, March 2003.

[12] Bamber Blackman, Homayoun Hadavinia, Anthony Kinloch, and J. Williams. The use of a cohesive zone model to study the fracture of fibre composites and adhesively-bonded joints. *International Journal of Fracture*, 119:25–46, 2003.

[13] H. Hadavinia J.G. Williams. Analytical solutions for cohesive zone models. *Journal of Mechanics and Physics of Solids*, 50:809–825, 2002.

[14] T. Diehl. On using a penalty-based cohesive-zone finite element approach, part ii: Inelastic peeling of an epoxy-bonded aluminum strip. *International Journal of Adhesion and Adhesives*, 28:256–265, 2008.

[15] A.J. Kinloch Ph. Martiny, F. Lani and T. Pardoen. Numerical analysis of the energy contributions in peel tests: a steady-state multilevel finite element approach. *International Journal of Adhesion and Adhesives*, 28:222–236, 2008.

[16] J.W. Hutchinson Y. Wei. Interface strength, work of adhesion and plasticity in the peel test. *Recent Advances in Fracture Mechanics*, pages 315–333, 1998.

[17] A.J. Kinloch H. Hadavinia, L. Kawashita, D.R. Moore, and J.G. Williams. A numerical analysis of the elastic–plastic peel test. *Engineering Fracture Mechanics*, 73:2324–2335, 2006.

[18] R.A. Sauer. Enriched contact finite elements for stable peeling computations. *International Journal of Numerical Methods in Engineering*, 87:593–616, 2011.

[19] Michael D. Bartlett, Scott W. Case, Anthony J. Kinloch, and David A. Dillard. Peel tests for quantifying adhesion and toughness: A review. *Progress in Materials Science*, 137:101086, August 2023.

[20] A. N. Gent and G. R. Hamed. Peel mechanics of adhesive joints. *Polymer Engineering & Science*, 17(7):462–466, 1977.

[21] A. N. Gent and G. R. Hamed. Peel mechanics. *The Journal of Adhesion*, 7(2):91–95, 1975.

[22] A.N. Gent and G.R. Hamed. Peel mechanics for an elastic-plastic adherend. *Journal of Applied Polymer Science*, 21(10):2817 – 2831, 1977.

[23] D.S. Dugdale. Yielding of steel sheets containing slits. *Journal of the Mechanics and Physics of Solids*, 8(2):100–104, 1960.

[24] L. Hakim and S.E. Mikhailov. A history-dependent cohesive zone model in elastic and visco-elastic materials under constant and variable loading. *International Journal of Mechanical Sciences*, 144:518–525, 2018.

[25] Gang Zhao, Jiaqi Xu, Yajie Feng, Jianbo Tang, Yousi Chen, Shiqing Xin, Xigao Jian, Shuxin Li, Shouhai Zhang, and Jian Xu. A rate-dependent cohesive zone model with the effects of interfacial viscoelasticity and progressive damage. *Engineering Fracture Mechanics*, 248:107695, 2021.

[26] Imadeddin Zreid, Robert Fleischhauer, and Michael Kaliske. A thermomechanically coupled viscoelastic cohesive zone model at large deformation. *International Journal of Solids and Structures*, 50(25):4279–4291, 2013.

[27] IIT library. 6.777j/2.751j material property database. `https://yourlibrary.iit.edu/material_property_database`, 2024. Accessed: 2024-02-27.

[28] Christopher Kovalchick. *Mechanics of Peeling: Cohesive Zone Law and Stability*. Ph.d. thesis, California Institute of Technology, Pasadena, California, May 2011. Defended on May 9, 2011.

[29] D. H. Kaelble. Theory and Analysis of Peel Adhesion: Mechanisms and Mechanics. *Transactions of The Society of Rheology*, 3(1):161–180, March 1959.

[30] Yoshiki Sugizaki, Takaaki Shiina, Yoshimi Tanaka, and Atsushi Suzuki. Effects of peel angle on peel force of adhesive tape from soft adherend. *Journal of Adhesion Science and Technology*, 30(24):2637–2654, December 2016.

[31] Masako Yamada, Kosuke Takahashi, Nao Fujimura, and Takashi Nakamura. Generalized characteristics of peel tests independent of peel angle and tape thickness. *Engineering Fracture Mechanics*, 271:108653, August 2022.

[32] Marco Musto and Giulio Alfano. A fractional rate-dependent cohesive-zone model. *International Journal for Numerical Methods in Engineering*, 103(5):313–341, 2015.

[33] M. J. van den Bosch, P. J. G. Schreurs, and M. G. D. Geers. On the development of a 3D cohesive zone element in the presence of large deformations. *Computational Mechanics*, 42(2):171–180, July 2008.

[34] M.J. van den Bosch, P.J.G. Schreurs, and M.G.D. Geers. Identification and characterization of delamination in polymer coated metal sheet. *Journal of the Mechanics and Physics of Solids*, 56(11):3259–3276, 2008.

Appendix C

Python code for adhesion energy estimation

```

import math
import numpy as np
from openpyxl import Workbook

test = 1    # 1 for black PSA results and 2 for grey PSA results
# Constants
MAX_ITER = 3000
DELTHETA0 = 0.0005
TOL = 0.00005

# Global variables
alpha, E, ey, theta, theta0, critheta0, h, GinfE, k = 0, 0, 0, 0, 0, 0, 0, 0, 0
miderror, begerror, oldtheta0, oldk = 0, 0, 0, 0

results = []

def input_consts():
    global alpha, ey, E
    alpha = 0.01863523205415344
    ey = 0.0064
    E = 160000        #MPa


def input_vars():
    global h, theta, GinfE

    theta_vector = np.array([30, 60, 90, 120, 150, 180]) * np.pi / 180

    if test == 1:
        GinfE_vector = np.array([1.0004780906269048, 0.8891169503135101,
    0.904772018407701, 1.39422068533696, 1.5455143665954971, 2.1634478153852075])
    *1000
        h = 310

    if test == 2:
        GinfE_vector=np.array([1.4913179714370286, 2.5239843227955117,
    2.8030583313356177, 3.0242424916891695, 3.325218960178923, 4.446335043093464])
    *1000
        h = 1110

    theta  = theta_vector[i]
    print(math.degrees(theta))
    GinfE = GinfE_vector[i]



def compute_f2():
    global k, theta0
```

```
    k = 3.0 * theta0 / (4.0 * ey)
    if theta0 < critheta0:
        f2 = k * k / 3.0
    else:
        f2 = alpha * (1.0 + 4.0 * (1.0 - alpha) * (1.0 - alpha)) / 3.0 * k * k
        f2 += 2.0 * (1.0 - alpha) * (1.0 - alpha) * (1.0 - 2.0 * alpha) * k
        f2 += 8.0 / k * (1.0 - alpha)**4 / (1.0 - 2.0 * alpha) / 3.0
        f2 -= 4.0 * (1.0 - alpha)**3
    return f2

def check_error(error):
    global oldtheta0, oldk, begerror, miderror, i, j, theta0, k
    if abs(error) < TOL and i > 5:
        print("Stop 1: OK, but solutions can be improved by reducing the error
    tolerance")
        return 1
    elif i > MAX_ITER:
        print("Stop 2: Exceeding the max. number of iterations (MAX_ITER)")
        return 2
    elif abs(miderror) < abs(begerror) and abs(miderror) < abs(error) and j > 4 and
     i > 5:
        k = oldk
        theta0 = oldtheta0
        print("Stop 3: Successful!")
        return 3
    elif theta0 > theta:
        print("Stop 4: theta0 > theta - no solution")
        return 4
    oldtheta0 = theta0
    oldk = k
    begerror = miderror
    miderror = error
    return 0

def compute_fl():
    global k, alpha, critheta0
    if theta0 < critheta0:
        fl = (1.0 - alpha) * (1.0 * k * k / 3.0 + 2.0 * (1.0 - alpha) / k / 3.0 -
    1.0)
    else:
        fl = 4.0 * alpha * (1.0 - alpha) * (1.0 - alpha) * k * k / 3.0
        fl += 2.0 * (1.0 - alpha) * (1.0 - alpha) * (1.0 - 2.0 * alpha) * k
        fl += 2.0 * (1.0 - alpha) * (4.0 * (1.0 - alpha)**3 + 1.0) / k / 3.0 / (1.0
     - 2.0 * alpha)
        fl -= (1.0 - alpha) * (4.0 * (1.0 - alpha) * (1.0 - alpha) + 1.0)
    return fl

def compute_Geba(pbgh):
    global ey, GinfE, alpha
```

```
    if ey * pbgh / 2.0 < 1.0:
        return GinfE + ey * ey * pbgh * pbgh / 4.0
    else:
        return GinfE + (ey * pbgh * ey * pbgh / 4.0 + (1.0 - ey * pbgh)) / alpha

def main():
    global theta0, critheta0, i, j, miderror, begerror, oldtheta0, oldk, theta,
    GinfE, k, alpha, ey, E, h

    input_consts()

    while True:
        input_vars()

        Gemax = E * ey * ey * h / 2.0
        GinfE /= Gemax
        i = 0
        j = 5
        theta0 = 0.005
        critheta0 = 2.0 * ((1.0 - alpha) / (1.0 - 2.0 * alpha)) * 4.0 * ey / 3.0
        oldtheta0 = theta0  # Initialize oldtheta0
        oldk = k  # Initialize oldk

        while True:
            error = compute_f2() - GinfE * (1.0 - math.cos(theta - theta0)) / (1.0
    - math.cos(theta))
            error_msg = check_error(error)
            if error_msg != 0:
                break
            theta0 += DELTHETA0
            i += 1

        if error_msg == 1 or error_msg == 3:
            Gdb = compute_f1()
            pbgh = GinfE / (1.0 - math.cos(theta))
            Geba = compute_Geba(pbgh)
            Ga = Geba - Gdb
            results.append([
            math.degrees(theta),
            Ga * Gemax,
            Gdb * Gemax,
            theta0 * 180.0 / math.pi,
            Geba * Gemax
            ])
            print(f"\nThe value of Ga (J/m^2) = {Ga * Gemax:.3f}")
            print(f"The value of Gdb (J/m^2) = {Gdb * Gemax:.3f}")
            print(f"The root angle (deg) = {theta0 * 180.0 / math.pi:.3f}")
            print(f"The Geba values (J/m^2) = {Geba * Gemax:.3f}")

```

```
        break


theta_vector = np.array([30, 60, 90, 120, 150, 180]) * np.pi / 180

for i in range(len(theta_vector)):
    if __name__ == "__main__":
        main()


wb = Workbook()
ws = wb.active
ws.title = "Results"
ws.append(['Theta (degrees)', 'Ga (J/m^2)', 'Gdb (J/m^2)', 'Root Angle (degrees)',
    'Geba (J/m^2)'])

for result in results:
    ws.append(result)

wb.save("results.xlsx")
```

Appendix D

Python code for digital image processing

```
1
2  import cv2
3  import numpy as np
4  import matplotlib.pyplot as plt
5
6  # Load the image
7  Date = '30_04'
8  test = 'cinzento_90_'
9  test_number = '5'
10 photo_number = '0072'
11 image_path = 'D:\\FEUP\\Mestrado EAV\\2 ano\\Tese\\Peel\\Fotos\\' + Date + '\\' +
       test + test_number + '\\DSC_' + photo_number + '.jpg'
12
13
14 image = cv2.imread(image_path)
15
16 # Check if the image is loaded correctly
17 if image is None:
18     raise ValueError(f"Failed to load image at {image_path}")
19
20 # List to store points
21 points = []
22
23 # Function to handle mouse clicks
24 def onclick(event):
25     if event.button == 1:  # Left mouse button
26         if event.xdata and event.ydata:
27             points.append((int(event.xdata), int(event.ydata)))
28             plt.plot(event.xdata, event.ydata, 'ro')
29             plt.draw()
30             if len(points) == 6:
31                 plt.close()
32     elif event.button == 3:  # Right mouse button
33         if points:
34             points.pop()
35             # Redraw the image and points
36             plt.cla()
37             ax.imshow(cv2.cvtColor(image, cv2.COLOR_BGR2RGB))
38             plt.title('Click to select points: 2 for acrylic thickness, 2 for crack
       width, 2 for process zone length')
39             for point in points:
40                 plt.plot(point[0], point[1], 'ro')
41             plt.draw()
42
43 # Function to handle zooming with scroll wheel
44 def zoom_factory(ax, base_scale=1.1):
45     def zoom(event):
46         cur_xlim = ax.get_xlim()
47         cur_ylim = ax.get_ylim()
```

```
        xdata = event.xdata   # get event x location
        ydata = event.ydata   # get event y location
        if xdata is None or ydata is None:
            return

        if event.button == 'up':
            scale_factor = 1 / base_scale
        elif event.button == 'down':
            scale_factor = base_scale
        else:
            scale_factor = 1

        new_width = (cur_xlim[1] - cur_xlim[0]) * scale_factor
        new_height = (cur_ylim[1] - cur_ylim[0]) * scale_factor

        relx = (cur_xlim[1] - xdata) / (cur_xlim[1] - cur_xlim[0])
        rely = (cur_ylim[1] - ydata) / (cur_ylim[1] - cur_ylim[0])

        ax.set_xlim([xdata - new_width * (1 - relx), xdata + new_width * relx])
        ax.set_ylim([ydata - new_height * (1 - rely), ydata + new_height * rely])
        plt.draw()
    return zoom

# Display the image using matplotlib
fig, ax = plt.subplots()
ax.imshow(cv2.cvtColor(image, cv2.COLOR_BGR2RGB))
ax.set_title('Click to select points: 2 for acrylic thickness, 2 for crack width, 2
     for process zone length')
ax.set_aspect('equal')

# Connect the zoom function to scroll events
scale = 1.1
fig.canvas.mpl_connect('scroll_event', zoom_factory(ax, base_scale=scale))
fig.canvas.mpl_connect('button_press_event', onclick)
plt.show()

# Wait until six points are selected
while len(points) < 6:
    plt.pause(0.1)

# Ensure six points were selected
if len(points) != 6:
    raise ValueError("You must select exactly six points (two for acrylic thickness
    , two for crack width, and two for process zone length)")

# Extract points
acrylic_point1, acrylic_point2, crack_point1, crack_point2, process_zone_point1,
    process_zone_point2 = points

```

```
# Calculate acrylic thickness in pixels
acrylic_thickness_px = np.linalg.norm(np.array(acrylic_point1) - np.array(
    acrylic_point2))
print(f"Acrylic thickness in pixels: {acrylic_thickness_px:.2f}")

# Calculate crack width in pixels
crack_width_px = np.linalg.norm(np.array(crack_point1) - np.array(crack_point2))
print(f"Crack width in pixels: {crack_width_px:.2f}")

# Calculate process zone length in pixels
process_zone_length_px = np.linalg.norm(np.array(process_zone_point1) - np.array(
    process_zone_point2))
print(f"Process zone length in pixels: {process_zone_length_px:.2f}")

# Known acrylic thickness in mm
acrylic_thickness_mm = 6

# Scale factor
scale_factor = acrylic_thickness_mm / acrylic_thickness_px
print(f"Scale factor: {scale_factor:.6f} mm/px")

# Calculate CTOD in mm
ctod_mm = crack_width_px * scale_factor
print(f"Crack Tip Opening Displacement (CTOD): {ctod_mm:.2f} mm")

# Calculate process zone length in mm
process_zone_length_mm = process_zone_length_px * scale_factor
print(f"Process Zone Length: {process_zone_length_mm:.2f} mm")

# Display the image with selected points and lines
output_image = image.copy()
cv2.line(output_image, acrylic_point1, acrylic_point2, (255, 0, 0), 2)
cv2.line(output_image, crack_point1, crack_point2, (0, 0, 255), 2)
cv2.line(output_image, process_zone_point1, process_zone_point2, (0, 255, 255), 2)
for point in points:
    cv2.circle(output_image, point, 5, (0, 255, 0), -1)

# Save the final image
save_path = 'D:\\FEUP\\Mestrado EAV\\2 ano\\Tese\\Peel\\Fotos\\Images_python\\' +
    Date + '_' + test + test_number + '_' + photo_number + '.jpg'
cv2.imwrite(save_path, output_image)
print(f"Final image saved at {save_path}")

# Show the final image
plt.figure(figsize=(10, 10))
plt.title('Selected Points and Lines')
plt.imshow(cv2.cvtColor(output_image, cv2.COLOR_BGR2RGB))
plt.show()
```